**Room-Temperature Sodium-Sulfur Batteries and Beyond: Realizing Practical High Energy Systems through Anode, Cathode, and Electrolyte Engineering**

*Alex Yong Sheng Eng,† Vipin Kumar,† Yiwen Zhang,† Jianmin Luo, Wenyu Wang, Yongming Sun, Weiyang Li,* and Zhi Wei Seh**

Dr. A.Y. S. Eng, Prof. Z. W. Seh
Institute of Materials Research and Engineering, Agency for Science, Technology and Research (A*STAR), 2 Fusionopolis Way, Innovis, Singapore 138634, Singapore.
Email: sehzw@imre.a-star.edu.sg (Z.W.S.)

Prof. V. Kumar
Centre for Energy Studies, Indian Institute of Technology Delhi, New Delhi, India, 110016.

Y. Zhang, Dr. J. Luo, Prof. W. Li
Thayer School of Engineering, Dartmouth College, 14 Engineering Drive, Hanover, New Hampshire 03755, United States.
Email: weiyang.li@dartmouth.edu (W.L.)

W. Wang, Prof. Y. Sun
Wuhan National Laboratory for Optoelectronics and School of Optical and Electronic Information, Huazhong University of Science and Technology, Wuhan, 430074, China.

† These authors contributed equally to this work.

Keywords: room-temperature sodium-sulfur batteries, sulfur composites, sulfur cathodes, sodium anodes, solid electrolyte interphases, polymer electrolytes, solid-state electrolytes

The increasing energy demands of society today have led us to pursue alternative energy storage systems that can fulfil rigorous requirements like cost-effectiveness and high storage capacities. Based fundamentally on earth-abundant sodium and sulfur, room-temperature sodium-sulfur batteries are a promising solution in applications where existing lithium-ion technology remains less economically viable, particularly in large-scale stationary systems such as grid-level storage. In this Review, we first highlight the key challenges in the field, followed by comprehensive analyses of accessible strategies to overcome them, starting from engineering of the anode-electrolyte interface in both liquid and solid electrolytes. Upcoming polymer and solid-state electrolytes are also surveyed. We then focus on the core principles guiding use-inspired design of cathode architectures, covering the spectrum of elemental sulfur and polysulfide cathodes, to emerging host structures, and covalent composites. Future

prospects are explored, with insights into other alkali-metal systems beyond sodium-sulfur batteries, such as the potassium-sulfur battery. We finally conclude by outlining the research directions necessary to attain high energy sodium-sulfur devices, and potential solutions to issues concerning large-scale production, so as to ultimately realize widespread deployment of practical energy storage systems.

## 1. Introduction

The energy demands of today's society continue to rise even as we push towards clean energy production with sustainable sources such as solar, wind, and tidal power. The intermittent nature of these sources however, necessitates concurrent deployment of an extensive energy storage ecosystem capable of delivering an uninterrupted supply to the array of stationary and mobile applications. This has spurred the development of new systems and sustainable materials.[1] Battery systems in particular, have found themselves to be in increasing demand over the last decade for portable electronic devices, electric vehicles, and in stationary grid storage systems.[2-4] As of 2018, lithium-ion (Li-ion) batteries take the top spot as the most prevalent energy storage technology with total global power deployment reaching over 1.6 GW, barring pumped hydropower primarily for grid-level storage.[5] Nevertheless in recent years, manufacturers of Li-ion batteries have been facing increasingly fierce competition in the marketplace and continuous price reduction (at approximately 14% annually per kWh).[6,7] Based on recent projections, the battery demand from electric vehicles alone will exceed 2000 GWh by 2030,[8] and at the same time, the cost of battery packs is expected to fall to $144 per kWh.[9] Therefore, it is critical and desirable to develop battery systems with both high performance and low cost to satisfy the market demands.

A promising and viable battery system that fulfils these two requirements at the same time is the sodium–sulfur (Na-S) battery. Similar to the lithium–sulfur (Li-S) battery that is known for its high energy density, the Na-S battery system is under extensive investigation as

it not only benefits from the high performance of the metal-sulfur battery configuration, but also takes advantage of low material costs of both sodium (Na) and sulfur (S).[10-13] The Na-S battery delivers a high theoretical energy density of 1274 Wh $kg^{-1}$ which is about three times higher than that of Li-ion batteries (~420 Wh $kg^{-1}$),[14, 15] while the price of Na raw material is only $1/25^{th}$ that of Li owing to its high abundance (Na: 23,600 mg $kg^{-1}$ *vs*. Li: 20 mg $kg^{-1}$ in the Earth's Crust) and accessibility.[16,17] These advantages open up new possibilities and opportunities for the Na-S battery system.

Investigation into Na-S batteries dates back to the 1960s when high-temperature Na-S batteries were tested for the first time.[10] At an operating temperature in the range of 300 to 350 °C, both Na metal anode and S-cathode work in their molten states. These batteries use a ceramic layer of Na β"-alumina as solid electrolyte that can only yield sufficient Na-ion conductivity beyond 300 °C. These were later employed in grid-scale energy storage applications but suffered from severe safety, durability, and system maintenance issues due to the highly reactive and corrosive nature of molten states of both S and Na at high temperature, as well as the risk of rupture of the solid electrolyte.[18] Hence, ambient-temperature Na-S batteries have drawn much attention over the past decade, and they are considered as promising alternatives for both stationary grid storage and transportation applications. To achieve sufficient Na-ion conductivity at room temperature, these batteries typically utilize polymer-based gels or liquid phase organic solvents as electrolytes.[19] As illustrated in **Figure 1**, a typical room-temperature (r.t.) Na-S battery is comprised of a Na metal anode, an S-based cathode, and an ion-conductive electrolyte in between. The battery reaction generally starts with discharge if elemental sulfur ($S_8$) is used as cathode. During discharge, sulfur receives electrons and first goes through a solid-liquid phase transition, in which insoluble sulfur transforms to the long-chain polysulfide $Na_2S_8$ that can dissolve into the electrolyte. This phase transition is represented by the first plateau at around 2.2 V in the discharge curve. The plateau is followed by a slope which corresponds to further reduction of the dissolved

polysulfides from $Na_2S_8$ to $Na_2S_4$. Further conversion from dissolved $Na_2S_4$ to insoluble $Na_2S_3$ or $Na_2S_2$ then occurs, represented by the second plateau at around 1.65 V for this liquid-solid phase transition. In some cases, a slope after 1.65 V is regarded as the transformation of $Na_2S_3$ or $Na_2S_2$ to $Na_2S$ as the final product.[10,20] The subsequent charge is a reverse process, in which short-chain Na sulfides undergo multiple phase-transitions and are oxidized back to sulfur.

Since the validation of a r.t. Na-S battery for the first time in 2006, inspiring progress has been achieved, including rational design and synthesis of cathode materials, anode protection, and new electrolyte systems to realize optimal battery performance.[19,21,22,23] Meanwhile, a considerable number of studies have been devoted to elucidating the underlying electrochemical reaction mechanisms.[24,25] Despite such advancements, practical applications of r.t. Na-S batteries are still hindered by unsatisfactory performance metrics, including poor cycle life, low active material utilization, and low Coulombic efficiency. Insights gleaned from numerous works have since revealed critical issues caused by fundamental materials challenges originating from both S-cathode and Na metal anode, as summarized in **Table 1**.

**Figure 2** details major milestones in the development of Na-S batteries to date. In the early years since 2006, many explorations focused on liquid-based electrolytes and S-infused carbon cathodes, and uncovered potentialities and limitations in Na-S batteries.[17,19] Many systems suffered from very short battery lifetimes until breakthroughs in cathode design were reported. As summarized on the right panel of Figure 2, innovations in covalent sulfur composites (green) significantly alleviated the shuttle effect, with improved cycle lifetimes helping to bridge the gap towards eventual commercialization of Na-S technology. Targeting the same challenges, further cathode modifications such as sulfur and $NaS_2$ encapsulation (pink, grey) and electrocatalytic additives (yellow) have also been introduced, which effectively improved cell performance. In the left panel, we have seen the development of novel electrolyte designs (purple) and separator modifications (light blue). Further success in

the engineering of stable Na-anode solid electrolyte interphases (SEI) have been achieved since 2015 with both intrinsic and extrinsic approaches (orange),[26] boosting Coulombic efficiencies and bringing Na-S batteries ever closer to practical applications. Nevertheless, our understanding of their interfacial chemistry remains lacking, especially with regard to different systems at various states-of-charge.

In this comprehensive Review, we start by examining the Na anode-electrolyte interface in Section 2 on the interaction and compatibility between various Na salts, solvents and Na metal, further detailing the development of electrolyte salts, highly concentrated electrolyte systems, and solid-state electrolytes. Recent innovations in engineering intrinsic and extrinsic interphases are discussed, followed by localized surface polishing, and guided Na deposition through host modification. Section 3.1 then surveys the strategies for S-cathodes based on *solid-liquid-solid* polysulfide conversions by exploiting polysulfide-binding adsorbents and electrocatalysts, fully encapsulated structures, or ion-selective membranes, gel-polymer and solid-state electrolytes capable of mitigating polysulfide dissolution and shuttling. On the other hand in Section 3.2, *solid-solid* conversion reactions serve to eliminate these issues by employing only insoluble sulfur species, with the broad class of sulfurized carbons, sulfur copolymers, and other short-chain sulfur host materials. Most importantly, we chart the *prospects* of Na-S batteries in Section 4, and consider the critical issues needed to bring current cells into actual production lines to build tomorrow's high energy battery packs (Figure 2, boxes with dashed lines). Aspects discussed include: maximizing full cell energy densities by increasing active S-loading, while applying self-healing materials to avoid structural degradation, extrinsic Na-anode interphases to allow processing in standard dry-room production environments, pre-sodiated cathode materials for assembly with common Na-ion battery anodes, dendrite-free eutectic liquid anodes, and other alkali-metal systems such as potassium-sulfur (K-S) batteries.

## 2. Stabilizing the Na anode-electrolyte interphase

### 2.1. Effect of salt and solvent

*2.1.1. Choice of salts and solvents, and their compatibility with Na anode*

One of the key challenges in developing metal anode batteries is in designing electrolyte formulations that may withstand rigorous operating conditions associated with metal-sulfur batteries, such as in the Na-S system. For instance, the Na-metal anode is highly reducing towards organic species, which includes reactive polysulfide species ($Na_xS_y$) formed at the cathode during discharge, or even solvent molecules themselves. These reactions, if left unchecked, would lead to solvent decomposition by either nucleophilic attack or proton abstraction, which greatly impacts cycle life.[27,28] In addition, the nature of electrolyte plays a crucial role in determining battery performance and longevity.[28,29]

Chu *et al.* recently identified that the metal-sulfur battery performance is associated with the *donocity* or donor number of electrolyte components, where battery performance was positively correlated with an increase in the donor number of the electrolyte formulation.[30] In 1976, Gutmann introduced two empirical parameters: *1)* donicity or donor number (DN) to describe nucleophilic character, and *2)* acceptor number (AN) to describe electrophilic character, with these parameters defined to facilitate better understanding of ion solvation behavior.[31] Solvents with high Gutmann DN have been reported to promote redox reactions of $Na_xS_y$ species by stabilizing multiple states of polysulfide anions and altering the kinetic pathway.[32] A high-DN solvent, like dimethylacetamide (DMA), was used to ensure full utilization of sulfur and its discharge product, $Li_2S$.[33] More recently, Gunasekara *et al.* demonstrated that anions with different DN significantly affect battery performance. For instance, the high-DN trifluoromethanesulfonate ($OTf^-$, triflate) anion exhibits a higher capacity due to stronger solvation of the $Li^+$ cation, as compared to the low DN of hexafluorophosphate ($PF_6^-$).[34] Despite that high-DN solvents offer distinct advantages in alleviating polysulfide deposition and solvent decomposition, reactivity towards the metal

anode (both Li and Na) is inevitable.[35] For this particular reason, solvents with high DN are unable to achieve stable cycling for extended durations in metal-sulfur batteries, and practical systems utilizing high-DN solvents are thus yet to be demonstrated. In addition to high-DN electrolyte formulations, altering the Gutmann AN is observed to be equally effective in improving the stability of the discharge product for high performance batteries.[30] Kwabi *et al.* also reported that increasing the solvent AN could be a promising strategy to increase solubility of discharge products in high performance batteries such as Li-$O_2$.[36]

Besides DN and AN of solvent, the nature of salt strongly affects the battery operation. Lutz *et al.* recently investigated the role of salt's donocity on the stability of the SEI on Na metal anode,[35] with findings in contrast to Gunasekara *et al.* on the Li metal anode.[34] Salts with different anions, *e.g.*, $PF_6^-$, $OTf^-$, perchlorate ($ClO_4^-$), and trifluoromethanesulfonimide ($TFSI^-$) acquired different DN in ethereal solvents: due to their different charge distributions, solvation behavior was observed to defer between these anions. However, the formation of solvent separated ion-pairs (SSIPs) was nonetheless identified to be the same irrespective of anion nature. It is also noteworthy that the anion size plays a significant role in ensuring the stability of the SEI. For example, uniform Na deposition could be achieved in the presence of small-sized anion, *e.g.* $PF_6^-$ anions, whereas a broken or non-uniform deposition appeared for medium-sized anions, such as $ClO_4^-$ and $OTf^-$. In contrast, the $TFSI^-$ anion , which is largest in size, was found to be unable to initiate Na deposition. Such deposition behavior is schematically represented in **Figure 3**a.

It is worth highlighting that in weakly solvating solvents however, the interaction of the anion increases in the following manner, $ClO_4^- < PF_6^- < OTf^- < TFSI^-$, which may indeed affect the stability of the SEI. They also demonstrated that replacing weakly interacting anions ($ClO_4^-$) with the strongly interacting $TFSI^-$ anion did not lead to enhanced battery performance, and careful selection of the anion component is crucial in designing high performance batteries. The remarkable differences and consequences for long-term stability were further established by

cycling Na coin cells, where electrolytes using NaTFSI were most detrimental for metallic Na, while NaOTf and $NaClO_4$ led to short-term stability. Only the combination of dimethoxyethane (DME) with $NaPF_6$ provided the highest efficiency and performance, in excellent agreement with Seh *et al.* where high average Coulombic efficiencies of 99.9% were maintained over 300 strip−plate cycles at 0.5 mA $cm^{-2}$ (Figure 3b,c).[26]

*2.1.2. Electrolyte salt and highly concentrated electrolyte systems*

It is known that precise control of electrolyte composition is crucial and significantly impacts the battery performance. This fact is paradoxical to the rocking chair mechanism in Li-ion batteries, where it is generally accepted that the electrolyte does not have an active role in charge transfer (*i.e.*, Faradaic reaction) mechanisms.[37] Contemporary Li-ion cells are mostly based on a 1 M salt concentration in a mixture of organic solvents, and while these recipes satisfy the primary requirements for a cell's operation, they are known to be volatile and readily degrade above 80 °C.[38] Substituting common graphite anodes with alkali metals can increase the full-cell energy density, but stresses the electrolyte by exposing it to freshly deposited Na, leading to poor reversibility and Coulombic efficiency *via* irreversible consumption of both Na and electrolyte. In this regard, highly concentrated electrolytes (HCEs, where the molar concentration is higher than 4 M) have emerged as a possible solution to metal anode batteries.[39] At elevated salt concentrations, thermodynamically stable Na complexes favor strong binding with free solvent molecules, significantly reducing the free solvent content and thereby reducing the occurrence of side reactions with the metal anode.[39,40] As shown in **Figure 4**a, the solvation structure of HCEs is different from diluted electrolytes (at 1 M concentration), where all solvent molecules are coordinated to cations. This leads to the formation of aggregates or crystal ion-pairs (*i.e.* AGGs) instead of SSIPs or contact ion-pairs (CIPs) common in diluted electrolytes, thus lowering its volatility/toxicity,

reduces dissolution of the current collector and confers higher overall electrochemical stability, but which comes at the cost of higher viscosity and lower ionic conductivity.[41]

The most important aspect in designing HCEs is to ensure chemical compatibility and thermodynamic stability of the solvent-salt mixture at high concentration, as not all combinations may produce a homogeneous and stable liquid state at room temperature.[42] Typically, a 4 M or greater mixture may lead to salt crystallization if not compatible with the solvent. A detailed analysis of the salt-solvent system to produce HCEs was performed by Brouillette *et al.* and Henderson *et al.*, providing us a good reference tool to select appropriate solvent-salt combinations for HCEs.[43-45] For example, as high as 5 M of sodium bis(fluorosulfonyl)imide (NaFSI) or sodium trifluoromethanesulfonimide (NaTFSI) can be dissolved in DME, EC/PC (ethylene carbonate/propylene carbonate), or DMSO with reasonable ionic conductivity (~$4x10^{-3}$ S $cm^{-1}$) and viscosity (~70 cP), but no more than 1 M $NaPF_6$ can be dissolved in DME or EC/PC.[46,47] In connection to HCEs, the anion nature plays a vital role in determining the stability of solvate complexes, and thus determines the liquidus concentration range.[48] For instance, electrolytes with $PF_6^-$, $FSI^-$, and $TFSI^-$ anions tend to be dissociated and are susceptible to form SSIPs in dilute solutions, while favoring AGGs in HCEs. The anion's charge distribution is determined by their chemical structure and the ability to experience Coulombic interaction with counter-ions. Consequently, the ionic conductivity and viscosity of HCEs vary as a function of ion concentration (Figure 4b). Henderson *et al.* scrutinized the effect of anions in Li salt-solvent mixtures using acetonitrile (AN) as a simple model solvent with straightforward monodentate solvation.[48,49] More recently, Lee *et al.* designed a HCE based on 5 M NaFSI-DME for high performance Na metal batteries exhibiting high stability and excellent reversibility.[46] In a separate study, Cao *et al.* identified that a salt concentration as high as 4 M could be equally effective to form HCEs.[50] One potential downside is the majority of current HCEs stable with Na metal

anodes are based solely on DME, and research efforts are in progress to substitute DME with other low vapor pressure solvents.

Although ether-based HCEs containing NaFSI or NaTFSI are able to provide stable Na cycling with excellent reversibility and high Coulombic efficiency, they come at the expense of poor wettability, high viscosity, and high costs concomitant with the high salt content. Zheng *et al.* reported a novel electrolyte system in which the salt concentration was significantly reduced, while ensuring the same solvation structure as obtained in ultra-concentrated electrolyte systems.[51] Figure 4c depicts their structural differences, where the salt concentration was reduced by an inert diluent like hydrofluoroether while preserving the Na solvation structures. Termed a localized high concentration electrolyte (LHCE), it consists of 2.1 M NaFSI salt in DME and bis(2,2,2-trifluoroethyl) ether (BTFE), at a solvent molar ratio of 1:2. It exhibited the lowest viscosity comparable to that of the dilute liquid electrolyte, see Figure 4d. Owing to the high ionic conductivity and low viscosity, LHCE enabled prolonged stripping/plating of Na with a high Coulombic efficiency of over 99% at various current densities (Figure 4e). The developed model electrolyte system provides a viable avenue for further improvement of Na metal anode performance, with continuing efforts to incorporate these electrolytes into high energy density batteries.

Besides conventional HCEs, unconventional viscous electrolytes based on sodium ammoniates ($NaX\text{-}YNH_3$, where X = I, $BH_4$, $BF_4$, and Y = 1–3.3) present a whole new family of electrolytes which ensure ultra-long stability (for weeks), and nearly 100% Coulombic efficiency.[52,53] Despite their high volatility, their flammability is much lesser than that of HCEs. Moreover, the ionic conductivity (~0.1 S $cm^{-1}$) was determined to be higher than that of their conventional HCE counterparts. Despite that the NaI-3.3 $NH_3$ electrolyte was initially designed by Badoz-Lambing *et al.* for use in primary batteries,[54] Martinez *et al.* more recently repurposed these for secondary batteries.[52] Liquid electrolytes with different ammonia concentrations were developed (*e.g.*, NaI-3.3 $NH_3$, $NaBF_4$-2.5 $NH_3$, and $NaBH_4$-1.5

$NH_3$), and observed to be highly effective in stabilizing the Na metal anode. The authors identified uniform Na deposition, and the overpotential was observed to be even smaller (~10-15 mV) than that of standard liquid electrolytes. The excellent Na stripping/plating with minimal overpotential was credited to the unique attributes of ammoniates, which include a high $Na^+$ ion concentration (> 7 M), high ionic conductivity on the order of $10^{-1}$ S $cm^{-1}$, and a solvation structure very similar to that of an ionic liquid, but with the advantage of low viscosity. Finally, it was stated that the development of new Na metal batteries using the aforementioned ammoniates do not entail high costs since Na salts are usually cheaper than their Li counterparts. In addition, liquid ammonia is also inexpensive, with the result that the studied ammoniates were estimated to cost approximately 3–5 times lower than conventional organic electrolytes containing $NaPF_6$, and roughly 10 times lower than NaFSI or NaTFSI electrolytes.

*2.1.3. Beyond liquid electrolytes*

Liquid electrolytes exhibit fast kinetics, low charge transfer resistance, and excellent electrode wettability, but pose serious concerns related to safety and cycle life; unwarranted dendrite growth, sulfur dissolution, and shuttling of the discharge products being key issues. Currently, electrolytes used in metal anode batteries are mostly all-organic in nature (*e.g.*, ether- or carbonate-based). Due to high vapor pressures, such electrolytes have poor thermal stability which leads to generation of undesirable gases upon decomposition at the metallic anode,[55] and are prone to leakage or explosions in some cases. With their serious associated issues, solid electrolytes have been explored as an alternative both to suppress dendrite growth and mitigate the shuttle effect from dissolution of long-chain polysulfides, $Na_2S_5$-$Na_2S_8$.[56] An ideal solid electrolyte should have the following properties: high ion mobility, wide electrochemical potential window, stable mechanical properties (sufficiently stiff but adequately ductile), stable chemical and electrical properties, and maintaining electrochemical

stability under the respective redox reactions occurring at both electrode interfaces.[57,58] In practice however, one of the main reasons hampering commercialization of solid electrolyte batteries is their poor ionic conductivity at ambient operating temperatures, which strongly affects the specific capacity and cycle life of the cell.[58]

To this end, gel polymer electrolytes (GPEs) have been tested and successfully developed in recent years.[59-63] Interestingly, $Na^+$ ion transport in gel electrolytes is fundamentally identical to its liquid electrolyte counterpart, albeit with altered diffusive properties.[64] To improve GPE effectiveness, fillers such as $SiO_2$ and $Al_2O_3$ nanostructures, or graphene oxide (GO) are introduced into polymer matrices with the ability for $Na^+$ ion transport. Common examples of polymers include poly(methyl methacrylate) (PMMA) and poly(vinylidene fluoride-co-hexafluoropropylene) (PVdF-HFP).[59,65-67] Luo *et al*. developed a novel GPE using GO flakes as ion transport sites in a PVdF-HFP host, attaining reversible stripping/plating of Na for over 400 hours at 5 mA $cm^{-2}$. GO contains rich oxygen-containing functional groups that have strong affinity towards positively charged $Na^+$ ions, accelerating their diffusion and in turn achieving high ionic conductivity. Lei *et al.* adopted a different strategy, where they used an ionic conductor instead. $Al_2O_3$ nanowires in a PVdF–HFP host enhanced the ionic transport, and achieved a high Na deposition reversibility.[66] In addition to their high ionic conductivity, GPEs can also mitigate against polysulfide dissolution at the S-cathode, which we discuss in greater detail in Section 3.1.3.

Despite their benefits, the ductility of most GPEs are inadequate to suppress anode dendrite growth, especially at high charging rates.[68] In contrast, solid electrolytes (SEs) generally exhibit superior mechanical properties providing better resistance against dendrite formation, particularly when the level of defects within the SE pellet is minimal.[69-71] They possess further advantages such as good thermal stability as they do not contain a liquid phase, and the ability to conduct structural rearrangement even at the molecular level.[72,73] Generally, SEs may be categorized accordingly as *(1)* inorganic solid electrolytes (ISEs), *(2)*

solid polymer electrolytes (SPEs), and *(3)* ceramic/polymer composite electrolytes (CPEs).[74] Amongst these, ISEs are typically ceramic materials with high ionic conductivity, and have high thermal stability suited for operation at relatively high temperatures.[75,76] Recently, Wenzel *et al.* probed the interfacial stability of Na in conjunction with β″-$Al_2O_3$ and $Na_3PS_4$ using time-resolved impedance and polarization resistance measurement with X-ray photoelectron spectroscopy.[77] While β″-$Al_2O_3$ exhibited superior chemical stability, $Na_3PS_4$ promoted continuous growth of an S-containing SEI directly over Na metal surface, which was observed to affect the reaction kinetics and strongly deteriorated the cell performance. Though the use of ISEs ensures near-absolute dendrite suppression, the main challenge is in maintaining a firm ionic interface between ISEs and the Na metal anode. Honma *et al.* ingeniously bypassed this obstacle by combining $Na_3Zr_2Si_2PO_{12}$ material (*i.e.* Na Super Ionic CONductor, abbreviated as NASICON) with a glass electrolyte ($60Na_2O–10Nb_2O_5–30P_2O_5$).[78] The authors repurposed an earlier glass (with $Li^+$ ion conductivity on the order of $10^{-6}$ S $cm^{-1}$),[79] as filler material by replacing $Li_2O$ with $Na_2O$. The resultant mixture of 90 wt% NASICON with 10 wt% glass exhibited a higher $Na^+$ ion conductivity of $1.2 \times 10^{-4}$ S $cm^{-1}$ at r.t.[78] More recently, Yu and Manthiram designed an ISE and demonstrated its application in Na-S full cell configuration, by altering the surface structure of NASICON.[80] To improve the typically poor ionic interface between NASICON and the Na-metal anode, a thin polymer of intrinsic nano-porosity (PIN) was formed by dip-coating on the NASICON pellet (∼20 μm). Compatibility of the ISE with a S-cathode was also demonstrated with both potentiostatic and galvanostatic data showing stable cycling up to a C-rate of C/3 (**Figure 5**a,b). Further comparison to a common Celgard separator also showed that PIN-NASICON was able to prevent polysulfide shuttling, with Coulombic efficiencies maintained close to 100% over 100 cycles (Figure 5c).

In connection to glass electrolytes, Braga and coworkers worked extensively and reported various glass electrolyte systems for both Li and Na ion conduction.[81,82] They were

the first to report on anti-perovskites $A_3OCl$ and their doped glassy amorphous form as the electrolyte (*i.e.*, $Na_{2.99}Ba_{0.005}OCl\ x(OH)_x$) for Na-metal batteries, which could achieve reversible Na deposition for over 100 cycles. However, the overpotential was observed to increase with cycle number. The glass electrolyte could achieve an ionic conductivity of ~63 mS $cm^{-1}$ at 60 °C, and could also have potential applications in r.t. Na-metal batteries. The electrolyte was claimed to exhibit double layer charging behavior instead traditional diffusion phenomenon of ions, as schematically depicted in Figure 5d. Such ability of glass electrolytes to promote reversible stripping/plating of Na metal without getting reduced itself at the anode surface invites a complete rethink of strategies for rechargeable batteries.

## 2.2. Interface engineering to enhance stability of Na anode

### *2.2.1. Sodium metal/electrolyte interface and dendrites*

We have since discussed the importance of the SEI, which can be considered as a thin passivating layer acting as an *interphase* between the electrode and liquid electrolyte, mimicking a *solid electrolyte* with high electronic resistivity, hence its name.[83] Its stability exerts a profound influence on cell performance, as $Na^+$ ions are plated onto or stripped from the underlying Na metal during cycling. The electrochemical deposition/dissolution reaction takes place sequentially according to the following steps: *(1)* electron transfer at metal/SEI interface, *(2)* migration of cations from one interface to the other, and *(3)* ion transfer at the SEI/electrolyte interface.[84,85] Through various experimental techniques, *step 2* is identified to be the rate-determining step, and controls nucleation of the metal deposit. The thickness of the freshly formed passivating film can be estimated theoretically (by determining the electron-tunneling range) as well as experimentally.[86] For high performance batteries, the SEI must be compact and electronically resistive to avoid constant consumption of the organic species, resulting in SEI thickening and further leading to high internal resistance, self-discharge, and low Coulombic efficiency.[83,86] The first layer close to the metal electrode is thin (~10-20

nm) and compact, further covered by a porous layer (often assumed to be the second one). This upper layer is structurally open and suppresses the mass transport of ions. In terms of its chemistry, the SEI consists of ordered or disordered crystals (mostly salt anions with reduced organic species) which are thermodynamically stable with respect to metallic Na.[83]

Recent research efforts have identified that structural information down to atomic scale of moisture sensitive electrode materials (e.g., alkali metals) is difficult to be obtained under the conventional TEM.[87] For example, Na metal, which is notoriously reactive towards moisture, corrodes radially upon transfer of the sample into TEM column. In addition, Na metal is prone to vaporization under electron beam irradiation (due to its low melting temperature) which contributes to localized heating, posing a risk to the imaging process and the instrument. To overcome these challenges in characterizing moisture sensitive electrode materials, Li *et al.* and Zachman *et al.* independently utilized cryogenic techniques, originally developed for preserving hydrated biological specimens. Using cryo-transmission electron microscopy (cryo-TEM) and cryo-scanning transmission electron microscopy (cryo-STEM) techniques respectively, they were able to access the structural and chemical information of Li dendrites and the interphases down to the atomic scale.[87,88] While cryo-TEM or STEM, and *in-situ* TEM analyses have been conducted to study structural irregularities on Li metal anode, structural evaluation of the Na metal anode remained challenging. Most recently, Kumar *et al*. performed cryo-TEM to study localized structural irregularities of the Na metal anode, and revealed that Na dendrites are defect free single crystals preferring to grow along the $<00\bar{2}>$ direction of Na metal, which could be due to low surface energy along this direction.[89] Based on their relative sizes and distribution density, dendrites can be categorized in two classes: *type-I* (often tiny and regular in shape and size), and *type-II* (nano-or micro-needle shaped particles).[88] Han *et al.* used atomic force microscopy (AFM) to visualize Na dendrites on a thin layer of gold at three different stages, namely, nucleation, growth, and dendrite formation, and examined the formation of type-I dendrites at low current densities.[90] The

insights gained from these advanced characterization tools lead to a detailed understanding about the failure mechanisms in high energy batteries. Understanding structural and crystallographic changes in Na dendrites in different environments can potentially be used to explain the efficacy of certain electrolyte systems. Besides conventional X-ray photoelectron microscopy (XPS) and time-of-flight secondary ion mass spectroscopy (TOF-SIMS), Rutherford backscattering spectrometry (RBS) was recently used to probe the properties of the SEI over Na anode, as a highly versatile tool to unravel chemical and physical properties.[91,92] For non-destructive analysis, nuclear magnetic resonance (NMR) spectroscopy is also an advanced and indispensable tool to probe the microstructure of Na dendrites.[93] More recently, Kondou *et al.* devised a new method to track the uniformity of the Na deposition process through monitoring thermal reactivity of Na metal (*e.g.*, shape and size of heat flow peaks are largely related with quality of the deposition).[94]

As discussed above, many advanced characterization tools or methods have been devised to probe the SEI and nature of Na dendrites. Unlike Li anodes, there are several fundamental questions that have yet to be answered, for instance, how does ionic non-uniformity lead to dendrite growth? Through literature review and our personal experience, we realize that any one of these techniques alone is not enough to obtain detailed understanding of the SEI or dendrite growth. New combinatorial techniques, which include the synchrotron radiation-based X-ray absorption spectroscopy (XAS) in combination with X-ray imaging, or Raman spectroscopy with 3D optical imaging facility, are expected to offer new insight of Na anodes.

### *2.2.2. Intrinsic interphase formation*

The interphase can be developed by *intrinsic* as well as *extrinsic* (*i.e.*, artificial) means directly over the Na metal anode. The intrinsic interphase is self-growing and develops instantly in contact with electrolyte, where its properties are solely controlled by the

electrolyte, for instance by chemical potential or redox potential of the organic solvent, nature of the Na salt, and reduction potential of additive cations or organic molecules, which are obviously complex in practice.[95] Electrolyte components, in particular additives, have been examined to improve the health of the SEI by suppressing or regulating dendrite growth.[90,96-99]

Additives, whether a cation or organic molecule, can reduce, decompose, adsorb, or polymerize directly over the Na metal anode, in the process substantially modifing both physical and chemical properties of the SEI, and therefore altering the deposition morphology. Among the known additives, fluorinated compounds have been widely examined. For example, a trace amount of HF and $H_2O$ in ether-based electrolytes promote the formation of dense and uniform NaF/$Na_2O$ interphase directly over Na anode, which is found remarkable in producing dendrite-free deposition morphology.[35] However, the charge transfer resistance is noted to inecrease after 10 stripping/plating cycles, which could be due to partial blocking of HF molecules, as the SEI eventually becomes too thick for HF to reach to Na anode. Other combinations, such as $NaN(SO_2CF_3)_2$, (NaTFSI), NaFSI, $NaSO_3CF_3$ (NaOTf), and $NaClO_4$ with various ethers (*e.g.*, monoglyme, diglyme, and tetraglyme) and carbonates, *e.g.*, EC/DEC and EC/DMC, have also been examined by numerous groups, but due to lack of HF species in these electrolytes, a stable cycling could not be achieved. It is noteworthy that $NaPF_6$ in combination with EC/DEC or EC/DMC leads to a mixed organic-inorganic SEI instead, which is reported to be permeable to solvent molecules and prone to Na dendrite growth. Though carbonate solvents have higher reduction potential compared to ethers and are susceptible to reduction at the Na anode, their reactivity can be suppressed using fluoroethylene carbonate (FEC) as additive or co-additive, as examined by Dugas *et al.* and Lee *et al.*[96,100] FEC is a popular electrolyte additive known to be reduced earlier than EC/DEC or EC/DMC, forming a homogeneous and compact NaF film over Na anode. However, due to continuous reduction, the charge transfer resistance increases with cycle

number. Inorganic electrolyte additives such as KTFSI, $Na_2S_6$, $SiO_2$ nano-particles, $SnCl_2$, and $InI_3$ have been explored[11,99,101-103] hitherto to improve the health of the Na anode SEI, and may be categorized into two classes: *1)* cations that are reduced and adsorbed onto Na anode without forming an alloy, and *2)* cations that are reduced with consequent formation of a localized metal alloy.

Additives like KTFSI have $K^+$ cations which preferentially reduce and adsorb on the Na anode, electrostatically guiding the flux of $Na^+$ ions to suppress dendrite growth. As a result, Na anodes could be cycled for over hundreds of hours at higher capacities (*e.g.*, 2 mA $cm^{-2}$), see **Figure 6**a.[99] Unlike $Li_2S_8$-$LiNO_3$ co-additives in Li-S batteries,[104] Wang *et al.* demonstrated that the $Na_2S_6$-$NaNO_3$ counterpart has an adverse effect on the stability of Na metal anodes, which sheds light on the fundamental differences between Li and Na anodes.[101] They demonstrated that an optimized concentration of $Na_2S_6$ (0.33 M with 1 M $NaPF_6$ in diglyme) generated a stable interphase, see Figure 6b, which leads to uniform Na deposition even at high current density up to 5 mA $cm^{-2}$. In addition, a highly reversible Na anode could be designed by pre-treating Na metal surfaces with electrolyte solution. Wei *et al.* identified that an ionic liquid in conjunction with $SiO_2$ nano-particles could be used as additive to repair the Na anode interphase and to promote a uniform and dense Na deposition.[11] The 1-methyl-3-propylimidazolium-chlorate ionic liquid-tethered silica nanoparticle ($SiO_2$–IL–$ClO_4$) additive was observed to play dual roles in promoting uniform Na deposition: *1)* the tethered ionic liquid forms a mechanically robust and chemically stable SEI layer, while *2)* abundant surface sites at $SiO_2$ nano-particles served as anchors for $ClO_4^-$ anions, thus reducing the electric field through the tethered anion effect. With the assistance of the non-alloying type electrolyte additives, the Na metal anode could realize a uniform SEI and long cycle life over several hundreds of hours.

On the other hand, alloying electrolyte additives, undergo reduction to form an alloy with Na, instead of experiencing conventional electrostatic adsorption on Na metal. Several varieties of salts can serve as electrolyte additives, but only a few qualify as alloy-forming additives. The additive must contain a metal cation capable of forming an alloy with Na metal upon reduction, while the counter-ion could be a complex of one or more anions. A criterion of an alloying-type additive is that the reduction potential of its cationic component must be sufficiently positive with respect to the Na electrode.[105] A more positive reduction potential favors the occurrence of spontaneous redox reactions that form the localized metal-alloy interphase. For example, the reaction between $Sn^{2+}$ and Na metal can be considered spontaneous, as the Gibbs free energy ($\Delta G = -nF\Delta E$) for the reaction is highly negative ($Sn^{2+} + 2e^- \rightarrow Sn$, E = –0.14 V *vs.* SHE, and $Na \rightarrow Na^+ + e^-$, E = 2.71 V *vs.* SHE, which makes $\Delta E$ positive, and $\Delta G$ negative). Zheng *et al.* recently introduced a small amount of $SnCl_2$ (50 mM) in carbonate electrolyte to facilitate the spontaneous reaction between $SnCl_2$ and Na metal, which enables the formation of Na-Sn alloy and a mechanically robust NaCl-rich SEI layer directly over the Na anode, see Figure 6c.[102] $SnCl_2$ reduces to $Sn^0$ upon contacting Na metal due to hyper-reductivity of metallic Na towards $Sn^{2+}$, with Sn subsequently forming an alloy with bulk Na. Meanwhile, $Cl^-$ anions contribute to the formation of an electrically insulating NaCl-rich layer, which is indeed highly desirable and further passivates Na metal against unwarranted reactivity of the electrolyte solvent. The as-formed interphase allows fast and uniform Na deposition, achieving a dendrite-free morphology instead of dendritic or mossy Na structure. As a result, symmetric Na//Na cells could be cycled for over 500 hours at 0.5 mA $cm^{-2}$, as depicted in Figure 6d. In another recent example, Xu *et al.* utilized a small amount of $InI_3$ (10 mM) to form a compact localized Na-alloy interphase, exploiting the positive reduction potential of $In^{3+}$ *versus* Na.[103] Moreover, this film was identified to benefit polysulfide conversion reactions by the oxidation of iodine upon charging. The $InI_3$ additive acted as redox mediator to greatly improve the deposition morphologies by guiding the flux of

$Na^+$ ions, and helped to form a protective layer on Na metal anode against polysulfide corrosion, also improving the transformation kinetics of $Na_2S$ in cathode. Beyond existing electrolytes additives (performance comparison is provided in **Table 2**), new additive systems with the advantages of uniform Na deposition, improved safety, and low cost need to be developed to address current issues in Na metal batteries.

*2.2.3. Extrinsic interphase engineering*

In addition to intrinsic interphases, artificial or *ex-situ* interphases are very promising as they offer a significantly greater level of control and precision over their design, and are commonly produced prior to cell assembly. As a result, direct contact of electrolyte solvent with the Na anode can be avoided, preventing unnecessary consumption of both solvent and anode material itself.[89,105] Artificial interphases also offer several advantages over intrinsic interphases, which include the fact that *1)* side reactions can be mitigated immediately from the outset, unlike a bare Na anode that reacts on first contact with the electrolyte. Also, the *2)* SEI thickness can be controlled with a great degree of accuracy, *3)* interphases are generally more uniform compared to that of intrinsic interphases, *4)* artificial interphases do not grow with cycle number unlike intrinsic interphases, and they possess *5)* superior mechanical and chemical properties to intrinsic interphases.[106] Owing to these obvious advantages, development of artificial SEIs has grown tremendously in the past few years, as discussed in this section.

Artificial SEIs can be developed by controlled exposure of Na to chemicals (employing *solid-liquid*, *solid-vapor*, or *solid-gas* approaches) or through the use of specific materials that are adhesive towards the surface (*i.e.*, *solid-solid* approach).[107-109] Choudhary *et al*. designed an artificial interphase based on the *solid-liquid* approach. By allowing Na metal to react with 1-bromopropane ($C_3H_7Br$) in an inert atmosphere (Figure 6e), an NaBr interphase was formed and characterized by experimental and theoretical tools.[107] The

interphase was observed to be dense and rough, with thickness of the interphase noted to increase linearly with reaction time (~2 μm $min^{-1}$). The surface diffusion barrier for NaBr was further compared with other halides (*e.g.*, NaF, NaCl and NaI), and identified to be the lowest due to its high interfacial conductivity and excellent crystallinity. Attributed to the presence of NaBr, the treated anode could be cycled stability for over 250 cycles at 1 mA $cm^{-2}$ as depicted in Figure 6f. It is apparent that the interphase comprising NaBr not only blocks dendritic growth, but also minimizes unwarranted side reactions between the electrode and electrolyte solvent. Besides NaBr protection, Archer and co-workers also investigated the effectiveness of a halide-free interphase, *i.e.*, Na-Sn interphase (~2 μm), which was developed by reacting Na metal directly with tin bis(trifluoromethanesulfonyl)imide (SnTFSI).[108] The electroless reduction of $Sn^{2+}$ was found to favor the formation of a hybrid alloy interphase on either Li or Na metal. Protected Sn–Na symmetric cells functioned stably for over 1600 h at 0.25 mA $cm^{-2}$, compared to pristine Na cells which experienced large overpotentials > 1 V after just 250 h. In order to achieve improved adhesion and ionic conductivity of the interphase, electro-polymerization of different functional imidazolium cation-based ionic liquid monomers, *e.g.*, 1,3-diallyl imidazolium perchlorate (DAIM) has been examined by Wei *et al.*[109] The ionic polymer membrane effectively protects Na metal against parasitic reactions with the solvent, without compromising ionic transport in the SEI. They reduced or distributed the electric field on the Na surface, allowing uniform Na deposition for at least 50 hours at 1 mA $cm^{-2}$. However, Na deposition remains notoriously unstable at high current densities (>2 mA $cm^{-2}$). To address this limitation, Wang *et al.* devised a new strategy of pre-passivation to stabilize the Na metal anode at higher current densities (1-10 mA $cm^{-2}$).[101] The SEI formed with $Na_2S_6$ as pre-passivation agent consists mainly of $Na_2O$, $Na_2S_2$, and $Na_2S$, which are mechanically robust and chemically stable enough to protect Na metal anode from further reaction with the electrolyte solvent. Even at high current densities of up to 10 mA $cm^{-2}$, stable voltage profiles were maintained over 100

cycles, with low overpotentials of approximately 52 mV. Other pre-passivating agents such as $NaNO_3$ did not perform as well likely due to its higher reactivity than $Na_2S_6$. Thus, both spontaneous and non-spontaneous reaction methods are promising strategies to design the artificial SEIs on Na metal anode.

We have seen thus far that the solid-liquid approach leads to chemically and mechanically robust interphases, but offers little control over the interphase *thickness*, which also inevitably contains organic impurities.[101,108] Recently in 2020, Kumar *et al*. devised a new *solid-vapor* method which eliminates direct contact of liquid chemicals with Na metal.[89,105] Volatile liquid vapors were used instead of liquid precursors, and fast growth of the interphase (~0.15 μm $s^{-1}$, 5-10 s exposure duration) can be realized without concurrent formation of any impure phases. Process steps are schematically illustrated in **Figure 7**a. For example, ammonia vapor was used as precursor to develop the interphase (*i.e.*, biphasic interphase) comprising chemically and mechanically distinct phase of amide-hydroxide compound directly over Na metal anode.[89] Attributed to the high Young's modulus of NaOH and ductility of $NaNH_2$, the biphasic interphase allowed stable Na deposition for over 500 cycles at extremely high current densities (up to 50 mA $cm^{-2}$), see Figure 7b. The effectiveness of the interphase was investigated using cryo-TEM before and after cycling, and identified to be effective in blocking the emergence of Na dendrites. Besides ammonia vapor, other volatile liquids, such as tin tetrachloride ($SnCl_4$), silicon tetrachloride ($SiCl_4$) and titanium tetrachloride ($TiCl_4$) were also examined by Kumar *et al*.[105] A uniform interphase comprising Na-Sn and a thin layer of NaCl was produced directly over the Na metal surface. The surface diffusion barrier of the Na-Sn interphase was also calculated to be significantly lesser than that of the pristine Na surface. These strategies are therefore unique and highly versatile for developing novel artificial interphases with synergistic material combinations.

The *solid-gas* approach has also been widely applied to fabricate artificial SEI and protective films for Na metal anodes.[110-112] Among them, atomic layer deposition (ALD) is

extensively utilized in due to its obvious advantages, which include a high level of control in the deposition of thin films, avoidance of side reactions, and improved adhesion with the underlying surface. Schematics are shown in Figure 7c. Both ALD and plasma-enhanced ALD-grown $Al_2O_3$ have been found to enhance stripping/plating stability of the Na anode at relatively high current densities (0.5-3 mA $cm^{-2}$) in both ether and carbonate-based electrolytes, see Figure 7d.[110] Besides its high performance, the polarization potential was observed to the same, indicating high ionic conductivity of $Al_2O_3$ films.

As an extension of the solid-gas approach, molecular layer deposition (MLD) has been further employed for its enhanced thermal and adhesive properties. For example, the oxidizing precursor in ALD (*e.g.*, $H_2O$ and $O_2$) can be replaced with organic linkers or added to a molecular fragment into the film to further strengthen adhesion with the substrate. Zhao *et al*. demonstrated the application of MLD alucone (produced by reacting trimethylaluminum and ethylene glycol) in developing an organic-inorganic interphase over Na metal. The Na anode with MLD grown protective layer was shown to exhibit prolonged cycling and extremely low polarization potential at various current densities (1-3 mA $cm^{-2}$). Indeed, both ALD and MLD are effective tools to engineer artificial SEIs with excellent thickness control at relatively low temperatures.[112]

Additionally, the *solid-solid* approach can be used to develop interphases without direct reaction with the Na anode. In other words, precursors can either be physically or chemically attached to the Na metal surface, forming the artificial interphase.[113,114] From theoretical calculations of various 2D materials,[113] it was identified that the crystalline quality, defect patterns, increase in bond length, and proximity effect could favorably increase the ionic conductivity and surface diffusion properties. However, all materials were found to negatively impact the hardness or stiffness required to suppress dendrite growth. Unlike the case for Li, defective hexagonal-boron nitride (h-BN) or graphene was not favorable for Na anodes, likely due to the $Na^+$ ionic radius being much larger and diffusion more difficult

(calculated barrier > 3 eV), leading to poor ionic conductivity. On the other hand, relatively high surface diffusion of $Na^+$ in materials like silicene with vacancies was predicted, and these interphases were also shown to exhibit stronger mechanical properties than common SEIs. Materials with puckered structures (*i.e.*, bent non-planar rings) such as SnS, SnSe, and phosphorene were predicted to be worse in blocking dendrite growth due to poor mechanical properties. In addition, Snydacker *et al.* developed an open quantum materials database (OQMD) to identify electronically insulating materials (*i.e.*, transition metal compound films) that exhibit a stable equilibrium with the Na anode.[114] They identified 118 of such coatings (including binary, ternary, and quaternary compounds of oxides, nitrides, sulfides but no fluorides) that are both chemically stable with respect to Na metal and are electronically insulating. In spite of the theoretical ineffectiveness of graphene in stabilizing Na metal anodes, Wang *et al.* employed a graphene-PMMA transfer method, with process steps are depicted in Figure 7e.[115] An optimized thickness of about 5 nm (approximately 15 layers of graphene) led to the best performance in carbonate electrolyte without any additives for over 100 cycles, at a current density of 2 mA $cm^{-2}$. More importantly, it should be emphasized that minute differences in graphene film thickness (by just about 2-3 nm) could instead have decisive influence on the stability and rate capability of the Na anode, illustrating that precise control is critical in handling the materials. Another 2D material, $MoS_2$ was identified to be chemically reactive towards Na metal, unlike graphene which is chemically inert.[116] Zhang *et al.* demonstrated a novel means to develop artificial interphases by application of $MoS_2$ flakes directly over Na metal, followed by repeated folding and rolling unto itself.[116] They identified the simultaneously formation of an artificial SEI and 3D-host structure for Na, *via* a conversion reaction: $4Na + MoS_2 \rightarrow 2Na_2S + Mo$. The excellent Na stripping/plating was ascribed to the unique SEI composition and structure, where uniform $Na_2S$ dispersion effectively suppressed dendritic growth, and the stable host formed by $MoS_2$ nanosheet fragments serves to accommodate volume changes with cycling. Kim *et al.* presented a simple

yet effective approach by exploiting an inorganic-organic free-standing composite protective layer (FCPL), which comprised mechanically stable $Al_2O_3$ inorganic micro-particles and liquid electrolyte-swollen PVdF-HFP polymers,[117] see Figure 7f. Due to the ductility of Na metal, the FCPL can be tightly attached to the metal surface even at r.t., and could also easily be laminated over the Na metal surface by roll-pressing. The as-designed composite electrode effectively suppressed Na dendrite formation and consequently improved cycling stability. The strategies to design artificial interphases and their effectiveness in stabilizing Na metal anode are summarized in **Table 3** for comparison.

*2.2.4. Localized surface polishing to realize ultra-smooth surfaces*

As discussed earlier, the exact origins of Na dendrite growth are not well understood, but often relates to non-uniform electric field distribution leading to an uneven ion flux. These detrimental factors are inherently correlated with surface roughness, as well as chemical or mechanical inhomogeneity of the SEI inevitably formed on the metal surface. From previous studies on Li metal anodes, surface irregularities are known to act as kink sites for nucleation, while chemical inhomogeneities in the SEI induce dendrite growth.[85] The design of a smooth electrode surface has been pursued for a long time, but is exceptionally challenging to achieve by existing approaches.[118,119] Electrochemical polishing, one of the oldest known techniques to create smooth surfaces down to atomic flatness, creates ultra-smooth surface on metals by selectively removing specific atoms/ad-atoms from the outer surface of the metal electrode. Gu *et al.* established a straightforward but effective protocol to form atomically smooth (0.6-1.5 nm surface roughness) alkali metal anode surfaces,[120,121] with highly anodic potentiostatic stripping, during which dissolution of Na atoms and electrolyte reduction takes place. This is followed by galvanostatic plating, during which Na deposition and further reduction of the electrolyte occurs, creating near-perfect Na or Li metal anodes with near-ideal SEIs. Owing to finely tuned electrochemical processes, a multilayered SEI (mixed

inorganic/organic-layered structures) was obtained over alkali metal anodes, in contrast to the traditional mosaic model of the SEI.[83] The SEIs exhibited excellent mechanical properties coupled with desirable rigidity (stemming from its inorganic components) and elasticity (due to organic components). It is worth mentioning that the structure and thickness of the SEIs largely depends on electrochemical polishing steps. For example, a *soft-stiff* interphase without a passive layer was formed with a single polishing step, while multiple polishing steps led to *stiff-soft-stiff* interphases. The stiff-soft-stiff interphase was identified to be superior (500 cycles at 10 mA $cm^{-2}$) to either soft or stiff interphases alone. These findings are in contrast to previous studies on purely inorganic or organic interphases.[89,105] Such near-perfect alkali metal surfaces with tunable SEI structure provide tremendous opportunities in diverse fields including surface science, nanotechnology, and energy technologies.

## 3. Engineering sulfur-based cathode architectonics

### 3.1. Solid-liquid-solid conversion systems

In a generic S-cathode containing bulk elemental $S_8$ as active material, sodiation is expected to proceed *via* a multistep *solid-liquid-solid* phase transition. While both charge and discharge end-products (*i.e.* $S_8$ and $Na_2S$) respectively exist in the solid phase, long-chain polysulfide intermediate species ($Na_2S_x$, where $4 < x \leq 8$) easily dissolve in ether-based electrolytes, and react irreversibly in the presence of alkyl carbonate solvents. At the cathode-electrolyte interface, solid elemental $S_8$ first undergoes reduction to long-chain polysulfides that dissolve into the electrolyte. Left on its own, these polysulfides can migrate to the anode, become chemically reduced and trapped in the shuttle effect. An obvious solution to alleviate this is preventing the dissolution of long-chain soluble polysulfides, with *adsorption* and *conversion* being the two key strategies. Strong polysulfide adsorption sites could effectively immobilize long-chain polysulfides on the cathode surface, while electrocatalysts are able to promote the

conversion of long-chain polysulfides to insoluble short-chain species, reducing the polysulfide content in the electrolyte. The flow of polysulfides can also be impeded either through strong *chemical interactions* or with *physical barriers*, because the migration of polysulfides are obstructed or the diffusion path of polysulfides are cut off completely. While these innovations alleviate dissolution and shuttling, there are associated benefits and limitations with each approach. In this Section, we first discuss polysulfide adsorbents and electrocatalysts, followed by encapsulation strategies, polymer-based electrolytes, ion-selective membranes and finally solid-state electrolytes.

### *3.1.1. Polysulfide adsorbents and electrocatalysts*

To date, various efforts have been taken to alleviate polysulfide shuttling. One of the most effective approaches is to anchor long-chain polysulfides, immobilizing them to prevent diffusion into the electrolyte. To achieve this, the construction of sulfiphilic sites that exhibit high affinity to polysulfide species is the key goal. One of the most widely investigated sulfiphilic materials are carbonaceous hosts which exhibit large surface area and good conductivity. For example, a carbon nanofoam inserted between the separator and the S-cathode has proven effective as a secondary current collector to capture and retain polysulfides, while S-cathodes fabricated by self-weaving multiwall carbon nanotube (MWCNT) as matrix could also localize the soluble Na polysulfides to alleviate their migration.[122,123] Although the discharge capacity of the Na-S battery with MWCNT fabric electrode remains at around 400 mAh $g^{-1}$ after 30 cycles, weak physical interaction and the non-polar nature of these carbon-based materials is far from fully suppressing polysulfide migration. In order to enhance the interaction between carbonaceous sulfiphilic hosts and polysulfide species, stronger chemical bonds are favored. Saroja and coworkers proposed that Teflon-lined conductive carbon substrate (TCS) would benefit from its covalent bonding

between the fluorine in Teflon and polysulfides.[124] Kumar *et al*. constructed C-S bonds by activating sulfiphilic sites on the surface of carbon matrix.[125] They activated carbon cloths through alkali treatment at elevated temperature which generates unpaired electrons (*i.e.* dangling bonds) on its surface. These unsaturated carbon atoms undergo free-radical coupling with the $S_3^{\bullet-}$ radical monoanions from the dissolution of polysulfides, and then instantly form sturdy C-S bonds and anchor polysulfides on the surface of carbon matrix. These chemical bonds facilitate electron transfer from the substrate that leads to further reduction of sulfur to form $Na_2S_2$ and $Na_2S$ as the discharged end-product through a reversible free-radical catalysis process, boosting performance to 678 mAh $g^{-1}$ after 700 cycles at 0.5 C.

Besides non-polar carbon materials, metal-based sulfiphilic sites have also been introduced into S-cathodes due to their strong polar-polar interaction with polysulfide species which improves polysulfide immobilization. For instance, metal oxide additives such as $TiO_2$ have been investigated as it substantially polarizes the cathode surface, providing strong polysulfide adsorption.[126] As reported by Ma and coworkers, $TiO_2$-nanolayer-coated porous free-standing C/$BaTiO_3$ (CSB@$TiO_2$) was synthesized and utilized as Na-S cathodes. 3 wt.% of commercial $BaTiO_3$ nanoparticles were well-dispersed inside the carbon matrix, followed by the direct deposition of a 4 nm-thick amorphous $TiO_2$ layer by ALD. Both compounds are active sulfiphilic sites for polysulfide adsorption, especially $BaTiO_3$ which is a widely accepted ferroelectric material with spontaneous polarization capable of generating an internal electric field. During cycling, the heteropolar polysulfides are first adsorbed by $BaTiO_3$ nanoparticles, while excess polysulfides are confined by the outer $TiO_2$ nanolayer, leading to improved cycling performance. As a result, the CSB@$TiO_2$ cathode shows stable cycling at 0.5 A $g^{-1}$ with a discharge capacity of 611 mAh $g^{-1}$ after 400 cycles, much higher than the 340 mAh $g^{-1}$ discharge capacity for the cathode without sulfiphilic sites.

Similarly, Ghosh *et al*. incorporated manganese oxide ($Mn_xO_y$) as sulfiphilic sites into an rGO composite cathode, based on its excellent stability and polysulfide suppression ability

in Li-S batteries.[127] The mixed-valence $Mn_xO_y$ nanoparticles have a homogeneous particle size of 10-15 nm and are evenly embedded on the surface of rGO and hybrid Na alginate/polyaniline (SA-PANI) matrix. To further investigate the polysulfide affinity of $Mn_xO_y$, solid-state $^{55}$Mn NMR was conducted on the pristine $Mn_xO_y$ and polysulfide-adsorbed $Mn_xO_y$, separately. As shown in **Figure 8**a, two peaks of the $Na_2S_6$-adsorbed $Mn_xO_y$ sample exhibits a slight downfield shift compared to as-prepared $Mn_xO_y$ from -740.1 to -740.4 ppm and from -780.2 to -780.3 ppm, respectively, indicating a weak dipole-dipole interaction between polysulfide and $Mn_xO_y$. Interestingly, the new peak at -766.2 ppm is attributed to an intermediate oxidation state of manganese ($Mn^{n+}$; $2 < n < 4$), indicating a redox reaction between $Mn_xO_y$ and $Na_2S_6$. In addition, a simple visual experiment (Figure 8b) shows that the dark brown $Na_2S_6$ solution quickly turns to colorless after adding $Mn_xO_y$ nanoparticles, corresponding to strong polysulfide adsorption onto $Mn_xO_y$ particles. Figure 8c schematically demonstrates the adsorption of polysulfides on $Mn_xO_y$ surface due to proposed surface reactions.

Other than metal oxides, MXenes are promising 2D materials due to its polar surface and strong affinity to polysulfides.[128-130] Bao *et al*. synthesized S-doped MXene (S-$Ti_3C_2T_x$) sheets as the cathode material in Na-S batteries. According to density functional theory (DFT) calculations, S-$Ti_3C_2T_x$ MXene nanosheets possess a strong adsorption capacity for polysulfides. The binding energies between S-$Ti_3C_2T_x$ and various polysulfides species: $Na_2S_2$, $Na_2S_4$, and $Na_2S_6$ were calculated to be -1.887, -2.880, and -4.722 eV, respectively, implying effective polysulfide adsorption. The discharge capacity of the S-$Ti_3C_2T_x$/S composite can be maintained at 690 mAh $g^{-1}$ after 200 cycles at 0.5 C, with its successful alleviation of polysulfide dissolution.

The sulfiphilic nature of copper (Cu) metal also makes it a popular polysulfide adsorbing material for Na-S cathodes. Exploiting its high polysulfide affinity, Zheng and coworkers deposited Cu nanoparticles onto high-surface-area mesoporous carbon (HSMC)

using ultrasonic-assisted multiple wetness impregnation and synchrodry techniques.[131] Cu nanoparticles were uniformly distributed in the HSMC matrix and then partially sulfurized to Cu-polysulfides $CuS_x$. In this regard, the new chemical bonds formed were purported to aid polysulfide immobilization. Li and coworkers subsequently used high surface area Cu foam as the cathode current collector, with evidence showing that Cu foam had a considerable polysulfide adsorption capacity of over 5 mg $cm^{-2}$ of sulfur.[132] The polysulfide immobilization not only came from the chemical reaction turning Cu into $Cu_2S$, but also by the polar-polar interactions between $Cu_2S$ and polysulfides. In another study, Zhang and coworkers observed an extremely high capacity of 3189 mAh $g^{-1}$ in the first discharge and 1403 mAh $g^{-1}$ in the first charge process when *in situ* grown S nanosheets with Cu foam current collector were used as the cathode.[133] They argued that, other than chemical immobilization and adsorption from polar-polar interaction, the high capacity could also be ascribed to the high electrochemical activity of S nanosheets, due to the Cu matrix acting as electrocatalyst. However, the battery experienced a steep capacity decay to only 377 mAh $g^{-1}$ within 5 cycles, due to instability of the cathode structure. Comparing these two Cu-based sulfiphilic species, we note that effective adsorption of polysulfide is also affected by the structural characteristics of the host, such as surface area and pore distribution.

In addition to the above examples based on the polysulfide immobilization approach, attaining fast electrochemical kinetics for the polysulfide redox reaction is another promising strategy to suppress serious polysulfide dissolution, and to enhance the energy efficiency and cycling stability of S-cathodes. Therefore, a number of *electrocatalytic materials* have been investigated to provide valuable insights into this process. Inspired by the role of active metallic catalysts in Li-S systems, Zhang *et al*. proposed that metallic catalysts would play a similar role in Na-S batteries.[134] They synthesized S-encapsulated atomic cobalt-hollow carbon nanospheres ($S@Co_n$-HC) as the cathode material to suppress polysulfide dissolution. In addition to the strong chemical bonds between the atomic cobalt (including single atom

cobalt and cobalt clusters) and polysulfide species, they proposed that the atomic Co could also accelerate the transformation of $Na_2S_4$ to $Na_2S$, improving the kinetics of the polysulfide conversion through electrocatalysis. To prove that atomic Co was electrocatalytically active, *in situ* synchrotron XRD (SXRD) was conducted in the initial charge/discharge (**Figure 9**a). In the beginning of discharge, only elemental sulfur (23.01°) was observed. Upon discharge to 1.8 V, a new peak at 22.97° evolves, representing formation of soluble long-chain polysulfides, $Na_2S_x$. Subsequently, $Na_2S_4$ (13.22°) gradually appears followed by the disappearance of $Na_2S_x$ at 1.4 V. When further discharged, the peak of $Na_2S_2$ was generated at 18.73°, and finally replaced by a peak at 17.07° attributed to the fully discharged $Na_2S$ product. This clearly shows the complete step-by-step discharge reaction from S to $Na_2S$, especially the solid-solid conversion of $Na_2S_4$ to $Na_2S$, which is rarely observed without metallic electrocatalysts.

The electrocatalytic process can be further explained by *ab initio* molecular dynamics (AIMD) simulations, as shown in Figure 9b. Initially, $Na_2S_4$ molecules adsorb on the $Co_6$ cluster with binding energy up to -0.64 eV. Spontaneous decomposition then follows over the catalytic sites. $Na_2S_3$, $Na_2S_2$, and $Na_2S$ clusters can be identified through the decomposition along with a rapid adsorption energy change from -4.33 eV ($Na_2S_4$), to -10.67 eV ($Na_2S$), which indicates the kinetically fast catalytic reaction. Figure 9c summarizes the rapid change in relative adsorption energies of these polysulfide clusters.

To validate the mechanism in fast $Na_2S_4$ decomposition, a two-step electrocatalytic mechanism is proposed.[135] Firstly, the polar surface of the electrocatalytic sites strongly adsorb dissolved long-chain polysulfides, which promotes further polysulfide nucleation on its surface. Secondly, the adsorbed particles are quickly converted to short-chain polysulfides through the fast-catalytic reactions. Due to the rapidly increasing bonding energy, the as-formed short-chain polysulfides immediately decompose to the final product $Na_2S$. This rapid polysulfide conversion largely reduces the dissolution of polysulfides in carbonate-based

electrolytes, therefore enhancing the cycling performance. To illustrate, Na-S batteries with metal-organic framework (MOF)-derived Co-containing N-doped porous carbon (CoNC) as sulfur host at the cathode provides a high capacity of 500 mAh $g^{-1}$ at 80 mA $g^{-1}$ after 150 stable cycles, indicating improved polysulfide conversion due to the existence of Co electrocatalytic sites.[136] Moreover, with S@$Co_n$-HC cathode, the batteries exhibit an initial reversible capacity of up to 1081 mAh $g^{-1}$ and a high reversible capacity of 508 mAh $g^{-1}$ at 100 mA $g^{-1}$ after 600 cycles.[134]

Inspired by the outstanding performance of atomic Co, a series of transition metals and metal sulfides are further demonstrated in Na-S batteries as electrocatalysts to circumvent the polysulfide issue. Ma and coworkers incorporated Co nanoparticles into a graphene aerogel, and achieved stable cycling performance at a high rate of 5 C with an average capacity fading of 0.01% per cycle, between 200 and 1000 cycles.[137] Zhang *et al*. implemented three transition metal (Fe, Cu, and Ni) nanoclusters separately in hollow carbon nanospheres (M-HC) as the sulfur host.[138] According to AIMD simulation results, Fe nanoclusters were most active in catalyzing the decomposition of $Na_2S_4$ among these transition metal candidates. The remarkable performance of Fe was further explained by Yan and coworkers.[135] They synthesized a composite cathode consisting of nitrogen-doped hierarchical carbon microspheres and $FeS_2$ nanograins with a high $FeS_2$ content of 14.5 wt%. The electrocatalytic behavior was verified *via* DFT calculations, in which $FeS_2$ exhibits small $Na^+$ ion diffusion barriers (0.071 to 0.149 eV), leading to fast ion diffusion on its surface. A few other transition metal sulfides were also proven as effective electrocatalysts, including $NiS_2$ nanocrystals and ZnS-$CoS_2$ crystals.[139,140] It should also be emphasized that the latter benefits from both high stability of ZnS and the good polysulfide suppression character of $CoS_2$, achieving outstanding cycling performance. The ZnS-$CoS_2$ cathode showed an extremely long cycling life with a capacity of 570 mAh $g^{-1}$ at 0.2 A $g^{-1}$ over 1000 cycles. At a

high current density of 1.0 A $g^{-1}$, it provided a capacity of 250 mAh $g^{-1}$ even after 2000 cycles.

Furthermore, the transition metals have also proven to facilitate the formation of S by electrocatalysis, during the re-charging process. Wang *et al*. successfully synthesized gold nanodots decorated hierarchical N-doped carbon microspheres (CN/Au/S) as cathode material in Na-S batteries.[141] Au nanodots with a mean size of 1.8 nm were uniformly distributed on the carbon host as sulfiphilic sites. Besides the promoted $Na_2S_4$/$Na_2S$ conversion during discharge, Au nanodots also induced a complete reverse reaction from $Na_2S_4$ to S. From *ex-situ* SXRD measurements during the charging process, $Na_2S_4$ intermediates were completely converted back to elemental S at 2.4–2.8 V, while some irreversible $Na_2S_4$ was detected when Au nanoparticles were absent. Nevertheless, the actual role of Au nanoparticles promoting conversion of $Na_2S$/$Na_2S_4$ during the charging process was not discussed within the work, and is an interesting aspect for future investigation.

Recently, an innovative hypothesis was proposed, providing valuable insights to both the polysulfide adsorption and electrocatalytic processes, and a better understanding of the mechanistic effects from metals and metal sulfide additives. Based on new research by Ye *et al*. on electron-state confinement effects, the change in electron-states of both electrocatalyst and S is responsible for their strong interaction during battery cycling.[142] They synthesized a 2D MOF, $Ni_2$(2-mer-captopyrimidine)$_4$ (Ni-MOF), by mechanical exfoliation of single layers from Ni-MOF-bulk material. During the exfoliation, due to the breaking of interlayer N···H hydrogen bonds, Ni-MOF-2D was observed to experience a charge redistribution in which the electron transfer from S to Ni results in a higher S valence state and a lower Ni valence state. Once the Ni-MOF-2D interacts with polysulfides (*e.g.* $Na_2S_5$), the electron from Ni then transfers to the polysulfides through its heterocyclic linker, resulting in strong polysulfide adsorption through electron donor/acceptor interaction between the linker and polysulfides,

thus leading to strong polysulfide confinement. Moreover, the charge redistribution also implies enhanced polysulfide conversion kinetics. Therefore, with an addition of 5% Ni-MOF-2D into the cathode material, a high discharge capacity of 347 mAh $g^{-1}$ was maintained after 1000 cycles under 1 C with a low capacity decay of 0.042% per cycle.

As summarized by **Table 4**, a number of metallic catalysts have been reported to date. When choosing appropriate sulfiphilic species/catalysts, several factors of the material that might influence the performance of Na-S batteries should be considered: *i*) adsorption capability towards polysulfides, *ii*) conductivity of sulfiphilic species/catalysts, *iii*) diffusion ability of polysulfides on these sulfiphilic species/catalysts, *iv*) the catalytic capability of conversion of $Na_2S_x$ ($4 \leq x \leq 8$) and $Na_2S_2$/$Na_2S$, and *v*) structural properties of the host that determine its surface area, pore distribution, and the exposure of active sites. Overall, there remains a long way toward practical applications of Na-S batteries attaining high-sulfur loading cathode with sulfiphilic species/catalysts. Moreover, the specific mechanisms of sulfiphilic species/catalysts in different electrolyte systems, such as ionic liquids or solid-state electrolyte, should also be explored in the future research.

*3.1.2. Towards hermetic encapsulation of active species*

With the previous section detailing approaches in Na polysulfide confinement and conversion, we further look at an approach striving towards the complete encapsulation of the active species. Hollow mesoporous carbon composites can serve as good host structures for sulfur. With pore diameters ranging from 2 nm to 50 nm, these structures generally have relatively high total pore volumes, allowing for a high S-content to be stored. It could also be envisioned that a hermetic seal encapsulating the active species within a large internal void could prevent polysulfide dissolution while at the same time maximizing the areal loading. In this case, soluble reaction intermediates would remain confined within the hollow structure *without* contacting the liquid electrolyte. Wang *et al*. first pioneered the use of hollow

mesoporous carbon spheres for r.t. Na-S batteries,[143] with the sulfur ratio reaching as high as 46%. Although sulfur was trapped within the internal void space, serious self-discharge was still observed due to gradual dissolution of long-chain polysulfides into the electrolyte through the mesopores.

Towards the design of materials for hermetic encapsulation of active sulfur and reactive Na polysulfides, Li and co-workers invented a hollow network of $Na_2S$ nanospheres contained within a carbon matrix.[144] This hollow nano-$Na_2S$ composite was prepared *via* a three-step process (**Figure 10**a). First, a solution containing $Na_2S$ and PVP was evaporated, precipitating the $Na_2S$-PVP agglomerates while maintaining the inherent double layer micellar structures. A process of vacuum evacuation and back-filling with argon gas was then repeated to inflate the PVP micelles into hollow spheres. Finally, carbonization of the polymer was carried out, trapping the $Na_2S$ internally within their individual hollow spheres and resulting in a spongy matrix similar to the morphology of frogspawn coral (Figure 10b). Unlike the majority of Na-S cathodes employing different forms of sulfur, the use of encapsulated $Na_2S$ addresses two major challenges: cathode pulverization could be avoided since the $Na_2S$-based cathode is effectively pre-sodiated and does not undergo further volumetric expansion. Also, capacity loss due to polysulfide dissolution can be mitigated against by an almost hermetic seal, since the active species remain trapped within the carbon matrix without risk of structural damage during cycling.

Furthermore, a high active material loading could be attained, with approximately 68 wt.% of $Na_2S$ contained in the composite. In an ether-based $NaPF_6$ electrolyte, galvanostatic charge/discharge profiles reveal the multi-step reaction starting from elemental $S_8$ to intermediate $Na_2S_x$ polysulfides (where x = 4-8) in a solid-to-liquid transition, occurring around the first voltage plateau at 2.2 V *vs*. $Na/Na^+$ (Figure 10c). This is followed by the transition of $Na_2S_4$ to the short-chain $Na_2S_2$ and $Na_2S_3$ species close to 2.1 V, and lastly the solid-solid conversion of $Na_2S_2$ to $Na_2S$ from the third plateau near 1.65 V and the final

sloping region. Initial capacities of up to 1127 mAh $g^{-1}$ and 980 mAh $g^{-1}$ could be obtained at current densities of 0.4 A $g^{-1}$ and 1.4 A $g^{-1}$ respectively, based on the weight of sulfur, and maintaining 600 mAh $g^{-1}$ after 100 cycles at 1.4 A $g^{-1}$. Thus, the demonstration of effective nano-$Na_2S$ encapsulation paves the way for newer designs of alternative architectures to physically trap reactive intermediates without compromising a high active material loading, at the same time mitigating against structural disintegration by volume expansion.

*3.1.3. Gel-polymer electrolytes*

Gel polymer electrolytes (GPE) in Na-S batteries were first tested by Park and coworkers in 2006.[19] GPEs generally comprise four components including the polymer matrix, liquid solvent as plasticizer, Na salt, and electrolyte additive. The polymer matrix provides the GPE with mechanical strength and keeps it in a quasi-solid state while the liquid plasticizer is mainly responsible for ion transport.[145] Thus, the GPE possesses both good mechanical property and high ionic conductivity. The authors benefited from these merits by employing PVDF-HFP, tetraglyme, and $NaCF_3SO_3$ in a ratio of 3:6:1 as GPE in Na-S batteries. During the first cycle, the battery is efficiently discharged with two plateau potentials of 1.73 V and 2.27 V, ascribed to the two reduction steps of sulfur, respectively. However, the cell experienced severe capacity decay and lost more than 90% of the discharge capacity within 20 cycles. This sharp capacity decay is due to extensive polysulfide dissolution, with the sulfur loss observed from the continuous decrease of the area of both reduction peaks and the length of the plateaus in cyclic voltammogram (CV) and discharge profile, respectively.

The same capacity decay was observed in several later studies as well. Kim and coworkers tested the same GPE with an increased current rate while Kumar and coworkers optimized the conductivity of PVDF-HFP GPE with $SiO_2$ filler and carbonate solvent.[146,147] Both Na-S systems experienced fast capacity decay within 10 cycles, and these efforts are proved unavailing in suppressing polysulfide migration, possibly due to the nature of PVDF-

HFP based GPE. Although the liquid solvents only take up 60% of the GPE, the ion transfer kinetics remain unchanged, which means both $Na^+$ ions and dissolved polysulfides can move in liquid plasticizers without any deterrent. Therefore, early GPE designs were less effective in preventing polysulfide dissolution and migration. The major problems are: *i*) liquid electrolytes in the GPE are typically good solvents for polysulfides, thus the polysulfide dissolution is inevitable;[148] *ii*) the pore sizes of PVDF-HFP are in micron-scale, which are sufficiently large to provide free paths for polysulfide migration.[149]

To solve the first problem, Li and coworkers inserted a layer of nanocarbon between PVDF-HFP GPE and the cathode to alleviate polysulfide dissolution.[150] The interlayer is synthesized by processing commercial nanosized carbon *via* high-energy ball-milling. Compared with the pristine carbon, the processed nanocarbon has much more vacancy defects, as confirmed by scanning transmission electron microscopy (STEM), Raman microscopy, and differential scanning calorimetry (DSC). These artificial defects have strong binding with the sulfur species. Based on DFT calculations, the adsorption energy **Figure 11**a between $S_8$ and the carbon surface reaches its highest value when two carbon atoms are absent. Meanwhile, the deformation charge density simulation Figure 11b also confirms that carbon with defects offer stronger binding than the defect-free carbon surface, thus efficiently trapping polysulfides in the carbon interlayer and reducing polysulfide dissolution. Moreover, the processed nanocarbon interlayer also helps to re-activate the dead sulfur formed on GPE to increase the reversibility of the batteries. As a result, Na-S batteries with nanocarbon coated GPE exhibit a stable reversible capacity of 700 mAh $g^{-1}$ for 200 cycles at 0.2 C, and outstanding Coulombic efficiency of 99.5%. Effective shuttling prevention is also verified by surface elemental analysis of the Na anode after cycling. No obvious sulfur signal can be detected by energy-dispersive X-ray spectroscopy (EDS).

Other than implementing an additional interlayer, Saroja and coworkers mixed boron nitride (BN, also known as white graphite) with the GPE (PVDF-HFP/poly (butyl

methacrylate) (PBMA)/1M $NaClO_4$), forming a composite electrolyte. The added BN not only increased the ionic conductivity of the electrolyte significantly, but also acted as anchoring sites for polysulfides and improved the cycling performance.[124] Furthermore, Zhou and coworkers synthesized a novel GPE which has the ability to bind polysulfides with its own functional groups.[151] This novel GPE consists of a (pentaerythritol tetraacrylate (PETEA)-tris[2-(acryloyloxy)ethyl] isocyanurate (THEICTA))-based copolymer matrix, 1 M NaTFSI in PC/FEC, and glass fiber. The ester group in PETEA monomers and the isocyanurate ring on THEICTA monomers exhibit high binding energy of -1.86 eV and -3.04 eV, respectively, according to first principle calculations in **Figure 12**a with $Na_2S_6$ as a representative polysulfide species. The binding between $Na_2S_6$ and the (PETEA-THEICTA) copolymer is much stronger than its binding with the PC/FEC liquid electrolyte (-1.57 eV and -1.22 eV, respectively). Therefore, rather than dissolving in the carbonate solvent, polysulfides can be strongly immobilized on the GPE.

Na-S batteries with this new GPE maintained a reversible capacity at 736 mAh $g^{-1}$ after 100 cycles, which is around twice the capacity of their liquid electrolyte counterpart. It is worth noting that successful inhibition of the shuttle effect was further validated by the surface elemental analysis of the Na metal anode after cycling. Field emission scanning electron microscopy was conducted (FE-SEM) on Na anodes (paired with polymeric sulfur cathode, disassembled after 100 cycles). As shown in Figure 12b, massive dendrites and holes were observed on the Na surface after cycling in liquid electrolyte. In contrast, the Na anode tended to have less dendrites and showed a smoother surface with the GPE. Moreover, the S-content on the Na anode decreased dramatically from 8.96 wt% to 0.96 wt.% attributed to (PETEA-THEICTA) copolymer GPE.

*3.1.4. Ion-selective membranes*

In the example above, a small amount of polysulfide crossover to the anode still occurred despite the effectiveness of the GPE in mitigating polysulfide dissolution. As we highlighted in the previous section, controlling the porosity and/or pore size of the separator is another key aspect towards absolute inhibition of polysulfide migration. To this end, ion-selective membranes were applied to Na-S batteries.

Nafion is accepted to be one of the most widely used ion-selective membranes. Sodiated Nafion (Na-Nafion) has been shown to be suited for $Na^+$ ion transfer in Na-ion batteries.[152] Following this, Bauer and coworkers employed Na-Nafion as a polysulfide blocker in Na-S batteries.[21] The composite electrolyte is composed of a porous polypropylene backbone, Na-Nafion coating, and $NaClO_4$ in tetraglyme. Although the underlying mechanism was not discussed, experimental results showed reduced polysulfide permeation. With a thin layer of Na-Nafion between cathode and anode, the batteries exhibited fewer fluctuations in discharge capacity during the initial cycling and achieved a capacity of 350 mAh $g^{-1}$ after 20 cycles. The large charging voltage peak in CV caused by polysulfide shuttling also disappears in Na-Nafion-coated samples.

Yu and Manthiram further validated this shuttle-suppression property of the Na-Nafion membrane through a simple visual experiment.[153] **Figure 13**b shows the experiment setup, where they separately sealed polysulfide containers with Celgard separator and free-standing Na-Nafion membrane on the cap, and then immersed both containers into pure liquid electrolytes for several hours. It is obvious that the electrolyte in the Celgard container became brown-reddish because of fast polysulfide diffusion, while the electrolyte in the Na-Nafion container stayed colorless even after 5 hours. As presented in Figure 13a, micron-sized pores were evenly distributed on the commercial Celgard separator while Na-Nafion exhibits a flat, dense, and non-porous surface morphology. This special “micro-structure” helps the Na-Nafion membrane prevent polysulfide permeation.[154] The Nafion membrane contains a hydrophobic region as backbone and a hydrophilic region with ion-clusters as ion-transfer

channels, as shown in Figure 13c. The size of these hydrophilic regions is estimated to be around 4-5 nm, much larger than the $Na^+$ ion but on the same order as the size of polysulfides. Due to this "size effect", polysulfide species can barely diffuse through the hydrophilic pores, leading to efficient suppression of polysulfide crossover. Secondly, the $-SO_3^-$ group at the hydrophilic region offers a negatively charged environment, enabling positively charged $Na^+$ ions to transfer through freely. In contrast, the polysulfide ions are in the negative charge states, resulting in a strong "charge repulsion effect" which further suppresses polysulfide migration in Na-Nafion membranes. Figure 13c demonstrates the molecular structure of the polysulfide species and the charge repulsion process schematically. As a consequence, Na-S batteries with Nafion membranes exhibited a capacity of around 550 mAh $g_{(S)}^{-1}$ after 100 cycles.

Besides Na-Nafion, several other ion-selective-membranes were also tested in Na-S systems. Ren and coworkers fabricated polybenzimidazole (PBI) membrane as the separator for Na-S batteries.[155] It possesses both small pore sizes and functional groups that are able to bind polysulfide species. Similarly, Yu *et al*. synthesized a polymer with intrinsic nanoporosity (PIN).[80] Based on the molecular dynamics (MD) simulation, the PIN membrane has a dense and uniform surface morphology with a pore size of less than 1 nm, which also demonstrates good cycling performance in Na-S cells.[156]

Therefore, two key concepts in preventing polysulfide dissolution and migration can be summarized as: (1) incorporating an interlayer capable of strong interaction with polysulfide species, and (2) implementing a robust filter membrane able to selectively transport $Na^+$ ions, while excluding polysulfides. Regardless of the numerous types of interlayers or membranes however, polysulfide crossover cannot be completely avoided since these systems still require varying amounts of liquid electrolyte. In **Table 5**, we have summarized the cycling performance of Na-S batteries with various types of electrolytes discussed thus far. In most of these batteries, the cycle lives are limited to less than 100

cycles, which are far from levels required for practical applications. To further optimize their performance, the amount of the liquid electrolyte has been minimized to reduce polysulfide dissolution, but a proper membrane is still needed to cut off the polysulfide diffusion pathway.

*3.1.5. Solid-state electrolytes*

Solid-state Na-S research was initiated by Park and coworkers, when they first paired PEO with a S-cathode in 2007.[22] This battery comprised three solid components including a Na metal anode, the PEO/$NaCF_3SO_3$ polymer electrolyte (PE), and a S-cathode. At 90 °C, the PEO polymer electrolyte operates in the liquid phase to achieve a sufficiently high $Na^+$ ionic conductivity. A sharp capacity decay was observed during charging and discharging, implying that molten PEO allows for significant polysulfide migration similar to levels in liquid electrolyte. The discharge capacity drops from 505 mAh $g^{-1}$ to 166 mAh $g^{-1}$ in 10 cycles because of sulfur loss and polysulfide dissolution as they occur in liquid electrolytes and GPEs. While several studies using PEO-based composite PEs in Na-S batteries have been reported,[157-160] no significant breakthrough has been achieved due to its intrinsic affinity to polysulfide.

Over the past decade, Na-ion conductive ceramic materials have drawn extensive attention as a potential solid-state electrolyte (SSE) for Na-S batteries. It is worth mentioning that, as the commercialized solid-state ceramic electrolytes in high-temperature Na-S batteries, β”-alumina electrolytes have also been tested in room temperature systems.[161] This dense solid-state ceramic membrane is intrinsically impermeable to liquid electrolytes, completely cutting off the polysulfide diffusion. The battery structure is shown in **Figure 14**. The ceramic beta-alumina pellet is sandwiched between two pieces of glass fiber separators soaked with liquid electrolyte ($NaCF_3SO_3$ in 1:1 DOL/DME (*i.e.* 1,3-dioxolane/ dimethoxyethane) to improve the surface contact. With this liquid-solid electrolyte

combination, the charging process is largely stabilized with reasonable polysulfide inhibition results. Ahn and coworkers reported a discharge capacity of 855 mAh $g^{-1}$ for the first cycle and 521 mAh $g^{-1}$ after 104 cycles at r.t. with β"-alumina membranes.[162] They identified that the capacity loss was not caused by the shuttling effect. The discharge profile can be divided into two regions: the upper region from 2.30 V to 1.75 V represents the formation of soluble higher-ordered polysulfides ($Na_2S_n$, $4 \leq n \leq 8$), and the lower region from 1.75 V to 1.00 V corresponds to phase transformation and precipitation of lower-ordered polysulfides ($Na_2S_n$, $1 \leq n \leq 3$). With cycling, the discharge capacity of the upper region keeps consistent at 350 mAh $g^{-1}$ while the capacity of the lower region decays rapidly because of the precipitation of lower-ordered polysulfides.

Following the investigations on Li-ion superionic conductors such as $Li_{10}GeP_2S_{12}$, Na-ion glass-ceramic electrolytes with outstanding ionic conductivity have also been investigated.[163] As part of their distinctive crystal structure, the stable one-dimensional (1D) channels provide good ion pathways. Inspired by the high ionic conductivity and wide electrochemical window of Li-sulfide electrolytes, Hayashi and coworkers synthesized a $Na_3PS_4$ glass-ceramic electrolyte with superionic conductivity in 2012.[164] The electrolyte contains similar $Na^+$ ion diffusion channels and a high conductivity was demonstrated at $\sim 2\times10^{-4}$ S $cm^{-1}$ at r.t. From computational data, the $Na_3PS_4$ electrolyte is known to have two crystal phases including a tetragonal-phase and a cubic-phase that show similar ionic conductivities.[165, 166] In practice however, the authors found that cubic-phase $Na_3PS_4$ exhibited higher ionic conductivity. Nagata and Tanibata later incorporated this SSE into all-solid-state (ASS) r.t. Na-S batteries.[167, 168] In the ASS configuration, $Na_3PS_4$ powder is sandwiched between electrodes' powder and pressed at 200 to 360 MPa as a robust pellet. The full battery pellet structure is illustrated in **Figure 15**a. The upper layer of the pellet is the S-cathode while the SSE powder is condensed at the bottom of it. With this ASS design, they

reported a high reversible capacity of 1112 mAh $g^{-1}$ for the first cycle and the retained capacity greater than 1000 mAh $g^{-1}$ after 25 cycles.[169]

In Na-S batteries, the highest merit of using $Na_3PS_4$ and the ASS configuration is the complete removal of liquid and polymer electrolytes in which polysulfides are soluble. After getting rid of polysulfide dissolution and migration, the shuttling phenomenon diminishes and low Coulombic efficiencies no longer exist with cycling. However, employing $Na_3PS_4$ as a solid electrolyte for Na-S batteries introduces new problems into the system that can limit its application.

Firstly, $Na_3PS_4$ is not electrochemically stable when paired with Na metal anode as previously mentioned in Section 2.1.3.[77, 170] At the anode/electrolyte interface, $Na_3PS_4$ decomposes continuously after contacting Na metal, with $Na_2S$ and $Na_3P$ identified as decomposition products, leading to the formation of a poorly conducting SEI and an increasing cell resistance. Thus, rather than Na metal, Na-Sn alloy is highly favorable as the anode material here because of its high stability to $Na_3PS_4$. However, Na-Sn alloy anodes narrows down the potential window and therefore results in reduced energy density.

Secondly, it was observed that $Na_3PS_4$ could deliver an additional capacity above the theoretical cathode capacity during its cycling. In ASS cells with $Na_2S$ as the active cathode material, a capacity of 869 mAh $g^{-1}$ was reported by Yue and coworkers, which is larger than the theoretical capacity 687 mAh $g^{-1}$ of $Na_2S$.[23] To further investigate the origin of this additional capacity, $Na_3PS_4$ was employed as cathode material mixed with electronic conductive carbon. In the first charge, a slope above 2.0 V representing the oxidation of $S_2^-$ in $Na_3PS_4$ is observed; in the following discharge, a large plateau at 1.6 V and several small plateaus could be ascribed to the reduction of S and P in $Na_3PS_4$, respectively. These reactions provide 0.35 mAh capacity based on 2.5 mg $Na_3PS_4$ powder. Later, Fan and coworkers came up with an idea to take advantage of this extra capacity.[171] Figure 15b shows the charge/discharge profile of $Na_3PS_4$ as active cathode material and $Na_2S/Na_3PS_4$ composite

cathode made by the cast-annealing process in the first three cycles, separately. $Na_3PS_4$ alone provides around 0.3 mAh capacity while $Na_2S/Na_3PS_4$ composite exhibits a total capacity of 1.2 mAh. Thus, $Na_3PS_4$ accounts for an increase of about 25% of the total reversible capacity and boosts the battery performance to 650 mAh $g^{-1}$ after 50 cycles. In this case, Na-S batteries may benefit from the -additional capacity.

Thirdly, the glass-ceramic $Na_3PS_4$ electrolyte exhibits low ionic conductivity compared with liquid electrolytes and GPEs. Although better cell performance can be achieved by heating the battery slightly to 60℃, the conductivity remains undesirable for practical applications, and requires additional apparatus. Significant efforts have thus been made to improve the conductivity of the $Na_3PS_4$ electrolyte such as mechanical milling to break down the particle size or heating the electrolyte pellet over 270 ℃ to achieve better crystallinity.[75,166] Moreover, elemental doping is also believed to be an effective approach. Dopants including Se, Si, and halogens distort the unit cell structure and provide more vacancies, thus leading to faster $Na^+$ ion diffusion.[172, 173, 174]

Fourthly, manufacturing complexities largely hinder the development and commercialization of $Na_3PS_4$. High temperatures and pressures are mandatory in the fabrication of glass-ceramic electrolytes, meaning high energy input is required. Also, it lacks the flexibility for roll-to-roll processing techniques used in the battery fabrication industry today, making it hard to be implemented in mass production. Furthermore, $Na_3PS_4$ is chemically unstable in ambient air. If exposed to oxygen and moisture, $Na_3PS_4$ will hydrolyze to its oxy-compound with the evolution of $H_2S$, giving rise to more restrictions in battery assembly.[175]

Recently, a new type of glass-ceramic SSE material, $Na_3SbS_4$, which has high structural similarity with $Na_3PS_4$, has been investigated for its outstanding conductivity and stability during assembly and cycling.[176] The $Na_3SbS_4$ electrolyte can be prepared through common thermal treatment methods such as heating the stoichiometric mixture of $Na_2S$, $SbS_3$,

and sulfur powder at temperatures over 550 °C. Specifically, $Na_3SbS_4$ powder shows excellent solubility in MeOH or water, and is therefore feasible for solution-based processing or coating techniques, which could be used to improve the interfacial contact between electrodes and the electrolyte. Similar to $Na_3PS_4$, the crystallographic unit cell of $Na_3SbS_4$ consists of a body-centered tetragonal sublattice of $SbS_4^{3-}$ tetrahedra that form open 3D $Na^+$ ion diffusion channels, as shown in **Figure 16**a,b. Hence, these channels confer a high ionic conductivity of around 1.1 mS $cm^{-1}$ at 25 °C. Furthermore, Zhang *et al.* reported an ionic conductivity of 3 mS $cm^{-1}$ at r.t. if the electrolyte is synthesized by heating to 700 °C.[177] $Na_3SbS_4$ also benefits from its high stability: when directly exposed to ambient air, it shows good stability to both $O_2$ and $CO_2$, resulting in relatively stable chemical properties up to 48 hours of exposure before forming hydrated compounds, and could be fully recovered through simple thermal treatment. Therefore, unlike $Na_3PS_4$, $Na_3SbS_4$ does not pose manufacturing difficulties as the SSE for Na-S batteries. In addition, the above-discussed additional capacity issue associated with by $Na_3PS_4$ no longer exists, as Wan and coworkers have reported that the capacity contribution from the electrolyte is negligible within the typical operating window of 1.0 to 2.8 V.[178] As a result, Na-S batteries with $Na_3SbS_4$ electrolyte could deliver a capacity of 1386 mAh $g^{-1}$ at a current density of 50 mA $g^{-1}$ and stable high-rate cycling for 100 cycles at 1000 mA $g^{-1}$, as shown in Figure 16(c-d). Targeting the poor electrolyte/cathode interface, Ando and coworkers further designed a liquid-solid procedure to precipitate $Na_3SbS_4$ from its aqueous solution onto the cathode particles and then ball-milled the composite material to introduce a good surface contact between the electrolyte and cathode active material.[179] When a composite negative electrode composed of $Na_3SbS_4$ and $Na_3PS_4$ glass-ceramic was applied, a high capacity of 1560 mAh $g^{-1}$ was observed and a high capacity retention of 93% was reported after 50 cycles.

In conclusion, solid-state polymer electrolytes such as PEO are less effective in preventing the shuttling effect, while glass/ceramic electrolytes exhibit better cycling

performance and could completely eliminate the polysulfide dissolution in ASS Na-S batteries. Although $Na_3PS_4$ experiences several drawbacks, $Na_3SbS_4$ shows great potential as a promising alternative in the development of ASS Na-S batteries.

### 3.2. Solid-solid conversion reactions

In addition to the above approaches focused on the construction of physical barriers to prevent long-chain polysulfide dissolution and the resultant parasitic shuttle effect, an entirely different strategy is to eliminate the presence of long-chain sulfur species, which do not generate soluble polysulfides during battery operation. This can be achieved *via* fully solid-state conversion reactions that do not rely on bulk elemental sulfur as active material, but instead employ solid sulfur species, such as *chemically-bonded* sulfur bound to a composite, or insoluble *short-chain allotropes* (*e.g.* $S_2$ to $S_4$). In such a case, it is a requirement that all reaction intermediates formed during cycling also exist in the solid state and remain insoluble in the electrolyte solvent. Additionally, these composites must maintain good electrochemical reversibility, to avoid inadvertent formation of long-chain polysulfide intermediates ($Na_2S_x$, where $4 < x \leq 8$) arising from disproportionation side reactions. One unique property of such short-chain sulfur is their compatibility with carbonate-based electrolytes. Unlike their soluble long-chain counterparts that react irreversibly with alkyl carbonates, short-chain sulfur cycles well in carbonate electrolytes currently employed in Li-ion batteries.

In its bulk state, elemental sulfur exists as cyclo-octasulfur (*i.e.* $S_8$) in a cyclic crown-like conformation as the primary allotrope. Heated past its melting point, octasulfur undergoes ring opening at which point the $S_8$ sulfur chains become highly reactive, and can combine with other compounds present in the reaction mixture to form chemical bonds. Depending on the stoichiometric composition, the length of these sulfur chains varies, though it is preferable that chain lengths are limited to between 2 and 4 atoms. Also, the composite itself should be electrically conductive to allow for efficient electron transfer, and it is thus no coincidence

that many composites have conjugated structures. One such class of composites is termed sulfurized carbons, with sulfur chains bonded on the periphery of a graphitic carbon backbone. More recently, several groups have also explored new polymeric systems containing various forms of sulfur as the active species.

*3.2.1. Sulfurized carbons*

Sulfurized polyacrylonitrile (S-PAN) is an early example demonstrated with Na-S batteries. Nearly two decades ago in 2002, Wang and co-workers first reported that heating of the polyacrylonitrile (PAN) polymer in the presence of sulfur and an inert atmosphere produced a cathode capable of Li-ion storage.[180] While heating PAN itself above 300 °C leads to decomposition of its primary nitrile functionality, the added presence of sulfur has two effects.[181] Firstly, a portion of the sulfur acts as an oxidant and dehydrogenating agent during cyclization, undergoing reaction with the methylene groups to release $H_2S$ gas. Concurrently in the same process, reactive sulfur chains become embedded within the structure as short oligomeric chains (typically $S_{2-4}$), which exhibit high thermal stability above the normal boiling point of orthorhombic sulfur at *ca*. 445 °C. Typical S-content in the composites range from around 35 to 45 wt.%. The first reported use of S-PAN in a Na-S system followed in 2007, with Wang *et al*. attaining a short battery lifetime of 18 cycles with a specific capacity about 500 $mAh \cdot g^{-1}$, and employed an uncommon cathode architecture using porous nickel foam.[182] While not explicitly discussed at the time, we believe that the low sulfur utilization and cycle life could be the result of the composite exhibiting poor electronic conductivity or slow $Na^+$ diffusion rates.

Later attempts moved towards the electrospinning of S-PAN fibers as means to improve both cycle life and rate performance.[181,183] Instead of particulate PAN, Choi and co-workers carbonized electrospun PAN fibers together with sulfur (**Figure 17**b), resulting in a porous cathode. With a $NaClO_4$ electrolyte in EC/DEC, the authors indeed achieved better

sulfur utilization: 1158 mAh·$g_{(S)}^{-1}$ in the first discharge, with the nanofibers displaying better rate performance than its particulate counterpart, up to 6 C. Capacity retention was moderately high at 70% after 500 cycles at 1 C, with 153 mAh $g_{(\text{total composite})}^{-1}$ remaining compared to the initial 219 mAh $g_{(\text{total composite})}^{-1}$, and Coulombic efficiency maintained above 99.9%.[181]

Regardless of the S-PAN morphology, the general sodiation mechanism remains unchanged. Upon discharge, sodiation of the short sulfur chains occur, with $Na_2S$ formed as the final discharge product (Figure 17a). Recharging then results in the re-generation of sulfur species covalently bonded to the carbon backbone. Due to the nature of short-chain sulfur, the galvanostatic charge/discharge of S-PAN appears as a single sloping profile, unlike elemental sulfur which displays an irreversible high voltage plateau from long-chain polysulfides.[181] In spite of improvements in their electrochemistry, one drawback of electrospun cathodes is their incompatibility with conventional battery manufacturing practices employed in the Li-ion battery industry today, such as slurry-based preparations and roll-to-roll processing, posing a potential hurdle for large-scale production.

A second approach to enhance S-PAN performance is by altering the local chemical environment. From DFT computations, Seh and co-workers observed that $Na_2S$ and short-chain Na polysulfides generated from S-PAN interact strongly with polar binders.[184] Specifically, *carboxyl* groups in binders such as polyacrylic acid (PAA) were able to bind reaction intermediates more effectively compared to traditional PVDF (Figure 17c,d). Additional tests with natural carboxyl-containing binders (*e.g.* carboxymethyl cellulose (CMC), and Na-alginate) similarly achieved greater capacity retention and enhanced reaction kinetics. The PAA-based Na-S battery maintained a high specific capacity of 1000 mAh $g_{(S)}^{-1}$ with an exceptional lifetime of 1000 cycles in carbonate electrolyte, and Coulombic efficiency close to 100% throughout (Figure 17e). This is contrasted to the PVDF system with cathode pulverization and binder swelling observed.

More recently, alternative efforts to improve the kinetics of the S-PAN redox reaction and battery performance have turned towards *chemical doping* instead.[185-191] Chalcogens like selenium (Se) and tellurium (Te), or even iodine atoms have been incorporated into the composite to accelerate reaction kinetics. For example, although sulfur is electrically insulating at room temperature with a conductivity of approximately $5 \times 10^{-30}$ S $cm^{-1}$, elemental selenium is many orders of magnitude more conductive (in the order of $10^{-5}$ S $cm^{-1}$).[192] Thus, the overall composite conductivity increases with increasing Se/Te doping,[193] which is expected to improve the electrochemical performance. Yu and co-workers first employed a ball-milled mixture of Se and S powders for carbonization with electrospun PAN fibers, resulting in 6% Se-doping.[185] Thus, $S_{0.94}Se_{0.06}$@PCNFs (porous carbon nanofiber) electrodes demonstrated an improved initial sulfur utilization of 1375 mAh $g_{(S)}^{-1}$ at 0.1 A $g^{-1}$. Alternatively, commercial $SeS_2$ powder could be used in place of sulfur (**Figure 18**a,b),[186] with the total chalcogen (*i.e.* S and Se) content potentially reaching as high as 63 wt.% as achieved by Mitlin and co-workers.[188] Lou and co-workers demonstrated a clear enhancement in both sulfur utilization and capacity retention with Se-doping. At 0.1 A $g^{-1}$, the regular pPAN/S material gave an initial capacity of 1264 mAh $g^{-1}$, but decreased to 331 mAh $g^{-1}$ after 50 cycles. Under similar conditions, the pPAN/$SeS_2$ composite achieved a significantly improved 1530 mAh $g^{-1}$ and 835 mAh $g^{-1}$ in its first and final cycles, respectively (Figure 18b).[186] Longer term cycling at a higher current density of 1 A $g^{-1}$ gave an initial capacity of 1043 mAh $g^{-1}$ and maintained about 800 mAh $g^{-1}$ after 400 cycles.

One key advantage of the S-PAN sulfurized carbon family over other classes of S-based cathodes is their excellent compatibility with many common electrolyte systems. Xie and co-workers demonstrated their applicability in both carbonate- and ether-based electrolytes in 2019, and even in a $Na_3PS_4$ solid-state electrolyte, for both undoped and Se-doped S-PAN materials. The authors first reported their cyclability in a $NaClO_4$ PC/EC electrolyte, and also with NaTFSI/tetraglyme (containing 5% FEC). With the doped

$Se_{0.08}S_{0.92}$@pPAN, they observed a higher rate capability of 767 mAh $g^{-1}$ with the carbonate electrolyte versus 350 mAh $g^{-1}$ in ether, at 3 A $g^{-1}$.[187] Although possible reasons where not discussed, one may expect superior rate performance from the perchlorate/carbonate system due to their higher ionic conductivities. Long term cycling was also observed to be better in carbonates. With the Se-doped composite, a capacity of 770 mAh $g^{-1}$ was maintained up to 500 cycles at 0.4 A $g^{-1}$, compared to just 200 cycles in the ether. More recently, they further developed a full solid-state battery, utilizing Se-doped S-PAN together with a $Na_3PS_4$ solid electrolyte and an alloyed Na/Sn anode.[189] While the anode/electrolyte interface required an ionic liquid (*N*-butyl-*N*-methylpyrrolidinium bis(fluorosulfonyl)imide) to improve the interfacial contact, a good cathode/electrolyte interface could be obtained with standard cold-pressing and pelletization. Despite the low capacity and cycle life (372 mAh $g^{-1}$ at the final 50$^{th}$ cycle), this represents an important first step in establishing the suitability of S-PAN for solid-state r.t. Na-S batteries, serving as a foundation to build upon for future solid-state sulfurized carbon cathode systems.

In addition to Se, Te-doping has also been performed (at 4 mol%), similarly displaying excellent cycling in both carbonate and ether electrolytes.[190] At 0.1 A $g^{-1}$, a $Te_{0.04}S_{0.96}$@pPAN cathode gave high initial capacities of 1236 mAh $g^{-1}$ and 1111 mAh $g^{-1}$. Better rate performance for both $NaClO_4$-based EC/DMC/FEC and DOL/DME/FEC electrolytes were also noted compared to its Se-doped counterpart, respectively maintaining up to 629 mAh $g^{-1}$ and 601 mAh $g^{-1}$ at 6 A $g^{-1}$. The doped Na-S system was also able to deliver 970 mAh $g^{-1}$ over 600 cycles at 0.5 A $g^{-1}$ in carbonates, representing an impressively low decay rate of just 0.015%. Based on voltammetric analyses and UV-vis data, the authors also found that short-chain $S_3$ species underwent a two-step sodiation reaction pathway, first from sulfur to the short-chain $Na_2S_3$ polysulfide intermediate, then followed by $Na_2S$ as the final discharge product (Figure 18c,d). With their similar chalcogen chemistries, Te was also sodiated to give $Na_2Te$ in the fully discharged state. In ether solvent, Te-doping also

accelerated the conversion reaction, preventing the dissolution of polysulfide intermediates that would have resulted in capacity loss over time. In the case of iodine (I)-doping, it was proposed that iodination occurred only on the carbon backbone, without bonding to sulfur.[191] They also did not contribute to reversible battery capacity, after forming a C-Na-I bond during the first discharge cycle (Figure 18e). The resulting I-S@pPAN electrode exhibited an initial capacity of 994 mAh $g^{-1}$ at 0.5C, retaining 768 mAh $g^{-1}$ after 500 cycles, with the authors noting faster $Na^+$ ion diffusion as seen from GITT data.

Overall, improvements in cycling performance due to elemental doping are primarily attributed to improved electronic conductivities. For example, doping an S-PAN composite with 5% selenium was seen to almost double its electronic conductivity from $3.5 \times 10^{-9}$ S $cm^{-1}$ to $6.7 \times 10^{-9}$ S $cm^{-1}$,[188,194] similar to I-doping at 2wt.%, from $3.07 \times 10^{-10}$ S $cm^{-1}$ to $5.90 \times 10^{-10}$ S $cm^{-1}$,[191] compared to Te-doping at 4% (for $Te_{0.04}S_{0.96}$@pPAN) increasing its electronic conductivity by 1.65 times.[190]

As such, current evidence of the effects of doping on electrical conductivity remain fairly anecdotal, and it would be very useful for the battery community to have more comprehensive evidence of how the conductivity varies with the *doping extent*, either containing *different* elements (*e.g.* within the chalcogen/halogen groups), or at least a measure of an optimal doping range. Despite their benefits, such doping with heavy elements (*e.g.* Se, Te, I) introduces yet another issue as their added weight reduces the overall *energy density* of the cell. In further consideration of the previously discussed compatibility issues between cathode morphology and conventional battery manufacturing practices, an *un-doped* sulfur composite of *particulate* morphology would therefore be advantageous towards practical application of Na-S batteries.

### *3.2.2. Sulfur-copolymers from bulk elemental sulfur*

We further explore other covalent-sulfur systems, in the form of S-copolymer composites. In 2013, Pyun and co-workers were first to develop a high-S-content rubber-like polymer for Li-S battery cathodes, based on the *inverse vulcanization* process of sulfur;[195,196] *vulcanization* being the process of adding small amounts of sulfur for cross-linking of diene-based polymers such as for the vulcanization of rubber tires, but which is instead *inverted* in the described process with excess sulfur crosslinked by dienes, specifically 1,3-diisopropenylbenzene (DIB). We note that while the S-content could be tuned by varying the S:DIB ratio, it mostly existed as long-chain species up to $S_8$. Interestingly, we have not seen the application of DIB-crosslinked sulfur in Na-S systems as yet, which again leads one to speculate on the low compatibility of long-chain S-cathodes in liquid electrolyte Na-S batteries.

With Na-S batteries, Ghosh *et al*. first performed the ring-opening polymerization of $S_8$ in the presence of cardanol-based benzoxazine, obtained as a lipid from the commercial processing of cashew nuts.[197] As illustrated in **Figure 19**a, the CS90 composite contained several potential reactive sites towards sulfur, including oxazine ring sites and benzylic carbons, but also the *diene* functionality central as a cross-linker in vulcanization processes. At this point however, it is important to emphasize two important aspects in the presented system: *(1)* a *lack* of conjugated structures in the carbon backbone to confer electronic conductivity, and *(2)* a large variation in the sulfur chain length. The former could be easily addressed with the addition of reduced-graphene sheets to improve the conductivity (Figure 19b), but the different sulfur species would have major ramifications on the battery properties, such as electrolyte compatibility. Indeed, an ether-based electrolyte ($NaClO_4$ in tetraglyme, containing $NaNO_3$) was required to accommodate cycling of long-chain sulfur species; carbonate electrolytes would have otherwise reacted irreversibly with these long-chain intermediates. As a result, a capacity of just 285 mAh $g^{-1}$ was observed for the CS90−reduced graphene composite, after only 100 cycles. In this regard, we believe that using the co-polymerization approach to tune the S-content could arguably act as a double-edged sword.

On the one hand, a major advantage is the ability to maximize the S-loading (*e.g.* up to ~89 wt.% sulfur in the present case) to attain high cellular energy densities. The difficulty lies however in limiting the precise sulfur-chain lengths to just short-chain species. Any long-chain sulfur present would produce soluble polysulfide intermediates, resulting in loss of active material and fast capacity decay.

Following this example, Armand and co-workers further developed a S-copolymer cathode the subsequent year, using $S_8$ and poly(S-pentaerythritol tetraacrylate) (PETEA) prepared *via* an analogous inverse vulcanization-like process.[151] Through the cross-linking of sulfur chains and PETEA (Figure 19c), the S-copolymer cathode could reach an impressive S-content of 97 wt%. As discussed in Section 3.1.3., the gel polymer electrolyte could be further used to mitigate against polysulfide dissolution and shuttling. Used in combination, the poly(S-PETEA) cathode and gel polymer electrolyte were able to deliver high specific capacities of 877 mAh $g^{-1}$ and 372 mAh $g^{-1}$ at 0.1 C and 2 C respectively, and retained 736 mAh $g^{-1}$ after 100 cycles. The corresponding energy density was also reasonably high at approximately 956 Wh $kg^{-1}$ (based on the sulfur mass only), and a mid-voltage of around 1.3 V. More importantly, the study also presented a fundamental understanding of the polysulfide-trapping abilities of the two polymers used.[151]

*3.2.3. "Bottom-up" sulfur-composite synthesis from small organosulfur molecules*

Compared to the use of elemental $S_8$ as a precursor for "top-down" synthesis (*i.e.*, breaking down of long polymeric sulfur chains for incorporation into a composite), we consider the "bottom-up" approach a more accessible method to build S-containing composites from small organosulfur molecules. Unlike the above instances which conferred little control over sulfur chain lengths, the use of specific molecules allows for better precision in this aspect, giving composites that have more ordered structures and electrochemically active sulfur moieties.

The following examples include thio-compounds such as thiophene, benzenedisulfonic acid, sulfate salts, and carbon disulfide.

In 2019, Chen *et al*. described the incorporation of S-atoms into a carbon structure *via* thioether bond formation (**Figure 20**a).[198] The first step of the synthetic procedure was based on classical Friedel–Crafts polymerization mechanisms using thiophene as the monomer and S-precursor, while dimethoxymethane served as the cross-linker. The obtained polymer was then carbonized at 600 °C under inert gas. As such, the authors reported the formation of only insoluble thioether species, and consequently the near-complete elimination of the polysulfide shuttle effect. The short-chain thioether moiety could thus be cycled in a standard carbonate electrolyte ($NaClO_4$ in PC/FEC), as the discharge products ($Na_2S_2$ and $Na_2S$) were also insoluble and remain confined within carbon defects. As a result, a reversible capacity of 500 mA h $g^{-1}$ was obtained over 100 cycles, at 100 mA $g^{-1}$. They also noted the importance of an electrochemical *activation* process, done by initial cycling within a low voltage region of 0.01–0.50 V *vs*. $Na/Na^+$, attributed to the scission of the thioether bond. After this activation, long-term cycling of 800 cycles could be achieved, with 330 mA h $g^{-1}$ remaining in the final cycle. One significant drawback however, was the low S-content at 21.5 wt.%, which could be somewhat expected given the single-atom thioether moiety.

As an effective answer towards the typical lack of control over the type of sulfur species and low overall S-content, Ji and co-workers showed that the sulfur chain-length could, in fact, be controlled by careful choice of thio-monomer precursors.[199] Summarized in Figure 20b, the calcination of benzenesulfonic acid (BSA, $C_6H_6O_3S$) in the presence of KCl salt at 600 °C in inert atmosphere produces a minimal amount of short-chain sulfur species bonded to a graphitic carbon backbone structure, with a sulfur weight-content at 8.53%. Replacing BSA with *di*-substituted benzenedisulfonic acid (BDSA) increased the S-content to 18.33%. However, further replacement of just the salt template to potassium sulfate ($K_2SO_4$) greatly boosted the S-content to 40.07 wt.% for the SC-BDSA composite, similar to levels in

sulfurized carbon materials. Most of the sulfur existed as O-S and C-S bridges, and the salt template also affected the composite morphology, with both the KCl-based C-BSA and C-BDSA composites having a three-dimensional coral-like appearance while SC-BDSA displayed flaked structures. Containing a majority of short-chain sulfur species insoluble in carbonates, the composite performed well in a EC/PC-based electrolyte. Similar to the thioether-based composite by Chen *et al.*, SC-BDSA was observed to perform better after electrochemical activation below 0.6 V *vs*. $Na/Na^+$, attributed to the cleavage of $C\text{-}S_x\text{-}C$ bridges which contributed an additional capacity. Thus, the SC-BDSA composite could attain an impressive 1000 cycles at 2.5 A $g^{-1}$, ending with a specific capacity of 696 mAh $g^{-1}$.

Another example of the "bottom-up" synthetic approach employed an unconventional but interesting combination of carbon disulfide ($CS_2$) and red phosphorus, prepared *in situ* by a high pressure solvothermal method, exploiting the strong interaction between the two materials (Figure 20c).[200] The use of $CS_2$ as S-precursor is fairly unusual due to its high volatility (boiling point: 46 °C) and also its associated toxicity. In this case however, the solvothermal vessel allowed for the high pressure and temperature necessary for $CS_2$ to exist as a supercritical fluid. Strong interactions between phosphorus and sulfur were described to have resulted in the rapid combination of red phosphorus with the sulfur atoms in $CS_2$ to form phosphorus sulfides, in the form of −P−S−C−S−P− bonds. The bridging phosphorus sulfide is then proposed in turn to escape under the high temperatures between 300 °C to 400 °C, leading to combination of neighboring S-C species and the eventual construction of a sulfur−carbon covalent structure. The resulting covalent-SC presented a sheet-like structure with interlayer separation of 0.389 nm, similar to graphite (0.34 nm), and a S-content of about 38 wt.% based on thermogravimetric analysis. In a $NaClO_4$ EC/DEC/FEC electrolyte, the authors found that electrochemical activation was again required (Figure 20d), between 0.01−3 V, akin to the earlier sulfur-carbon composites prepared based on the "bottom-up" synthetic approach. Sulfur in the interior of the sheets were first seen to be activated by $Na^+$

ion intercalation below 0.5 V, which then contributed to capacity in the subsequent cycles between 0.5−3 V. The activation was also noted to enlarge the interlayer spacing between carbon sheets to about 0.4 nm during the first cycle, and some pseudocapacitive behavior was also observed from $Na^+$ ion intercalation. Moreover, the interlayer spacing was also sufficient to accommodate the formation of $Na_2S$ as the discharge product. After activation, the composite delivered a significant 811.4 mAh $g^{-1}$ after up to 950 cycles at 1.6 C, from an initial 1063.7 mAh $g^{-1}$. The overall sodiation mechanism is also analogous to that of sulfurized carbons with $Na_2S_x$ (x = 1−4) reported to evolve in the discharge state, where such short-chain polysulfide intermediates remain insoluble and unreactive in the carbonate-based electrolyte.

Most recently, a Zn-based MOF structure was constructed for Na-S battery cathodes, using both 2,5-thiophenedicarboxylic acid and 1,4-bis(pyrid-4-yl) benzene as the organic ligands.[201] Its uniqueness lies in the ability to *co*-dope both sulfur (from thiophene) and nitrogen (from pyridine) into the structure. Although elemental sulfur was also introduced subsequently *via* vapor infiltration, the covalently-bonded sulfur and nitrogen functionalities provided strong entrapment of $Na_2S$ and short-chain polysulfides as they form during cycling. The resulting morphology exhibited large sheet-like structures, and when further wrapped with a polydopamine coating, could reach a maximum S-content of 37 wt.%. As such, a high initial charge capacity of 461 mAh $g_{composite}^{-1}$ (1246 mAh $g_{(S)}^{-1}$) could be obtained in a PC/FEC electrolyte, with a reasonable retained capacity of 270 mAh $g_{composite}^{-1}$ (730 mAh $g_{(S)}^{-1}$) after 1000 cycles at a current density of 1.0 A $g^{-1}$.

Hence, such recent progress in the synthesis of new sulfur-carbon composites from organosulfur molecules presents an exciting future for Na-S battery cathodes. Nevertheless, in the pursuit of alternative sulfur active materials, several key considerations should still be noted. Firstly, the choice of the S-based monomers/building blocks will greatly influence the *(1)* type of sulfur and *(2)* the length of the resulting sulfur chains, of which short-chain sulfur

species are still preferred to prevent any long-chain polysulfide dissolution or the shuttle effect. Furthermore, short-chain species undergo *solid-solid* sodiation reactions during cycling, exhibiting compatibility with common carbonate solvents with typically higher ionic conductivities and electrochemical stability in widespread use today with Li-ion batteries, as compared to ether-based electrolytes. Nevertheless, careful control of the S-precursor ratios with other reactants needs to be taken to *(3)* maximize the low sulfur contents generally associated with this approach. Certainly, it would be interesting to watch the development of other thio-based molecules being employed to form new composite structures in the near future.

*3.2.4. Microporous hosts for short-chain sulfur molecules*

Another broad approach to create such small sulfur allotropes is through *physical* encapsulation. Under room temperature and pressure, the main $S_8$ allotrope has a ring diameter of 0.69 nm.[11,202] Thus in 2012, Xin *et al*. first proposed that since short-chain allotropes ($S_{2–4}$) have at least one dimension less than 0.5 nm, while longer cyclo-sulfur species have at least two dimensions above 0.5 nm, one could technically force sulfur into micropores smaller than 0.5 nm across, and in so doing generate short chains containing no more than four S-atoms.[203] In this section, several methods are described herein to encapsulate sulfur within microporous carbon structures as short-chain molecules. Another recent study explores an intrinsically microporous polymer that combines *both* physical confinement and chemical bonding strategies to prevent polysulfide dissolution.

In light of the discussed confinement of sulfur within structures with micropores < 0.5 nm in diameter, several such composites have been demonstrated with Na-S batteries. These mainly include MOFs such as the zeolitic imidazolate framework (ZIF),[11,13,89,105] although common table sugar and polymeric structures can also be used as microporous templates. In addition to the repurposing of a glucose-derived microporous sulfur composite for the Na-S

battery by Xin *et al*.,[13] two other groups led by Archer[11] and Zhu[204] also developed microporous carbon-sulfur composites as Na-S battery cathodes in 2016. The preparation procedure is a three-step process. This begins from the synthesis of ZIF-8 crystals from zinc nitrate and 2-methylimidazole, followed by carbonization in inert atmosphere between 800 °C to 1000 °C (**Figure 21**a), resulting in highly ordered dodecahedron nanoparticles (Figure 21b). Since ZIF-8 contains tetrahedrally-coordinated zinc ions, it was noted that the carbonization temperature affected the final zinc content (boiling point at 907 °C), and could require additional acid washing to remove residual metal. Finally, the third step involved the melt-diffusion of sulfur into the micropore system, with the maximum S-content reaching up to *ca*. 50 wt.%.[204]

Zhu and co-workers demonstrated Na-S battery cycling in tetraglyme electrolyte, and obtained an initial specific capacity of 873 mAh $g^{-1}$ at 0.2 C, with the cell retaining around 500 mAh $g^{-1}$ after 250 cycles.[204] The rate performance however, decreased fairly quickly from 1000 mAh $g^{-1}$ at 0.1 C to 220 mAh $g^{-1}$ at 2 C, which we believe to arise from its high viscosity at r.t. A carbonate system was further investigated in the case of Archer and co-workers, using a $NaClO_4$-based EC/PC electrolyte, containing $SiO_2$–tethered ionic liquid–$ClO_4$ additives to stabilize the anode interface.[11] Using real-time mass spectroscopy (DART-MS) and a negative ion source, the authors found $S_3$ to be the dominant species present, although $S_8$ chains could also be observed when a positive ion source was used. Nevertheless, they reported that only insoluble $S_2^{2-}$ or $S^{2-}$ species were formed in the carbonate system. Also from GITT analysis, the equilibrium potential of each titration step fell below 2 V *vs*. $Na/Na^+$, suggesting the generation of short-chain $Na_2S_x$ (where $x \leq 2$). Hence, an initial capacity of 866 mAh $g^{-1}$ was obtained at 0.5 C, and could sustain up to 600 mAh $g^{-1}$ at the final 100$^{th}$ cycle.

Microporous carbons can also be constructed by exploiting the structure of common polymers such as PVDF,[205] attaining both a narrow distribution of pore sizes (around 0.55

nm) and also a reasonably high pore volume (0.41 $cm^3 g^{-1}$) to realize high storage capacities. After sulfur infiltration, Hu *et al*. reported a S-content of 39.72 wt.%. Cycling in an EC/DEC electrolyte achieved an initial capacity of 918.4 mAh $g^{-1}$ at 0.1 C, and retained 392 mAh $g^{-1}$ after 200 cycles at 1 C, with Coulombic efficiency maintained close to 100% throughout.

In our pursuit of suitable microporous host structures, one should also keep in mind that raw material costs constitute an important consideration for any future commercial development of Na-S battery technologies. In this regard, Pint and colleagues put forth a low-cost option to derive a microporous carbon host using standard table sugar.[206] The straightforward, albeit highly exothermic, process first involved the reaction between sucrose and concentration sulfuric acid, followed by pyrolyzing the collected amorphous carbon at 850 °C in argon gas to form the microporous structure (Figure 21c). Finally, regular melt infiltration of sulfur would be done to infuse short-chain sulfur into the pores. The spherical product ranged in diameter from around 50 nm to 500 nm, and more importantly consisted of micropores roughly 0.5 nm in size, allowing sulfur to exist mainly as $S_{3-4}$ chains within the pore structure (Figure 21c). Using the $NaPF_6$ electrolyte in tetraglyme with $NaNO_3$, the authors observed a two-step sodiation/desodiation mechanism from cyclic voltammetry; short-chain sulfur is first reduced to short-chain polysulfide intermediates such as $Na_2S_2$ at *ca*. 1.7 V, followed by formation of $Na_2S$ as the final discharge product at ~0.9 V (Figure 21d). Despite the ether-based solvent employed, the mechanism still proceeded *via* a solid-solid phase reaction due to effective sulfur confinement, with the pore diameter of approximately 0.7 nm being too narrow to accommodate solvent molecules. The first discharge cycle attained approximately 1520 mAh $g^{-1}$ at 0.1 C, close to the theoretical capacity of sulfur, with moderate rate capability of 370 mAh $g^{-1}$ at a higher rate of 1 C (Figure 21e). Long term stability was also noted, with 306 mAh $g^{-1}$ retained after 1500 cycles.

*3.2.5. Combining micropore confinement with covalent sulfur-bonding*

Besides the purely physical method of short-chain sulfur encapsulation, a *two-pronged* approach could also be accessed by simultaneously exploiting both physical encapsulation *and* chemical bonding methods. Unlike the synthetic methodologies of the earlier examples where sulfur was infused into microporous hosts only *after* their carbonization step, the main difference herein lies in the concurrent carbonization of the host structure together with the formation of covalent sulfur species in a *single* heating step. As such, an intrinsically microporous precursor must first be chosen such that its distinctive pore structure can be translated into the composite intact. Conjugated microporous polymers (CMPs) are one such possible class of precursors with all the advantageous attributes such as a π-conjugated system for electrical conductivity, heteroatoms for doping and covalent bond formation, and an inherently ordered pore structure.[207,208] We should *emphasize* nevertheless that the use of a microporous precursor does *not* necessarily imply that the product will adopt the same pore configuration, since the added presence of sulfur and/or the carbonization process could dramatically influence the resultant pore morphology.

Several attempts at the construction of covalent sulfur composites with micropores have largely focused on cyclic anhydride monomers, such as 1,2,4,5-benzenetetracarboxylic anhydride (or pyromellitic dianhydride, PDA)[209] and 3,4,9,10-perylenetetracarboxylic dianhydride (PTCDA).[210] Typical syntheses would call for the physical mixing of the precursor with elemental sulfur or S-compounds followed by carbonization under inert atmosphere. Reasonable battery performances could be achieved with good cycle lives of 1000 cycles (297 mAh $g^{-1}$) with the PDA-based composite,[209] or up to 400 mAh $g^{-1}$ after 150 cycles at 150 mA $g^{-1}$.[210] While there was clear evidence for the existence of covalent sulfur species, the final composites may not have had well-defined micropores for physical confinement of short-chain sulfur.

In the latest example, Jeon *et al*. designed a Na-S battery cathode based on a polymer of intrinsic microporosity, or PIM-1 (**Figure 22**a).[211] The microporous polymer was first

synthesized from its constituent monomers, followed by its carbonization in the presence of sulfur, resulting in short-chain sulfur ($S_{2-4}$) being trapped within its pores (Figure 22b,c). The high carbonization temperature of 600 °C was also said to remove any physically confined but chemically unbound sulfur species, with TOF-SIMS confirming the presence of covalently-bound sulfur fragments (Figure 22d), and the final S-content around 30 wt.%. Based on adsorption/desorption isotherm analysis with argon gas, the composite without loaded sulfur also exhibited a type I isotherm characteristic of micropores, and a narrow pore size distribution mainly around 0.5 nm (Figure 22e,f). Using a common perchlorate electrolyte in EC/PC/FEC, voltammetry of the composite showed a two-phase conversion of $Na_2S_4$ to $Na_2S_2$, then to $Na_2S$. Na-S batteries based on the PIM-1 sulfur cathode could exhibit a reversible capacity of *ca*. 550 mAh $g^{-1}$ up to 250 cycles, without any occurrence of the shuttle effect.

The uniqueness of the combined micropore confinement and chemical bonding approaches is expected to pose a challenge for accurate determination of the micropore distribution, since the pores themselves are likely to be already occupied (containing short-chain sulfur). Therefore, it is imperative for any claim of a microporous composite to be accompanied by a suitable analytical method detailing the pore distribution in the micropore regime (defined as <2 nm in diameter).[212] Instead of the common $N_2$ gas employed for adsorption/desorption analysis at 77K, other adsorptive gas/temperature combinations are necessary; either with argon gas at 87 K, or $CO_2$ at 273 K maintained with an ice bath. Furthermore, appropriate models should be used to approximate the micropore filling mechanism, usually available within the software supplied with the instrument, such as the Horvath-Kawazoe (HK) method,[213] or the non-local density function theory (NLDFT) pore-filling model for application over the full micropore and mesopore range,[214] but neither the Brunauer-Emmett-Teller (BET) analysis nor the Barrett-Joyner-Halenda (BJH) method which are applicable for mesopore (2-50 nm) surface areas and pore volumes/sizes, respectively.

As summarized in **Table 6**, innovations in the synthesis of insoluble short-chain sulfur composites, host structures, and sulfur co-polymers have greatly advanced the state-of-the-art. With the recent progress achieved in terms of cell metrics such as cycle life and sulfur utilization, the community should now turn our focus towards development of high energy and power devices for practical applications, as we explore in next Section.

## 4. Prospects and future outlook: sodium-sulfur batteries and beyond

### 4.1. Sodium anode and electrolyte development

The Na metal anode is both technologically and scientifically important, but there is a dearth of fundamental understanding of the SEI growth, structure, and origin of Na dendrites, which hamper its adoption for practical applications. The SEI, typically assumed to remain chemically and mechanically stable during electrochemical operations, is in fact extremely sensitive towards factors such as the solvent-salt system, nature of electrolyte additives, and electrode surface engineering. Moreover, Na dendrite growth is generally presumed as non-uniform Na plating on the metal surface, despite its exact origins not yet well understood. Without complete understanding of the fundamental reasons behind Na dendrite growth and SEI formation, safe and stable operation of Na metal batteries remain elusive. Here, we put forth fundamental and applied strategies to realize stable and safe operation of high energy density Na metal batteries.

#### *4.1.1. Micro-engineering electrolyte formulations*

Ionic conductivity and homogeneity are the two most essential components of an electrolyte formulation to ensure uniformity of the electric field, which is desirable for efficient and reversible electrodeposition. Nearly all liquid electrolyte research on Na metal batteries include diluted as well as concentrated electrolytes, so that a reversible and uniform Na deposition could be achieved. Due to inherent limitations of both salt and solvent, there is a

maximum current density or voltage that can be sustained by these electrolytes without negatively impacting electrochemical reversibility and Na deposition morphologies. Therefore, it is important to understand the possible causes behind these limitations, and to design novel electrolyte formulations for high rate and long-life batteries. Electrolyte additives have been promising thus far in achieving reversible Na deposition morphology. However, the majority of these carry a cation whose reduction potential is moderately positive with respect to Na metal. Despite aggressive theoretical and experimental investigations, more studies are still needed to insight the effect of the additives' reduction potential on Na anode stability. Electrolyte additives with highly reductive potentials afford opportunities for handling high current densities yet preserving Na deposition morphology, and strengthening the SEI.

The ionic interphase between Na metal anode and solid electrolytes have also become a bottleneck in designing high performance solid electrolytes. Solid electrolytes that comprise both highly conductive inorganic centers and soft polymer backbone could be a potential alternative to that of liquid electrolytes. The solid electrolyte can be designed using lamellar 1D or 2D inorganic materials, and polymer chains could serve as anchoring sites as well as the host for inorganic materials. Such a combination is expected to provide not only high mechanical strength and efficient $Na^+$ ion transport due highly ordered inorganic component, but also improved flexibility. Micro-engineering the ionic interface between Na metal and solid electrolytes is crucial to ensure adhesion and minimize interfacial resistance. A quasi-fluidic or viscoelastic solid electrolyte could be useful to accommodate local fluctuation at Na metal anode.

### *4.1.2. Characterization tools to study SEI and sodium dendrites*

In recent years, great progress has been made in developing and applying advanced characterization tools to understand morphological and structural aspects of Na dendrites. For example, morphological and chemical information of Na dendrites can be obtained using cryo-TEM and cryo-STEM. However, fundamental understanding of nucleation, growth, and electrochemical reactivity could not be established by any *single* characterization tool. It is therefore clear that any existing characterization tool is inadequate in obtaining deep and comprehensive information about the SEI and Na dendrites. We believe, however, that *combining* different characterization tools is an important direction to explore. To provide multi-dimensional, multimodal information about electrode chemistry, *in situ/in-operando* techniques previously developed to study Li battery interfacial chemistry can be extended to investigate Na metal interfacial chemistry. In addition, scanning droplet microscopy (SDM), which is a surface sensitive tool, can be used in combination with Raman spectroscopy to examine morphological evolution as well as electrochemical reactivity along with chemical properties of the SEI and Na dendrites.

Besides experimental evaluation, theoretical predictions using tools such as DFT or molecular dynamics simulations, and multi-scale modeling are equally important to understand the phenomenology of the SEI.[215,216] Owing to the complex structure of the SEI, it is immensely challenging to establish a comprehensive structure-property relationship. However, modeling methods coordinated with experiments may open a new dimension to make qualitative and quantitative predictions about the multi-component and multi-structured nature of the SEI. For example, Bhowmik *et al*. unveiled new strategies through integration of multi-scale modeling and experiments to understand and track different types of uncertainties in the experimental and simulation methods, and guided to improve the design of battery interfaces and interphases.[217] Moreover, the outlined possible strategy could also be applied to monitor the physical and chemical changes that occur upon addition of additives or other SEI repairing agents. For the development of future ultra-high performance battery

technologies, such innovative routes present distinctly interesting opportunities that are yet to be explored.

*4.1.3. SEI and surface engineering*

Despite structural and chemical evaluation of the SEI, precise control on SEI formation has not yet been achieved, likely due to the softness and irregularity of Na metal surfaces. Designing an ultra-smooth surface could be a possible route to understand the formation of SEI and dendrite growth, despite extreme difficulties in obtaining atomically flat Na surfaces. Recent research attempts have been made to tackle this issue, and research should continue in this direction to further understand the nucleation and growth of the SEI and Na dendrites.

SEI modification techniques, like electrolyte additive and artificial interphase design, have proven their vast potential in repairing the SEI and suppressing dendrite growth, and research should continue in this direction. The *methodologies* however, need to be improved, as existing techniques require metal anodes to be in direct contact with the precursor. Designing artificial interphases without compromising the integrity of the Na metal surface is of immense interest. Recent research on the solid-vapor approach (as a fully contact-free method), allows the development of high-quality artificial interphases, and we believe that research efforts in this direction may lead to us to attain ultra-stable Na metal anodes. This solid-vapor approach must not be limited to volatile liquid precursors, but more complex organic or inorganic compounds should also be explored. In addition to inorganic coatings that exhibit high ductility and stiffness, self-assembled monolayers or polymers should also be investigated, and it is imperative that their compatibility with the Na anode also be examined. Moreover, lamination of pre-fabricated self-healing layers using highly controlled techniques, such as Langmuir-Blodgett may also be explored, which not only increases the SEI functionality, but also scalability for mass production. At present, the majority of intrinsic and extrinsic interphases are based on a single inorganic or organic component limited to only one

desirable property, such as high stiffness, ductility, or ionic conductivity. Instead, designing a multi-layer interphase that exhibits both high mechanical strength and ionic conductivity is certainly desirable.

The issue of infinite volume change is also crucial in metal anode batteries, and a strategy to circumvent this is to use a host material with high affinity toward Na. Sodiophilic surfaces exhibiting high chemical, mechanical and electrochemical stability have recently been explored. However, the Na loading remains low and is also typically distributed randomly across host sites, which is a probable cause of poor Na anode stability. In these circumstances, it is necessary to design and develop a universal surface functionalization method that can accommodate Na through sodiophilic sites, and minimizes its distribution at the same time. We believe that combining this sodiophilicity aspect and the solid-vapor approach could be a novel route to realize high Na loading and uniform Na distribution across the electrode.

### 4.2. Prospective sulfur cathodes

#### *4.2.1 Covalent composites*

In our continued search for Na-S-compatible cathodes, two fundamental challenges of *low electrical conductivity* of sulfur and capacity fading from *polysulfide dissolution* remain of paramount importance. Arguably, strategies to address the former issue are more straightforward, such as the myriad examples of conductive conjugated carbon composites discussed above. A higher content of conductive additives (*e.g.* carbon black) could also be used in the electrode mixture. Yet another alternative is the addition of electrochemically active and conductive elements such as selenium,[192,218,219] which take part in the sodiation reaction and contribute to charge storage, unlike electrochemically inactive carbon. While these approaches are undoubtedly effective in improving sulfur utilization, the added weight introduces a practical dilemma by reducing gravimetric capacity and energy density.

Low gravimetric capacities are thus a major consideration in the choice of appropriate covalent-sulfur composites for Na-S battery systems. Unlike Li-S batteries where elemental sulfur can be cycled stably in ether electrolytes with high S-loads of up to 70-80 wt.%, soluble Na polysulfide intermediates produced in the Na-S system are too reactive with the Na anode to be cycled reversibly, should effective confinement measures not be in place. Furthermore in the case of carbonate solvents, such long-chain polysulfides react irreversibly with alkyl carbonates. This leads to the strong need to prevent direct physical contact of long-chain polysulfides with the electrolyte regardless of solvent type, as seen from numerous strategies above. Regardless of the confinement method employed, the average S-content is severely impacted, ranging between 20-40 wt.% in covalent-sulfur composites and microporous structures, to a maximum of around 40-60 wt.% with mesoporous carbon hosts. Hence, it is imperative that we turn our focus towards novel systems which contribute as little "dead weight", without compromising either electrical conductivity or polysulfide confinement properties.

*4.2.2 Host structures*

Given the typically low S-contents limited by short-chain sulfur species in microporous composites, higher pore volume mesoporous hosts with strong polysulfide binding and/or catalytic activities could be selected to maximize the S-content and gravimetric capacity. Indeed as seen in the earlier sections, several recent works have opted to focus on electrocatalysts in mesoporous host materials, which act by reducing the overall time that soluble polysulfides reside in solution. Also, new advances have been made in our understanding of polysulfide confinement using *polar* host materials in Li-S batteries, from which parallels can be drawn to Na-S batteries. Representing a paradigm shift, Amine, Yu, and colleagues demonstrated the importance of *surface polarity* over *conductivity* as the dominant factor for an ideal sulfur-host.[220] In their latest study, two mesoporous hosts with

similar pore structures were contrasted: non-conductive but highly polar mesoporous silica *versus* highly conductive but non-polar mesoporous carbon. Despite higher initial capacity (*i.e.* sulfur utilization) of the carbon host as one would expect from its better conductivity, polar mesoporous silica exhibited better polysulfide confinement with 54% capacity retention after 2000 cycles, compared to only 15% in non-polar mesoporous carbon, with Coulombic efficiencies of 96 and 83%, respectively. Most importantly, a high S-content could be attained at 80 wt.%. In summary, polysulfide dissolution should be prioritized as the more critical issue, while electronic conductivity can be simply compensated for using conventional additives. In light of these findings, we could also speculate that for existing polar host materials such as N,O,S–doped carbons demonstrated in Na-S batteries,[11,13,139-141,143,201,204] extensive doping could potentially improve sulfur-trapping and battery cycle life further, regardless that it comes at the expense of electronic conductivity.

It can thus be seen from the above discussion that designing effective sulfur hosts requires an in-depth understanding of reaction mechanisms and inherent properties of host structures. Rational development should be viewed as an *iterative process* between theory-guided design, empirical testing, followed by mechanistic validation in a positive feedback loop. For instance, DFT calculations are first performed for materials with potential polysulfide confinement and/or catalytic properties.[221-223] Electrochemical tests are then carried out, with the reaction mechanisms probed *in operando* using techniques such as *in situ* Raman spectroscopy and synchrotron X-ray diffraction (XRD).[134,141,142,224] The mechanistic insights gleaned then serve as input for improving subsequent iterations. Moreover, the significance of *in operando* characterization cannot be overstated, with a previous report on Li-S cathodes noting different observations from *in operando* XRD and transmission X-ray microscopy, as compared to *ex situ* results.[225]

*4.2.3 Pre-sodiated materials*

Another alternative to covalent composites and sulfur hosts is the use of $Na_2S$ as active material instead.[144,226] In addition to avoiding further volumetric expansion with the cathode already in the sodiated state, a potential benefit is the option for full cell assembly with hard carbon,[227-230] graphitic,[231] or even oxide[232] and chalcogenide anodes without the need for anode pre-sodiation. In this regard, a 2020 report by Kaskel and co-workers demonstrated the first functional full cell Na-S battery, using a $Na_2S$-based cathode and a pristine hard carbon anode.[226] The FEC additive contributed to the formation of a stable SEI on the carbon anode and allowed the cell to achieve a specific capacity of 740 mAh $g_{(S)}^{-1}$, based on the cathode S-content. Na-battery systems with carbonaceous anodes could further allay safety concerns associated with metal-based anodes employed in the vast majority of Na-S batteries to date.

In addition to the above, another important consideration is the ease of the synthetic process, as the majority of current techniques require multi-step procedures that pose a challenge for industrial scaled-up production. Also related to this is the cost and availability of raw materials, with many of the precursors required today being expensive specialty chemicals. In spite of our continued pursuit for better battery performances, our overall focus should not detract from the overarching goal for Na-S batteries, as *sustainable* (both environmentally and economically) and cost-effective energy storage solutions based on earth-abundant Na and S.

### 4.3. Current limitations for practical adoption of sodium-sulfur batteries

#### *4.3.1. Working voltage and its impact on full-cell energy density*

Other than production and raw material costs, one key limitation of Na-S batteries that must be addressed is their practical energy densities. At the time of writing, latest figures released by the U.S. Department of Energy revealed a high practical energy density of 350 Wh $kg^{-1}$ currently achieved with Li-metal batteries in a pouch cell configuration, based on NMC622 (*i.e.* nickel manganese cobalt oxide) cathode chemistry.[233] Li-NMC systems typically operate

up to *ca*. 4.2 V *vs*. Li/Li$^+$, with a nominal cell voltage around 3.6 V. Li-S cells have a lower average voltage of around 2.2 V,[234] but can still reach practical energy densities of at least 350-600 Wh kg$^{-1}$ due to the high specific capacity of sulfur.[235,236] Although Na-S batteries function on similar cathode chemistries, they have a significantly lower working voltage range from about 0.6 V to 2.7 V, and a mid-point voltage *ca*. 1.7–1.8 V *vs*. Na/Na$^+$. This arises from the standard reduction potential of Li/Li$^+$ (−3.04 V) being more negative than Na/Na$^+$ at −2.71 V *vs*. standard hydrogen.[237] Notwithstanding this thermodynamic limit, Na-S batteries still have a high theoretical energy density of 1274 Wh kg$^{-1}$ to exploit (based on $Na_2S$ as the final discharge product),[103,139] and it is thus critical that these systems achieve high capacities by maximizing their sulfur utilization to reach practical energy densities comparable to their Li counterparts. While current Na-S systems might not be a competitive option for state-of-the-art high-power applications like electric vehicles, the abundance of their basic raw materials (both Na and S) puts Na-S batteries in good stead for large-scale stationary applications like grid-level storage, an opinion shared by us and others alike in the battery community.

Current estimates of Na-S battery gravimetric energy densities have been reported over a large range from around 380 Wh kg$^{-1}$ to over 1000 Wh kg$^{-1}$, based only on the cathode weight.[13,140,141,184,238] A 2019 report exploited the porous nature of a carbon cloth current collector for a Na polysulfide cathode, reaching a high 946 Wh kg$^{-1}$ based on the combined mass of sulfur and Na, and maintained a respectable 728 W h kg$^{-1}$ after 500 cycles.[239] Liu *et al*. recently demonstrated pouch cell cycling with energy density reaching 384 Wh kg$^{-1}$ after 30 cycles at a current density of 0.1 A g$^{-1}$ (**Figure 23**a).[140] Towards a more functional system, Pampel *et al*. designed a 10-layered pouch cell with double-side-coated electrodes (Figure 23b,c), achieving 1000 cycles with energy density at roughly ∼500 Wh kg$_{(S)}^{-1}$ (Figure 23d).[238] However, the authors noted that due to the low sulfur present (2.30 wt.%) over the weight of the full cell (inclusive of packaging), the overall energy density attained was just

~30 Wh $kg^{-1}$ in the initial cycles and 17 Wh $kg^{-1}$ at the 930$^{th}$ cycle, although the cell design itself could in theory deliver up to 109 Wh $kg^{-1}$ if optimized. Nonetheless, the long cycle life demonstrated in a pouch cell system represents a significant advance for practical Na-S batteries.

*4.3.2. Areal sulfur-loading and areal capacity*

Other than optimizing the composite S-content alone to improve energy densities, the areal mass loading of the composite or active material itself could also be increased. Increasing the areal S-loading however, would not come without difficulty. As outlined in the Introduction, one of the major challenges faced by Na-S batteries is pulverization of the cathode structure due to severe volumetric expansion/contraction cycles concomitant with the sodiation/desodiation process. Thus, any attempt at increasing the mass loading without improving mechanical adhesion would likely result in faster structural damage and capacity decay. Given the densities of $S_8$ (2.03 g $cm^{-3}$), $Na_2S$ (1.86 g $cm^{-3}$) and their molecular weights, the Na-S battery cathode is expected to undergo a volume expansion of about 170%, significantly greater than the 80% for a similar cathode put into a Li-S cell.[15] Unsurprisingly, areal S-loading for Na-S batteries have been kept fairly low in the literature to date, usually less than 2 $mg_{(S)}$ $cm^{-2}$, and this is also not a parameter commonly considered for optimization studies. As a point of comparison with Li-S batteries, their areal capacity has to reach at least ~4 mAh $cm^{-2}$ to compete with the average Li-ion battery,[236] or a minimum of 6 mAh $cm^{-2}$ to match state-of-the-art levels necessary for electric vehicle applications.[240] Even assuming 100% sulfur utilization, sulfur loads will need to reach at least 2.4 – 3.6 $mg_{(S)}$ $cm^{-2}$. In reality, Na-S batteries will require *even higher* areal sulfur loads to compensate for the difference in working voltage. More studies will definitely be required to address prevailing inadequacies in this regard.

Despite this, available approaches to boost areal sulfur loads include the employment of highly porous cathode architectures, be it through the use of porous carbon current collectors or free-standing structures such as electrospun fibers as seen in several examples earlier (though the volumetric capacity will remain largely unchanged). Another promising strategy to overcome Na-S cathode disintegration whilst improving overall mass loading is the use of *polar* binder systems, unlike conventional fluoropolymer binders such as PVDF which can adopt non-polar conformations (*e.g.* α and ε phases) due to their dipole orientations.[241] In particular, the polar functional groups of the binder not only act as excellent polysulfide anchors but more importantly confer good mechanical properties to accommodate large volume changes. One such example is the carboxyl moiety found in PAA, CMC and Na-alginate, which effectively prevented cathode pulverization as earlier discussed.[184] Other polar binder systems containing amides (*e.g.* PVP)[242] and amines (*e.g.* polyethylenimine)[243] have also been reported to enhance Li-S cycling performance, and it is very likely that their positive effects could extend to Na-S batteries as well.

*4.3.3. Electrode processing methods and scaled-up cell testing*

With Na-S batteries gaining much traction over the past several years, greater emphasis should now be placed on the development of material synthesis and electrode processing methods capable of production at a larger scale. For instance, the vast majority of Na-S studies to date have been conducted at the laboratory-scale, with active material syntheses typically producing no more than a couple of grams at a time. Instead, methodologies for scaled-up composite synthesis must be developed. This would allow for material compatibility tests with conventional battery production methods such as slurry mixing, coating, roll-to-roll processing (Figure 23c), or calendaring to be conducted. Only then can practical cell assemblies such as pouch, prismatic, or cylindrical (*e.g.* 18650) cell types be built and tested. Furthermore, full cell energy densities obtained from these cell types would

much better reflect actual usage conditions in the real-world, with cell packaging contributing a large proportion of the overall weight,[238] thus allowing for better optimization of important parameters such as the electrode mass loading, electrolyte-to-sulfur ratios, *etc*.

Given the higher reactivity of the Na anode over Li, one might also question if Na-metal or Na-ion batteries could eventually be assembled under typical dry room conditions employed for commercial Li-ion battery production. Industrial anode processing and cell assembly are mostly conducted in custom-built dry rooms today, with the moisture content below 100 ppm,[244,245] much unlike laboratory-scale gloveboxes kept strictly under inert atmospheres. More rigorous conditions for both moisture and oxygen would certainly be expected for metallic anodes, compared to graphitic/silicon-based anodes in Li-ion batteries. As a reference based on our experience, the oxygen content must be carefully maintained well below ~2-3 ppm when handling metallic Na to ensure good cycle reproducibility. One potential solution to this could be the use of anode coatings, which can serve as protective barriers against ambient moisture and/or oxygen. A recent proof-of-concept by Goodenough and colleagues showed that *metallic*-Li anodes could even be processed in moderately humid air (relative humidity *ca*. 20–35%), after reaction with graphite fluoride to form an artificial SEI consisting of both graphite fluoride and a lithium fluoride (LiF) layer on Li-metal foils.[246] Furthermore, the LiF also promoted stable dendrite-free plating, analogous to the effects of sodium fluoride (NaF) SEIs exhibiting good ionic conductivity and uniform Na strip/plating.[26] NaF could also act as an effective barrier against atmospheric contamination, possibly allowing for processing and conventional dry-room cell assembly, as seen with NaF-rich films suppressing $O_2$ crossover in the case of Na-$O_2$ batteries.[247]

To achieve *safer* Na-S batteries, concerns with regard to the flammability of liquid electrolytes can be further allayed by adopting solid-state electrolyte materials suited with current production practices. As detailed in Section 3.1.5, the glass-ceramic material, $Na_3SbS_4$ , exhibits excellent chemical stability in ambient environment for up to 48 h. One

may therefore reasonably expect it to also be compatible with dry-room conditions for cell assembly. When used in combination, these potentially air-stable processing methods for Na metal anodes, solid-state Na electrolytes and S-composite cathodes can serve as powerful strategies to achieve industry-ready production, bringing us a step closer towards realizing practical Na-S batteries.

### 4.4. Potassium-sulfur batteries and other alkali metal systems

Beyond Na-S batteries, other alkali-metal batteries have also attracted some interest within the community. Like Na, potassium (K) offers advantages over Li such as a comparable crustal/oceanic abundance at 1.84% (Na: 2.27%, *vs*. Li: 0.0018%).[248] In terms of its physical properties, the $K^+$ ion has the highest ionic conductivity and ion mobility of the three metals in common carbonate electrolyte combinations such as EC/DEC or EC/DMC (in the order of $K^+ > Na^+ > Li^+$), due to its larger size and polarizability.[249,250] More critically, potassium-sulfur (K-S) batteries can deliver high gravimetric energy densities of about 1023 Wh $kg^{-1}$ despite the weight of K,[251] by virtue of higher working potentials (lower reduction potential of K: $E° = -2.93$ V, compared to Na: $E° = -2.71$ V *vs.* SHE).[237] Of course, challenges faced by the S-cathode must still be addressed, with the volumetric expansion issue being especially harsh: the already severe 170% increase for Na-S battery cathodes would pale in comparison to the expected ~300% for the $S_8$ to $K_2S$ transition (Table 7).[251]

#### *4.4.1. Potassium-sulfur cathode chemistry*

With their similar sulfur chemistries, many Na-S battery strategies have thus been successfully applied to K-S battery systems. In the first demonstrated r.t. K-S battery system, Zhao *et al*. sought to address polysulfide dissolution with a conductive polymer coating.[252] Polyaniline (PANI) was used as an ion conductive polymer to coat S-infused (CMK-3) mesoporous carbons (**Figure 24**b). While the K-S battery could cycle up to 50 cycles, the

authors observed that the potassiation of $S_8$ could only proceed partially to give $K_2S_3$ as the main discharge product (Figure 24a),[252] which is noted for its high thermodynamic stability.[253] This resulted in a low initial discharge capacity of 512.7 mAh $g^{-1}$, and in agreement with the theoretical capacity for conversion to $K_2S_3$ at 558 mAh $g^{-1}$ (Figure 24c). They also noted higher reactivity of the dissolved K polysulfides compared to Li, experiencing some extent of shuttling to the K anode that resulted in Coulombic efficiencies below 95% for the first few cycles. Solubilities of K polysulfides also closely resembled those of Na polysulfides, where short-chain polysulfides ($K_2S_x$ , x =1–4) remained in the solid phase, while long-chain species ($K_2S_x$, $x \geq 5$) were highly soluble in ether electrolyte.[254]

Many other methods for cathode preparation were also largely analogous to Na-S battery systems, such as the impregnation of sulfur or polysulfide catholytes into porous nanofiber matrices,[254,255] and the employment of electrocatalysts like imidazole-solvated copper to facilitate full conversion of the $K_2S_3$ intermediate to $K_2S$ (Figure 24c). This provided an effective solution for its sluggish kinetics, and maximized sulfur utilization for higher capacities.[253] Further exploiting the insolubility of short-chain K polysulfides, short-chain sulfur composites could be obtained *via* encapsulation within microporous carbons[256] and as covalent-sulfur composites.[191,257,258]

To counter the serious cathode volumetric expansion and structural disintegration, Sun and co-workers provided a straightforward solution by replacement of the binder.[258] When a traditional PVDF binder was substituted with PAA, the S-PAN cathode maintained a higher capacity of 1050 mAh $g^{-1}$ after 100 cycles and a capacity retention of 95% (Figure 24d), compared to PVDF with only 22% of its initial capacity. Post-mortem analysis also revealed structural damage and detachment of the PVDF-cathode from the current collector *versus* the well-maintained PAA (Figure 24e). This again reiterates the importance of the right choice of binder, which we feel cannot be overemphasized. Alternative binders with strong interactions such as hydrogen-bonding and excellent mechanical properties have also been exploited as

means to accommodate volume expansion in a variety of other electrode materials and systems.[259-261]

*4.4.2. Potassium anodes and composites*

At the K anode, interesting approaches have been employed to prevent dendritic growth and allow reversible plating. Several anode substrates include NiO nanoparticles on porous carbon,[262] or free-standing structures like 3D graphene-coated copper,[263] CNTs,[264] and MXene/CNT scaffolds.[265] Such structures typically discourage dendrite formation by increasing the density of nucleation sites for K deposition. The low melting temperature of metallic K (~64 °C) also presents a unique opportunity for K infiltration into these structures, where the molten metal can be introduced by heating on a common laboratory hotplate between 70-100 °C.[264,265] Another class of anodes are K-alloying materials like bismuth,[266] antimony[267] or $Sn_4P_3$ composites[268] on carbon, and even a mercury amalgam[269] have also been reported, though these anode types still need to be tested for compatibility with S-cathodes.

However, perhaps the most fascinating property of K is its formation of a eutectic system with metallic Na at room temperature, with K-Na liquid alloys formed over a wide compositional range of *ca*. 42 wt.% to 92 wt.% K.[270-272] In addition to the benefit of dendrite-free plating, K-Na liquid alloys exhibit strong surface tension, allowing for high permeability throughout porous carbon current collectors, but are unable to wet or penetrate either glass fiber or polypropylene-based separators (Figure 24f-h). Most importantly, these K-Na liquid anodes are compatible with carbonate solvents and well-suited for cycling with S-based cathodes like S-PAN.[272] With a $KPF_6$ electrolyte in EC/DMC/EMC solvent cycled between 0.5 V and 3.0 V *vs*. $K/K^+$, S-PAN cathodes maintained higher capacity after 100 cycles with the K-Na anode (490 mAh $g^{-1}$), *versus* a pure-K cell with only 140 mAh $g^{-1}$ retained.

*4.4.3. Alkali metals as electrolyte additives*

Beyond Li, Na, and K, there exists little justification for any of the remaining heavy alkali metals (*i.e.* rubidium and cesium) to be employed as battery anodes. Nevertheless, their presence as electrolyte additives in Li- and Na-batteries has been shown to confer benefits. For instance, low concentrations (~0.05 M) of either $Rb^+$ or $Cs^+$ were noted to permit dendrite-free Li plating based on a "self-healing electrostatic shield" mechanism.[273] During the initial stages of Li deposition under regular conditions, any sharp edge or protrusion will inadvertently exhibit a stronger electric field, causing preferential $Li^+$ deposition at such areas compared to the smooth surface. In the presence of $Rb^+$ or $Cs^+$ species however, these large cations were found to accumulate around protrusions and act as positively charged "shields", but otherwise remain electrochemically inactive due to their lower (less negative) reduction potentials. As such, these cationic shields therefore re-direct incoming $Li^+$ to deposit at the adjacent regions and not contribute to further growth of the dendrite.

Also in the case of Na hard-carbon anodes, $Rb^+$ and $Cs^+$ ions were seen to aid the formation of a more stable SEI.[274] With a $NaPF_6$ carbonate electrolyte, the additives promoted decomposition of $PF_6^-$ anions to form a stable NaF–based SEI layer, while suppressing undesirable decomposition of the carbonate solvent.

Finally on a more fundamental level, alkali metal ions were also found to interact differently with polysulfide species from the cathode.[275] Interestingly, the large $Rb^+$ cation exhibited strong electrostatic interactions with short-chain polysulfides, facilitating the conversion of long-chain $S_8^{2-}$ species to $S_4^{2-}$ and $S_3^{2-}$ during discharge. However during the re-charge phase, the same polysulfide stabilization by larger $K^+$ and $Rb^+$ cations instead resulted in poorer reversibility, with lower capacity and Coulombic efficiency compared to the smaller $Li^+$ and $Na^+$ systems. These findings could have potential ramifications for the choice between short-chain sulfur composites or elemental sulfur as the active material.

## 5. Conclusions

Developments in Na-S and alkali-metal sulfur battery technologies have proliferated over the last 3 to 5 years. The energy storage community has a much better understanding of the fundamental challenges that we face today, and we are now well-equipped with accessible strategies to overcome them. Not only has progress been made with S-composites and host structures, but also in the engineering of stable anode interphases and electrolyte systems, leading to significant improvements in battery lifetime and performance. Now more than ever, greater emphasis should be accorded to the development of practical Na-S batteries, which includes various aspects summarized in this Review such as scalable synthetic processes, safer electrolytes, and high energy systems with increased cathode active material loads. It would certainly be exciting to watch the progress of Na-S batteries as we work towards both environmentally sustainable and economically viable solutions to meet our ever-increasing future energy needs.

## Conflicts of Interest

There are no conflicts to declare.


## Acknowledgements

This work was co-supported by the Singapore National Research Foundation (NRF-NRFF2017-04), Young Investigator Program funded by the U.S. Air Force Office of Scientific Research under award FA9550-17-1-0184, and from the start-up funds at Thayer School of Engineering, Dartmouth College. A. Y. S. Eng, V. Kumar, and Y. Zhang contributed equally to this work.

Received: ((will be filled in by the editorial staff))
Revised: ((will be filled in by the editorial staff))
Published online: ((will be filled in by the editorial staff))


## References

[1] E. Pomerantseva, F. Bonaccorso, X. Feng, Y. Cui, Y. Gogotsi, *Science* **2019**, *366*, eaan8285.

[2] M. Armand, J. M. Tarascon, *Nature* **2008**, *451*, 652-657.

[3] D. Lindley, *Nature* **2010**, *463*, 18-20.

[4] B. Dunn, H. Kamath, J. M. Tarascon, *Science* **2011**, *334*, 928-935.

[5] K. Mongird, V. Viswanathan, P. Balducci, J. Alam, V. Fotedar, V. Koritarov, B. Hadjerioua, *Energy Storage Technology and Cost Characterization Report*. No. PNNL-28866. Pacific Northwest National Lab.(PNNL), Richland, WA (United States), **2019**.

[6] R. Schmuch, R. Wagner, G. Hörpel, T. Placke, M. Winter, *Nat. Energy* **2018**, *3*, 267-278.

[7] B. Nykvist, M. Nilsson, *Nat. Clim. Change* **2015**, *5*, 329-332.

[8] A. Thielmann, M. Wietschel, S. Funke, A. Grimm, T. Hettesheimer, S. Langkau, A. Loibl, C. Moll, C. Neef, P. Plötz, L. Sievers, L. T. Espinoza, J. Edler, *Batteries for Electric Cars: Fact Check and Need for Action*, https://www.isi.fraunhofer.de/content/dam/isi/dokumente/cct/2020/Fact_check_Batteries_for_electric_cars.pdf, accessed: October, **2020**.

[9] C. Wesley, A. W. Frazier, *Cost Projections for Utility-Scale Battery Storage: 2020 Update*, National Renewable Energy Laboratory, NREL/TP-6A20-75385. https://www.nrel.gov/docs/fy20osti/75385.pdf, accessed: October, **2020**.

[10] Y. X. Wang, B. W. Zhang, W. H. Lai, Y. F. Xu, S. L. Chou, H. K. Liu, S. X. Dou, *Adv. Energy Mater.* **2017**, *7*, 1602829.

[11] S. Y. Wei, S. M. Xu, A. Agrawral, S. Choudhury, Y. Y. Lu, Z. Y. Tu, L. Ma, L. A. Archer, *Nat. Commun.* **2016**, *7*, 11722.

[12] H. L. Pan, Y. S. Hu, L. Q. Chen, *Energy Environ. Sci.* **2013**, *6*, 2338-2360.

[13] S. Xin, Y. X. Yin, Y. G. Guo, L. J. Wan, *Adv. Mater.* **2014**, *26*, 1261-1265.

[14] A. Manthiram, X. Yu, *Small* **2015**, *11*, 2108-2114.

[15] Z. W. Seh, Y. Sun, Q. Zhang, Y. Cui, *Chem. Soc. Rev.* **2016**, *45*, 5605-5634.

[16] D. R. Lide, in *CRC Handbook of Chemistry and Physics*, Section 14, Geophysics, Astronomy, and Acoustics; Abundance of Elements in the Earth's Crust and in the Sea, 85th Edition, (Ed: J. R. Rumble), CRC Press, Boca Raton, Florida, USA, **2005**.

[17] Y. Wang, D. Zhou, V. Palomares, D. Shanmukaraj, B. Sun, X. Tang, C. Wang, M. Armand, T. Rojo, G. Wang, *Energy Environ. Sci.* **2020**, *13*, 3848-3879.

[18] Z. Wen, J. Cao, Z. Gu, X. Xu, F. Zhang, Z. Lin, *Solid State Ion.* **2008**, *179*, 1697-1701.

[19] C.-W. Park, J.-H. Ahn, H.-S. Ryu, K.-W. Kim, H.-J. Ahn, *Electrochem. Solid-State Lett.*, **2006**, *9*, A123-A125.

[20] X. Yu, A. Manthiram, *ChemElectroChem* **2014**, *1*, 1275-1280.

[21] I. Bauer, M. Kohl, H. Althues, S. Kaskel, *Chem. Commun.* **2014**, *50*, 3208-3210.

[22] C.-W. Park, H.-S. Ryu, K.-W. Kim, J.-H. Ahn, J.-Y. Lee, H.-J. Ahn, *J. Power Sources* **2007**, *165*, 450-454.

[23] J. Yue, F. Han, X. Fan, X. Zhu, Z. Ma, J. Yang, C. Wang, *ACS Nano* **2017**, *11*, 4885-4891.

[24] H. Ryu, T. Kim, K. Kim, J.-H. Ahn, T. Nam, G. Wang, H.-J. Ahn, *J. Power Sources* **2011**, *196*, 5186–5190.

[25] Y. Wang, Y. Hao, L.-C. Xu, Z. Yang, M.-Y. Di, R. Liu, X. Li, *J. Phys. Chem. C*, **2019**, *123*, 3988-3995.

[26] Z. W. Seh, J. Sun, Y. Sun, Y. Cui, *ACS Cent. Sci.* **2015**, *1*, 449−455.

[27] S. E. Lee, M. H. Tang, *Electrochem. Commun.* **2019**, *100*, 70–73.

[28] G. G. Eshetu, G. A. Elia, M. Armand, M. Forsyth, S. Komaba, T. Rojo, S. Passerini, *Adv. Energy Mater.* **2020**, *10*, 2000093.

[29] C. Geng, D. Buchholz, G. T. Kim, D. V. Carvalho, H. Zhang, L. G. Chagas, S. Passerini, *Small Methods* **2018**, *3*, 1800208.

[30] H. Chu, H. Noh, Y. J. Kim, S. Yuk, J. H. Lee, J. Lee, H. Kwack, Y. K. Kim, D. K. Yang, H. T. Kim, *Nat. Commun.* **2019**, *10*, 7914.

[31] V. Gutmann, *Electrochemica. Acta.* **1976**, *21*, 661.

[32] Q. Zou, Y. C. Lu, *J. Phys. Chem. Lett.* **2016**, *7*, 1518−1525.

[33] M. Cuisinier, C. Hart, M. Balasubramanian, A. Garsuch, L. F. Nazar, *Adv. Energy Mater.* **2015**, *5*, 1401801.

[34] I. Gunasekara, S. Mukerjee, E. J. Plichta, M. A. Hendrickson, K. M. Abraham, *J. Electrochem. Soc.* **2015**, *162*, A1055-A1066.

[35] L. Lutz, D. A. D. Corte, M. Tang, E. Salager, M. Deschamps, A. Grimaud, L. Johnson, P. G. Bruce, J. M. Tarascon, *Chem. Mater*. **2017**, *29*, 6066−6075.

[36] D. G. Kwabi, M. Tulodziecki, N. Pour, D. M. Itkis, C. V. Thompson, Y. S. Horn, *J. Phys. Chem. Lett.* **2016**, *7*, 1204−1212.

[37] E. Peled, *J. Electrochem. Soc.* **1979**, *126*, 2047.

[38] H. Yang, G. V. Zhuang, P. N. Ross Jr., *J. Power Sources* **2006**, *161*, 573–579.

[39] Y. Yamada, A. Yamada, *J. Electrochem. Soc.* **2015**, *162*, A2406-A2423.

[40] Y. Yamada, K. Furukawa, K. Sodeyama, K. Kikuchi, M. Yaegashi, Y.Tateyama, A. Yamada, *J. Am. Chem. Soc.* **2014**, *136*, 5039−5046.

[41] X. Ren, L. Zou, S. Jiao, D. Mei, M. H. Engelhard, Q. Li, H. Lee, C. Niu, B. D. Adams, C. Wang, J. Liu, J. G. Zhang, W. Xu, *ACS Energy Lett.* **2019**, *4*, 896−902.

[42] Y. Yamada, J. Wang, S. Ko, E. Watanabe, A. Yamada, *Nat. Energy* **2019**, *4*, 269.

[43] D. Brouillette, D. E. Irish, N. J. Taylor, G. Perron, M. Odziemkowski, J. E. Desnoyers, *Phys. Chem. Chem. Phys.* **2002**, *4*, 6063–6071.

[44] W. A. Henderson, N. R. Brooks, V. G. Young Jr., *Chem. Mater.* **2003**, *15*, 4685-4690.

[45] W. A. Henderson, N. R. Brooks, *Inorg. Chem.* **2003**, *42*, 15.

[46] J. Lee, Y. Lee, J. Lee, S. M. Lee, J. H. Choi, H. Kim, M. S. Kwon, K. Kang, K. T. Lee, N. S. Choi, *ACS Appl. Mater. Interfaces* **2017**, *9*, 3723−3732.

[47] M. He, K. C. Lau, X. Ren, N. Xiao, W. D. McCulloch, L. A. Curtiss, Y. Wu, *Angew. Chem. Int. Ed.* **2016**, *55*, 15310 –15314.

[48] A. Khetan, H. R. Arjmandi, V. Pande, H. Pitsch, V. Viswanathan, *J. Phys. Chem. C* **2018**, *122*, 8094−8101.

[49] D. M. Seo, O. Borodin, S. D. Han, Q. Ly, P. D. Boyle, and W. A. Henderson, *J. Electrochem. Soc.* **2012**, *159*, A553-A565.

[50] R. Cao, K. Mishra, X. Li, J. Qian, M. H. Engelhard, M. E. Bowden, K. S. Han, K. T. Mueller, W. A.Henderson, J. G. Zhang, *Nano Energy* **2016**, *30*, 825–830.

[51] J. Zheng, S. Chen, W. Zhao, J. Song, M. H. Engelhard, J. G. Zhang, *ACS Energy Lett.* **2018**, *3*, 315−321.

[52] D. R. Martınez, A. Kovacs, R. Gomez, *Energy Environ. Sci.* **2017**, *10*, 1936-1941.

[53] D. R. Martínez, R. Gomez, *Energy Storage Mater.* **2019**, *22*, 424–432.

[54] J. B. Lambling, M. Bardin, C. Bernard, B. Fahys, M. Herlem, A. Thiebault, G. Robert, *J. Electrochem. Soc.* **1988**, *135*, 587.

[55] L. E. C. Forero, P. B. Balbuena, *Phys. Chem. Chem. Phys.* **2017**, *19*, 30861.

[56] G. Nikiforidis, M. C. M. van de Sanden, M. N. Tsampas, *RSC Adv.* **2019**, *9*, 5649.

[57] J. W. Fergus, *J. Power Sources* **2010**, *195*, 4554–4569.

[58] K. Vignarooban, R. Kushagra, A. Elango, P. Badami, B. E. Mellander, X. Xu, T.G. Tucker, C. Nam, A. M. Kannan, *Int. J. Hydro. Energy* **2016**, *41*, 2829.

[59] D. Kumar, S.A. Hashmi, *J. Power Sources* **2010**, *195*, 5101–5108.

[60] Y. Xue and D. J. Quesnel, *RSC Adv.* **2016**, *6*, 7504.

[61] H. Gao, W. Zhou, K. Park, J. B. Goodenough, *Adv. Energy Mater.* **2016**, *6*, 1600467.

[62] S. Abbrent, J. Plestil, D. Hlavata, J. Lindgren, J. Tegenfeldt, A. Wendsjo, *Polymer*, **2001**, *42*, 1407–1416.

[63] D. Kumar, S.A. Hashmi, *Solid State Ion.* **2010**, *181*, 416–423.

[64] L. Long, S. Wang, M. Xiao, Y. Meng, *J. Mater. Chem. A* **2016**, *4*, 10038.

[65] K. Mishra, T. Arif, R. Kumar, D. Kumar, *J. Solid State Electr.* **2019**, *23*, 2401–2409.

[66] D. Lei, Y. B. He, H. Huang, Y. Yuan, G. Zhong, Q. Zhao, X. Hao, D. Zhang, C. Lai, S. Zhang, J. Ma, Y. Wei, Q. Yu, W. Lv, Y. Yu, B. Li, Q. H. Yang, Y. Yang, J. Lu, F. Kang, *Nat. Commun.* **2019**, *10*, 4244.

[67] C. Luo, T. Shen, H. Ji, D. Huang, J. Liu, B. Ke, Y. Wu, Y. Chen, C. Yan, *Small* **2019**, *16*, 1906208.

[68] Y. G. Cho, C. Hwang, D. S. Cheong, Y. S. Kim, H. K. Song, *Adv. Mater.* **2019**, *31*, 1804909.

[69] B. Wu, S. Wang, J. Lochala, D. Desrochers, B. Liu, W. Zhang, J. Yang, J. Xiao, *Energy Environ. Sci.* **2018**, *11*, 1803-1810.

[70] H. Liu, X.-B. Cheng, J.-Q. Huang, H. Yuan, Y. Lu, C. Yan, G.-L. Zhu, R. Xu, C.-Z. Zhao, L.-P. Hou, C. He, S. Kaskel, Q. Zhang, *ACS Energy Lett.* **2020**, *5*, 833–843.

[71] B. Lee, E. Paek, D. Mitlin, S. W. Lee, *Chem. Rev.* **2019**, *119*, 5416−5460.

[72] J. Zheng, Y. Zhao, X. Feng, W. Chen, Y. Zhao, *J. Mater. Chem. A* **2018**, *6*, 6559.

[73] J. I. Kim, Y. Choi, K. Y. Chung, J. H. Park, *Adv. Funct. Mater.* **2017**, *27*, 1701768.

[74] H. Che, S. Chen, Y. Xie, H. Wang, K. Amine, X. Z. Liao, Z. F. Ma, *Energy Environ. Sci.* **2017**, *10*, 1075.

[75] K. Noi, A. Hayashi, M. Tatsumisago, *J. Power Sources* **2014**, *269*, 260-265.

[76] M. Guin, F. Tietz, *J. Power Sources* **2015**, *273*, 1056-1064.

[77] S. Wenzel, T. Leichtweiss, D. A. Weber, J. Sann, W. G. Zeier, J. Janek, *ACS Appl. Mater. Interfaces* **2016**, *8*, 28216−28224.

[78] T. Honma, M. Okamoto, T. Togashi, N. Ito, K. Shinozaki, T. Komatsu, *Solid State Ion.* **2015**, *269*, 19–23.

[79] T. Okada, T. Honma, T. Komatsu, *Mater. Res. Bull.* **2010**, *45*, 1443-1448.

[80] X. Yu, A. Manthiram, *Matter* **2019**, *1*, 439–451.

[81] M. H. Braga, A. J. Murchison, J. A. Ferreira, P. Singh, J. B. Goodenough, *Energy Environ. Sci*. **2016**, *9*, 948.

[82] M. H. Braga, N. S. Grundish, A. J. Murchison, J. B. Goodenough, *Energy Environ. Sci.* **2017**, *10*, 331.

[83] E. Peled, S. Menkin, *J. Electrochem. Soc.* **2017**, *164*, A1703-A1719.

[84] X. Zhang, A. Wang, X. Liu, J. Luo, *Acc. Chem. Res*. **2019**, *52*, 3223−3232.

[85] Y. He, X. Ren, Y. Xu, M. H. Engelhard, X. Li, J. Xiao, J. Liu, J. G. Zhang, W. Xu, C. Wang, *Nat. Nanotechnol*. **2019**, *14*, 1042.

[86] X. B. Cheng, R. Zhang, C. Z. Zhao, F. Wei, J. G. Zhang, Q. Zhang, *Adv. Sci.* **2016**, *3*, 1500213.

[87] Y. Li, Y. Li, A. Pei, K. Yan, Y. Sun, C. L. Wu, L. M. Joubert, R. Chin, A. L. Koh, Y. Yu, J. Perrino, B. Butz, S. Chu, Y. Cui, *Science* **2017**, *358*, 506–510.

[88] M. J. Zachman, Z. Tu, S. Choudhury, L. A. Archer, L. F. Kourkoutis, *Nature* **2018**, *560*, 345.

[89] V. Kumar, Y. Wang, A. Y. S. Eng, M. F. Ng, Z. W. Seh, *Cell Rep. Phys. Sci.* **2020**, *1*, 100044.

[90] M. Han, C. Zhu, T. Ma, Z. Pan, Z. Tao, J. Chen, *Chem. Commun.* **2018**, *54*, 2381.

[91] Y. Zhao, J. Liang, Q. Sun, L. V. Goncharova, J. Wang, C. Wang, K. R. Adair, X. Li, F. Zhao, Y. Sun, R. Li, X. Sun, *J. Mater. Chem. A* **2019**, *7*, 4119.

[92] M. Brocklebank, J. J. Noël, L. V. Goncharova, *J. Electrochem. Soc.* **2019**, *166*, C3290-C3296.

[93] P. M. Bayley, N. M. Trease, C. P. Grey, *J. Am. Chem. Soc.* **2016**, *138*, 1955−1961.

[94] H. Kondou, J. Kim, H. Watanabe, *Electrochemistry* **2017**, *85*, 647–649.

[95] Z. Shen, W. Zhang, G. Zhu, Y. Huang, Q. Feng, Y. Lu, *Small Method*s **2020**, *4*, 1900592.

[96] R. Dugas, A. Ponrouch, G. Gachot, R. David, M. R. Palacin, J. M. Tarascon, *J. Electrochem. Soc.* **2016**, *163*, A2333-A2339. 

[97] X. Q. Zhang, X. B. Cheng, X. Chen, C. Yan, Q. Zhang, *Adv. Funct. Mater.* **2017**, *27*, 1605989.

[98] Q. Zhang, Y. Lu, L. Miao, Q. Zhao, K. Xia, J. Liang, S. L. Chou, *J. Chen, Angew. Chem. Int. Ed.* **2018**, *57*, 14796 –14800.

[99] Q. Shi, Y. Zhong, M. Wu, H. Wang, H. Wang, *Angew. Chem. Int. Ed.* **2018**, *57*, 9069 – 9072.

[100] Y. Lee, J. Lee, J. Lee, K. Kim, A. Cha, S. Kang, T. Wi, S. J. Kang, H. W. Lee, N. S. Choi, *ACS Appl. Mater. Interfaces*, **2018**, *10*, 15270−15280.

[101] H. Wang, C. Wang, E. Matios, W. Li, *Angew. Chem. Int. Ed*. **2018**, *57*, 7734 –7737.

[102] X. Zheng, H. Fu, C. Hu, H. Xu, Y. Huang, J. Wen, H. Sun, W. Luo, Y. Huang, *J. Phys. Chem. Lett.* **2019**, *10*, 707−714.

[103] X. Xu, D. Zhou, X. Qin, K. Lin, F. Kang, B. Li, D. Shanmukaraj, T. Rojo, M. Armand, G. Wang, *Nat. Commun.* **2018**, *9*, 3870.

[104] W. Li, H. Yao, K. Yan, G. Zheng, Z. Liang, Y.-M. Chiang, Y. Cui, *Nat. Commun.* **2015**, *6*, 7436.

[105] V. Kumar, A. Y. S. Eng, Y. Wang, D. T. Nguyen, M. F. Ng, Z. W. Seh, *Energy Storage Mater.* **2020**, *29*, 1–8.

[106] D. Lin, Y. Liu, Y. Cui, *Nat. Nanotechnol.* **2017**, *12*, 194.

[107] S. Choudhury, S. Wei, Y. Ozhabes, D. Gunceler, M. J. Zachman, Z. Tu, J. H. Shin, P. Nath, A. Agrawal, L. F. Kourkoutis, T. A. Arias, L. A. Archer, *Nat. Commun.* **2017**, *8*, 898.

[108] Z. Tu, S. Choudhury, M. J. Zachman, S. Wei, K. Zhang, L. F. Kourkoutis, L. A. Archer, *Nat. Energy* **2018**, *3*, 310.

[109] S. Wei, S. Choudhury, J. Xu, P. Nath, Z. Tu, L. A. Archer, *Adv. Mater.* **2017**, *29*, 1605512.

[110] Y. Zhao, L. V. Goncharova, A. Lushington, Q. Sun, H. Yadegari, B. Wang, W. Xiao, R. Li, X. Sun, *Adv. Mater.* **2017**, *29*, 1606663.

[111] W. Luo, C. Fu Lin, O. Zhao, M. Noked, Y. Zhang, G. W. Rubloff, L. Hu, *Adv. Energy Mater.* **2017**, *7*, 1601526.

[112] Y. Zhao, L. V. Goncharova, Q. Zhang, P. Kaghazchi, Q. Sun, A. Lushington, B. Wang, R. Li, X. Sun, *Nano Lett.* **2017**, *17*, 5653−5659.

[113] H. Tian, Z. W. Seh, K. Yan, Z. Fu, P. Tang, Y. Lu, R. Zhang, D. Legut, Y. Cui, Q. Zhang, *Adv. Energy Mater.* **2017**, *7*, 1602528.

[114] D. H. Snydacker, V. I. Hegde, C. Wolverton, *J. Electrochem. Soc*. **2017**, *164*, A3582-A3589.

[115] H. Wang, C. Wang, E. Matios, W. Li, *Nano Lett.* **2017**, *17*, 6808−6815.

[116] D. Zhang, B. Li, S. Wang, S. Yang, *ACS Appl. Mater. Interfaces* **2017**, *9*, 40265−40272.

[117] Y. J. Kim, H. Lee, H. Noh, J. Lee, S. Kim, M. H. Ryou, Y. M. Lee, H. T. Kim, *ACS Appl. Mater. Interfaces* **2017**, *9*, 6000−6006.

[118] N. Delaporte, Y. Wang, K. Zaghib, *Front. Mater*. **2019**, *6*, 267.

[119] S. Wang, J. Wang, J. Liu, H. Song, Y. Liu, P. Wang, P. He, J. Xu, H. Zhou, *J. Mater. Chem. A* **2018**, *6*, 21248.

[120] Y. Gu, W. W. Wang, Y. J. Li, Q. H. Wu, S. Tang, J. W. Yan, M. S. Zheng, D. Y. Wu, C. H. Fan, W. Q. Hu, Z. B. Chen, Y. Fang, Q. H. Zhang, Q. F. Dong, B. W. Mao, *Nat. Commun.* **2018**, *9*, 1339.

[121] Y. Gu, W. W. Wang, J. W. He, S. Tang, H. Y. Xu, J. W. Yan, Q. H. Wu, X. B. Lian, M. S. Zheng, Q. F. Dong, B. W. Mao, *ChemElectroChem* **2018**, *5*, 1–9.

[122] X. Yu, A. Manthiram, *J. Phys. Chem. C* **2014**, *118*, 22952-22959.

[123] X. Yu, A. Manthiram, *J. Phys. Chem. Lett.* **2014**, *5*, 1943-1947.

[124] A. P. V. K. Saroja, K. Muthusamy, R. Sundara, *Adv. Mater. Interfaces* **2019**, *6*, 1901497.

[125] A. Kumar, A. Ghosh, M. Forsyth, D. R. MacFarlane, S. Mitra, *ACS Energy Lett.* **2020**, *5*, 2112-2121.

[126] D. Ma, Y. Li, J. Yang, H. Mi, S. Luo, L. Deng, C. Yan, M. Rauf, P. Zhang, X. Sun, X. Ren, J. Li, H. Zhang, *Adv. Funct. Mater.* **2018**, *28*, 1705537.

[127] A. Ghosh, A. Kumar, A. Roy, M. R. Panda, M. Kar, D. R. MacFarlane, S. Mitra, *ACS Appl. Mater. Interfaces* **2019**, *11*, 14101-14109.

[128] K. R. G. Lim, A. D. Handoko, S. K. Nemani, B. Wyatt, H.-Y. Jiang, J. Tang, B. Anasori, Z. W. Seh, *ACS Nano* **2020**, *14*, 10834–10864.

[129] W. Bao, C. E. Shuck, W. Zhang, X. Guo, Y. Gogotsi, G. Wang, *ACS Nano* **2019**, *13*, 11500-11509.

[130] X. Huo, Y. Liu, R. Li, J. Li, *Ionics* **2019**, *25*, 5373-5382.

[131] S. Zheng, P. Han, Z. Han, P. Li, H. Zhang, J. Yang, *Adv. Energy Mater.* **2014**, *4*, 1400226.

[132] P. Li, L. Ma, T. Wu, H. Ye, J. Zhou, F. Zhao, N. Han, Y. Wang, Y. Wu, Y. Li, J. Lu, *Adv. Energy Mater.* **2018**, *8*, 1800624.

[133] B. W. Zhang, Y. D. Liu, Y. X. Wang, L. Zhang, M. Z. Chen, W. H. Lai, S. L. Chou, H. K. Liu, S. X. Dou, *ACS Appl. Mater. Interfaces* **2017**, *9*, 24446-24450.

[134] B. W. Zhang, T. Sheng, Y. D. Liu, Y. X. Wang, L. Zhang, W. H. Lai, L. Wang, J. Yang, Q. F. Gu, S. L. Chou, H. K. Liu, S. X. Dou, *Nat. Commun.* **2018**, *9*, 4082.

[135] Z. Yan, Y. Liang, J. Xiao, W. Lai, W. Wang, Q. Xia, Y. Wang, Q. Gu, H. Lu, S. L. Chou, Y. Liu, H. Liu, S. X. Dou, *Adv. Mater.* **2020**, *32*, 1906700.

[136] R. Zhang, A. M. Esposito, E. S. Thornburg, X. Chen, X. Zhang, M. A. Philip, A. Magana, A. A. Gewirth, *ACS Appl. Mater. Interfaces* **2020**, *12*, 29285-29295.

[137] Q. Ma, G. Du, B. Guo, W. Tang, Y. Li, M. Xu, C. Li, *Chem. Eng. J.* **2020**, *388*, 124210.

[138] B. W. Zhang, T. Sheng, Y. X. Wang, S. Chou, K. Davey, S. X. Dou, S. Z. Qiao, *Angew. Chem. Int. Ed.* **2019**, *58*, 1484-1488.

[139] Z. Yan, J. Xiao, W. Lai, L. Wang, F. Gebert, Y. Wang, Q. Gu, H. Liu, S. L. Chou, H. Liu, S. X. Dou, *Nat. Commun.* **2019**, *10*, 4793.

[140] H. Liu, W. Pei, W. H. Lai, Z. Yan, H. Yang, Y. Lei, Y. X. Wang, Q. Gu, S. Zhou, S. Chou, H. K. Liu, S. X. Dou, *ACS Nano* **2020**, *14*, 7259–7268.

[141] N. Wang, Y. Wang, Z. Bai, Z. Fang, X. Zhang, Z. Xu, Y. Ding, X. Xu, Y. Du, S. Dou, G. Yu, *Energy Environ. Sci.* **2020**, *13*, 562-570.

[142] C. Ye, Y. Jiao, D. Chao, T. Ling, J. Shan, B. Zhang, Q. Gu, K. Davey, H. Wang, S. Z. Qiao, *Adv. Mater.* **2020**, *32*, 1907557.

[143] Y.-X. Wang, J. Yang, W. Lai, S.-L. Chou, Q. Gu, H. K. Liu, D. Zhao, S. X. Dou, *J. Am. Chem. Soc.* **2016**, *138*, 16576.

[144] C. Wang, H. Wang, X. Hu, E. Matios, J. Luo, Y. Zhang, X. Lu, W. Li, *Adv. Energy Mater.* **2019**, *9*, 1803251.

[145] D. Zhou, D. Shanmukaraj, A. Tkacheva, M. Armand, G. Wang, *Chem* **2019**, *5*, 2326-2352.

[146] J.-S. Kim, H.-J. Ahn, I.-P. Kim, K.-W. Kim, J.-H. Ahn, C.-W. Park, H.-S. Ryu, *J. Solid State Electrochem.* **2008**, *12*, 861-865.

[147] D. Kumar, M. Suleman, S. A. Hashmi, *Solid State Ion.* **2011**, *202*, 45-53.

[148] X. Yu, A. Manthiram, *Phys. Chem. Chem. Phys.* **2015**, *17*, 2127-2136.

[149] K. M. Kim, N.-G. Park, K. S. Ryu, S. H. Chang, *Electrochim. Acta* **2006**, *51*, 5636-5644.

[150] X. Hu, Y. Ni, C. Wang, H. Wang, E. Matios, J. Chen, W. Li, *Cell Rep. Phys. Sci.* **2020**, *1*, 100015.

[151] D. Zhou, Y. Chen, B. Li, H. Fan, F. Cheng, D. Shanmukaraj, T. Rojo, M. Armand, G. Wang, *Angew. Chem. Int. Ed.* **2018**, *57*, 10168-10172.

[152] C. Cao, W. Liu, L. Tan, X. Liao, L. Li, *Chem. Commun.* **2013**, *49*, 11740-11742.

[153] X. Yu, A. Manthiram, *Adv. Energy Mater.* **2015**, *5*, 1500350.

[154] X. Yu, A. Manthiram, *Chem. Mater.* **2016**, *28*, 896-905.

[155] Y. X. Ren, H. R. Jiang, T. S. Zhao, L. Zeng, C. Xiong, *J. Power Sources* **2018**, *396*, 304-313.

[156] X. Yu, S. Feng, M. J. Boyer, M. Lee, R. C. Ferrier, N. A. Lynd, G. S. Hwang, G. Wang, S. Swinnea, A. Manthiram, *Mater. Today Energy* **2018**, *7*, 98-104.

[157] Z. Ge, J. Li, J. Liu, *Ionics* **2020**, *26*, 1787-1795.

[158] T. Zhu, X. Dong, Y. Liu, Y.-G. Wang, C. Wang, Y.-Y. Xia, *ACS Appl. Energy Mater.* **2019**, *2*, 5263-5271.

[159] M. Patel, K. G. Chandrappa, A. J. Bhattacharyya, *Solid State Ion.* **2010**, *181*, 844-848.

[160] K. M. Freitag, P. Walke, T. Nilges, H. Kirchhain, R. J. Spranger, L. van Wüllen, *J. Power Sources* **2018**, *378*, 610-617.

[161] S. Wenzel, H. Metelmann, C. Raiß, A. K. Dürr, J. Janek, P. Adelhelm, *J. Power Sources* **2013**, *243*, 758-765.

[162] I. Kim, J.-Y. Park, C. H. Kim, J.-W. Park, J.-P. Ahn, J.-H. Ahn, K.-W. Kim, H.-J. Ahn, *J. Power Sources* **2016**, *301*, 332-337.

[163] N. Kamaya, K. Homma, Y. Yamakawa, M. Hirayama, R. Kanno, M. Yonemura, T. Kamiyama, Y. Kato, S. Hama, K. Kawamoto, A. Mitsui, *Nat. Mater.* **2011**, *10*, 682-686.

[164] A. Hayashi, K. Noi, A. Sakuda, M. Tatsumisago, *Nat. Commun.* **2012**, *3*, 856.

[165] N. J. J. de Klerk, M. Wagemaker, *Chem. Mater.* **2016**, *28*, 3122-3130.

[166] A. Hayashi, K. Noi, N. Tanibata, M. Nagao, M. Tatsumisago, *J. Power Sources* **2014**, *258*, 420-423.

[167] H. Nagata, Y. Chikusa, *Chem. Lett.* **2014**, *43*, 1333-1334.

[168] N. Tanibata, H. Tsukasaki, M. Deguchi, S. Mori, A. Hayashi, M. Tatsumisago, *Solid State Ion.* **2017**, *311*, 6-13.

[169] N. Tanibata, M. Deguchi, A. Hayashi, M. Tatsumisago, *Chem. Mater.* **2017**, *29*, 5232-5238.

[170] I. H. Chu, C. S. Kompella, H. Nguyen, Z. Zhu, S. Hy, Z. Deng, Y. S. Meng, S. P. Ong, *Sci. Rep.* **2016**, *6*, 33733.

[171] X. Fan, J. Yue, F. Han, J. Chen, T. Deng, X. Zhou, S. Hou, C. Wang, *ACS Nano* **2018**, *12*, 3360-3368.

[172] T. Krauskopf, C. Pompe, M. A. Kraft, W. G. Zeier, *Chem. Mater.* **2017**, *29*, 8859-8869.

[173] N. Tanibata, K. Noi, A. Hayashi, M. Tatsumisago, *RSC Adv.* **2014**, *4*, 17120-17123.

[174] Y. Hibi, N. Tanibata, A. Hayashi, M. Tatsumisago, *Solid State Ion.* **2015**, *270*, 6-9.

[175] H. Wang, Y. Chen, Z. D. Hood, G. Sahu, A. S. Pandian, J. K. Keum, K. An, C. Liang, *Angew. Chem. Int. Ed.* **2016**, *55*, 8551-8555.

[176] A. Banerjee, K. H. Park, J. W. Heo, Y. J. Nam, C. K. Moon, S. M. Oh, S. T. Hong, Y. S. Jung, *Angew. Chem. Int. Ed.* **2016**, *55*, 9634-9638.

[177] L. Zhang, D. Zhang, K. Yang, X. Yan, L. Wang, J. Mi, B. Xu and Y. Li, *Adv. Sci.*, **2016**, *3*, 1600089.

[178] H. Wan, W. Weng, F. Han, L. Cai, C. Wang, X. Yao, *Nano Today* **2020**, *33*, 100860.

[179] T. Ando, A. Sakuda, M. Tatsumisago, A. Hayashi, *Electrochem. Commun.* **2020**, *116*, 106741.

[180] J. Wang, J. Yang, J. Xie, N. Xu, *Adv. Mater.* **2002**, *14*, 963-965.

[181] T. H. Hwang, D. S. Jung, J.-S. Kim, B. G. Kim, J. W. Choi. *Nano Lett.* **2013**, *13*, 4532−4538.

[182] J. Wang, J. Yang, Y. Nuli, R. Holze, *Electrochem. Commun.* **2007**, *9*, 31–34.

[183] I. Kim, C. H. Kim, S. H. Choi, J.-P. Ahn, J.-H. Ahn, K.-W. Kim, E. J. Cairns, H.-J. Ahn, *J. Power Sources* **2016**, *307*, 31-37.

[184] A. Y. S. Eng, D.-T. Nguyen, V. Kumar, G. S. Subramanian, M.-F. Ng, Z. W. Seh, *J. Mater. Chem. A* **2020**, *8*, 22983-22997.

[185] L. Zeng, Y. Yao, J. Shi, Y. Jiang, W. Li, L. Gu, Y. Yu, *Energy Storage Mater.* **2016**, *5*, 50–57.

[186] Z. Li, J. Zhang, Y. Lu, X. W. Lou, *Sci Adv.* **2018**, *4*, eaat1687.

[187] L. Wang, X. Chen, S. Li, J. Yang, Y. Sun, L. Peng, B. Shan, J. Xie, *J. Mater. Chem. A* **2019**, *7*, 12732–12739.

[188] V. Pham, J. Boscoboinik, D. Stacchiola, E. Self, P. Manikandan, S. Nagarajan, Y. Wang, V. Pol, J. Nanda, E. Paek, D. Mitlin, *Energy Storage Mater.* **2019**, *20*, 71-79.

[189] T. An, H. Jia, L. Peng and J. Xie, *ACS Appl. Mater. Interfaces* **2020**, *12*, 20563−20569.

[190] S. Li, Z. Zeng, J. Yang, Z. Han, W. Hu, L. Wang, J. Ma, B. Shan, J. Xie, *ACS Appl. Energy Mater.* **2019**, *2*, 2956-2964.

[191] S. Ma, P. Zuo, H. Zhang, Z. Yu, C. Cui, M. He, G. Yin, *Chem. Commun.* **2019**, *55*, 5267.

[192] A. Abouimrane, D. Dambournet, K. W. Chapman, P.J. Chupas, W. Weng, K. Amine, *J. Am. Chem. Soc.* **2012**, *134*, 4505–4508.

[193] X. Li, J. Liang, K. Zhang, Z. Hou, W. Zhang, Y. Zhu, Y. Qian, *Energy Environ. Sci.* **2015**, *8*, 3181—3186.

[194] Y. Zhang, Y. Sun, L. Peng, J. Yang, H. Jia, Z. Zhang, B. Shan, J. Xie, *Energy Storage Mater*. **2019**, *21*, 287−296.

[195] W. Chung, J. Griebel, E. Kim, H. Yoon, A. Simmonds, H. Ji, P. Dirlam, R. Glass, J. Wie, N. Nguyen, B. Guralnick, J. Park, Á. Somogyi, P. Theato, M. Mackay, Y. Sung, K. Char, J. Pyun, *Nat. Chem.* **2013**, *5*, 518-524.

[196] A. Simmonds, J. Griebel, J. Park, K. Kim, W. Chung, V. Oleshko, J. Kim, E. Kim, R. Glass, C. Soles, Y. Sung, K. Char, J. Pyun, *ACS Macro Lett.* **2014**, *3*, 229-232.

[197] A. Ghosh, S. Shukla, M. Monisha, A. Kumar, B. Lochab, S. Mitra, *ACS Energy Lett.*, **2017**, *2*, 2478−2485.

[198] K. Chen, H. J. Wei Li, Y. Xu, K. Liu, H. Li, X. Xu, X. Qiu, M. Liu, *Nanoscale* **2019**, *11*, 5967.

[199] T. Wu, M. Jing, L. Yang, G. Zou, H. Hou, Y. Zhang, Y. Zhang, X. Cao, X. Ji, *Adv.*

*Energy Mater.* **2019**, *9*, 1803478.

[200] J. Yan, W. Li, R. Wang, P. Feng, M. Jiang, J. Han, S. Cao, Z. Zhang, K. Wang, K. Jiang, *ACS Energy Lett.*, **2020**, *5*, 1307-1315.

[201] F. Xiao, X. Yang, H. Wang, J. Xu, Y. Liu, D. Y. W. Yu, A. L. Rogach, *Adv. Energy Mater.* **2020**, *10*, 2000931.

[202] B. Meyer, *Chem. Rev.* **1976**, *76*, 367–388.

[203] S. Xin, L. Gu, N. Zhao, Y. Yin, L. Zhou, Y. Guo, L. Wan, *J. Am. Chem. Soc.* **2012**, *134*, 18510-18513.

[204] Y.-M. Chen, W. Liang, S. Li, F. Zou, S. M. Bhaway, Z. Qiang, M. Gao, B. D. Vogt, Y. Zhu, *J. Mater. Chem. A* **2016**, *4*, 12471.

[205] L. Hu, Y. Lu, T. Zhang, T. Huang, Y. Zhu, Y. Qian, *ACS Appl. Mater. Interfaces* **2017**, *9*, 13813-13818.

[206] R. Carter, L. Oakes, A. Douglas, N. Muralidharan, A. P. Cohn, C. L. Pint, *Nano Lett.* **2017**, *17*, 1863-1869.

[207] Y. Xu, S. Jin, H. Xu, A. Nagai, D. Jiang, *Chem. Soc. Rev.* **2013**, *42*, 8012-8031.

[208] J.-S. M. Lee, A. I. Cooper, *Chem. Rev.* **2020**, *120*, 2171–2214.

[209] Y. Li, B. Ni, X. Li, X. Wang, D. Zhang, Q. Zhao, J. Li, T. Lu, W. Mai, L. Pan, *Nano-Micro Lett.* **2019**, *11*, 60.

[210] C. Luo, Y. Zhu, O. Borodin, T. Gao, X. Fan, Y. Xu, K. Xu, C. Wang, *Adv. Funct. Mater.* **2016**, *26*, 745–752.

[211] J. W. Jeon, D.-M. Kim, J. Lee, J.-C. Lee, Y. S. Kim, K. T. Lee, B. G. Kim, *J. Mater. Chem. A* **2020**, *8*, 3580-3585.

[212] S. Lowell, J. E. Shields, M. A. Thomas, M. Thommes, in *Characterization of Porous Solids and Powders: Surface Area, Pore Size and Density*, Springer Science, New York, **2004**, 129-156.

[213] S. U. Rege, R. T. Yang, *AIChE J.* **2000**, *46*, 734-750.

[214] J. James, P. Olivier, *Carbon* **2013**, *55*, 70-80.

[215] K. T. Butler, G. S. Gautam, P. Canepa, *Npj Comput. Mater.* **2019**, *5*, 19.

[216] A. Wang, S. Kadam, H. Li, S. Shi, Y. Qi, *Npj Comput. Mater.* **2018**, *4*, 15.

[217] A. Bhowmik, I. E. Castelli, J. M. Garcia-Lastra, P. B. Jørgensen, O. Winther, T. Vegge, *Energy Storage Mater.* **2019**, *21*, 446–456.

[218] G.-L. Xu, J. Liu, R. Amine, Z. Chen, K. Amine, *ACS Energy Lett.* **2017**, *2*, 605–614.

[219] G.-L. Xu, Z. Chen, K. Amine, Selenium-Doped Sulfur Cathodes for Rechargeable Batteries, *US 10601077B2*, **2016**.

[220] B. Lee, T. Kang, H. Lee, J. Samdani, Y. Jung, C. Zhang, Z. Yu, G. Xu, L. Cheng, S. Byun, Y. Lee, K. Amine, J. Yu, *Adv. Energy Mater.* **2020**, *10*, 1903934.

[221] Z. Sun, S. Vijay, H. H. Heenen, A. Y. S. Eng, W. Tu, Y. Zhao, S. W. Koh, P. Gao, Z. W. Seh, K. Chan, H. Li, *Adv. Energy Mater.* **2020**, *10*, 1904010.

[222] N. Abidi, K. R. G. Lim, Z. W. Seh, S. N. Steinmann, *Wiley Interdiscip. Rev. Comput. Mol. Sci.* **2020**, DOI: 10.1002/wcms.1499.

[223] A. D. Handoko, F. Wei, Jenndy, B. S. Yeo, Z. W. Seh, *Nat. Catal.* **2018**, *1*, 922–934.

[224] Y. Yan, C. Cheng, L. Zhang, Y. Li, J. Lu, *Adv. Energy Mater.* **2019**, *9*, 1900148.

[225] J. Nelson, S. Misra, Y. Yang, A. Jackson, Y. Liu, H. Wang, H. Dai, J. C. Andrews, Y. Cui, M. F. Toney, *J. Am. Chem. Soc.* **2012**, *134*, 6337–6343.

[226] L. M. Bloi, J. Pampel, S. Dörfler, H. Althues, S. Kaskel, *Adv. Energy Mater.* **2020**, *10*, 1903245.

[227] M. Kohl, F. Borrmann, H. Althues, S. Kaskel, *Adv. Energy Mater.* **2016**, *6*, 1502185.

[228] M. Liu, J. Zhang, S. Guo, B. Wang, Y. Shen, X. Ai, H. Yang, J. Qian, *ACS Appl. Mater. Interfaces* **2020**, *12*, 17620–17627.

[229] X. Chen, Y. Zheng, W. Liu, C. Zhang, S. Li, J. Li, *Nanoscale* **2019**, *11*, 22196-22205.

[230] H. Au, H. Alptekin, A. C. S. Jensen, E. Olsson, C. A. O'Keefe, T. Smith, M. Crespo-Ribadeneyra, T. F. Headen, C. P. Grey, Q. Cai, A. J. Drew, M.-M. Titirici, *Energy Environ.*

*Sci.* **2020**, *13*, 3469-3479.

[231] Z.-L. Xu, G. Yoon, K.-Y. Park, H. Park, O. Tamwattana, S. J. Kim, W. M. Seong, K. Kang, *Nat. Commun.* **2019**, *10*, 2598.

[232] I. Hasa, S. Mariyappan, D. Saurel, P. Adelhelm, A. Y. Koposov, C. Masquelier, L. Croguennec, M. Casas-Cabanas, *J. Power Sources* **2021**, *482*, 228872.

[233] Battery500: Progress Update, May 19, 2020. Office of Energy Efficiency & Renewable Energy. United States Department of Energy. https://www.energy.gov/eere/articles/battery500-progress-update, accessed: May, **2020**.

[234] C. Ye, D. Chao, J. Shan, H.Li, K. Davey, S.-Z. Qiao, *Matter* **2020**, *2*, 323–344,

[235] P. Kurzweil, J. Garche, in *Lead-Acid Batteries for Future Automobiles*, Chapter 2, (Eds: J. Garche, E. Karden, P. T. Moseley, D. A. J. Rand), Elsevier, Amsterdam, **2017**, pages 27-96.

[236] E. Cha, M. Patel, S. Bhoyate, V. Prasad, W. Choi, *Nanoscale Horiz.* **2020**, *5*, 808-831.

[237] P. Vanýsek, in *CRC Handbook of Chemistry and Physics*, 92nd ed., (Eds. W. M. Haynes and D. R. Lide), CRC Press, Boca Raton, U.S.A., **2011**, pages 5-80 – 5-89.

[238] J. Pampel, S. Dorfler, H. Althues, S. Kaskel, *Energy Storage Mater.* **2019**, *21*, 41–49.

[239] A. Kumar, A. Ghosh, A. Roy, M. R. Panda, M. Forsyth, D. MacFarlane, S. Mitra, *Energy Storage Mater.* **2019**, *20*, 196-202.

[240] M. Rana, S. A. Ahad, M. Li, B. Luo, L. Wang, I. Gentle, R. Knibbe, *Energy Storage Mater.* **2019**, *18*, 289-310.

[241] S. Jiang, L. Jin, H. Hou, L. Zhang, *Polymer-Based Nanocomposites with High Dielectric Permittivity, in Polymer-Based Multifunctional Nanocomposites and Their Applications*, ch. 8, (Eds: K. Song, C. Liu and J. Z. Guo), Elsevier, Amsterdam, **2019**, pp. 201–243.

[242] Z. W. Seh, Q. Zhang, W. Li, G. Zheng, H. Yao, Y. Cui, *Chem. Sci.* **2013**, *4*, 3673.

[243] W. Chen, T. Lei, T. Qian, W. Lv, W. He, C. Wu, X. Liu, J. Liu, B. Chen, C. Yan, J. Xiong, *Adv. Energy Mater.* **2018**, *8*, 1702889.

[244] S. A. Paul, A. Nelson, D. W. Dees, *J. Power Sources* **2016**, *326*, 490-497.

[245] J. B. Dunn, L. Gaines, J. C. Kelly, C. James, K. G. Gallagher, *Energy Environ. Sci.* **2015**, *8*, 158-168.

[246] X. Shen, Y. Li, T. Qian, J. Liu, J. Zhou, C. Yan, J. B. Goodenough, *Nat. Commun.* **2019**, *10*, 900.

[247] S. Wu, Y. Qiao, K. Jiang, Y. He, S. Guo, H. Zhou, *Adv. Funct. Mater.* **2018**, *28*, 1706374.

[248] A. M. Russell, K. L. Lee, *Structure–Property Relations in Nonferrous Metals*, John Wiley & Sons, Hoboken, New Jersey, **2005**, 503.

[249] S. Amara, J. Toulc'Hoat, L. Timperman, A. Biller, H. Galiano, C. Marcel, M. Ledigabel, M. Anouti, *ChemPhysChem* **2019**, *20*, 581-594.

[250] S. Komaba, T. Hasegawa, M. Dahbi, K. Kubota, *Electrochem. Commun.* **2015**, *60*, 172-175.

[251] J. Ding, H. Zhang, W. Fan, C. Zhong, W. Hu, D. Mitlin, *Adv. Mater.* **2020**, *32*, 1908007.

[252] Q. Zhao, Y. Hu, K. Zhang, J. Chen, *Inorg. Chem.* **2014**, *53*, 9000-9005.

[253] N.-C. Lai, G. Cong, Y.-C. Lu, *J. Mater. Chem. A* **2019**, *7*, 20584.

[254] J. Y. Hwang, H. M. Kim, C. S. Yoon, Y. K. Sun, *ACS Energy Lett.* **2018**, *3*, 540−541.

[255] X. Yu, A. Manthiram, *Energy Storage Mater.* **2018**, *15*, 368–373.

[256] P. Xiong, X. Han, X. Zhao, P. Bai, Y. Liu, J. Sun, Y. Xu, *ACS Nano* **2019**, *13*, 2536-2543.

[257] Y. Liu, W. Wang, J. Wang, Y. Zhang, Y. Zhu, Y. Chen, L. Fu, Y. Wu. *Chem. Commun.* **2018**, *54*, 2288.

[258] J.-Y. Hwang, H. M. Kim, Y.-K. Sun, *J. Mater. Chem. A* **2018**, *6*, 14587.

[259] A. Magasinski, B. Zdyrko, I. Kovalenko, B. Hertzberg, R. Burtovyy, C. Huebner, T. Fuller, I. Luzinov, G. Yushin, *ACS Appl. Mater. Interfaces* **2010**, *2*, 3004-3010

[260] G. Xu, Q. Yan, A. Kushima, X. Zhang, J. Pan, J. Li, *Nano Energy* **2017**, *31*, 568-574.

[261] H. M. Kim, J.-Y. Hwang, D. Aurbach, Y.-K. Sun, *J. Phys. Chem. Lett.* **2017**, *8*, 5331-5337.

[262] Y. Li, L. Zhang, S. Liu, X. Wang, D. Xie, X. Xia, C. Gu, J. Tu, *Nano Energy* **2019**, *62*, 367.

[263] P. Liu, Y. Wang, Q. Gu, J. Nanda, J. Watt, D. Mitlin, *Adv. Mater.* **2020**, *32*, 1906735.

[264] L. Qin, Y. Lei, H. Wang, J. Dong, Y. Wu, D. Zhai, F. Kang, Y. Tao, Q. H. Yang, *Adv. Energy Mater.* **2019**, *9*, 1901427.

[265] X. Tang, D. Zhou, Peng Li, X. Guo, B. Sun, H. Liu, K. Yan, Y. Gogotsi, G. Wang, *Adv. Mater.* **2020**, *32*, 1906739.

[266] F. Xie, L. Zhang, B. Chen, D. Chao, Q. Gu, B. Johannessen, M. Jaroniec, S. Qiao, *Matter* **2019**, *1*, 1681-1693.

[267] J. Zheng, Y. Yang, X. Fan, G. Ji, X. Ji, H. Wang, S. Hou, M. Zachariah, C. Wang, *Energy Environ. Sci.* **2019**, *12*, 615-623.

[268] W. Zhang, J. Mao, S. Li, Z. Chen, Z. Guo, *J. Am. Chem. Soc.* **2017**, *139*, 3316–3319.

[269] Q. Yang, Y. Ding, G. He, *Chem. Commun.* **2020**, *56*, 3512-3515.

[270] L. Xue, H. Gao, W. Zhou, S. Xin, K. Park, Y. Li, J. B. Goodenough, *Adv. Mater.* **2016**, *28*, 9608–9612.

[271] L. Qin, W. Yang, W. Lv, L. Liu, Y. Lei, W. Yu, F. Kang, J.-K. Kim, D. Zhai, Q.-H. Yang, *Chem. Commun.* **2018**, *54*, 8032—8035.

[272] Y. Zhang, J. Lou, Y. Shuai, K. Chen, X. He, Y. Wang, N. Li, Z. Zhang, F. Gan, *Mater. Lett.* **2019**, *242*, 5–8.

[273] F. Ding, W. Xu, G. Graff, J. Zhang, M. Sushko, X. Chen, Y. Shao, M. Engelhard, Z. Nie, J. Xiao, X. Liu, P. Sushko, J. Liu, J. Zhang, *J. Am. Chem. Soc.* **2013**, *135*, 4450-4456.

[274] H. Che, J. Liu, H. Wang, X. Wang, S.S. Zhang, X.-Z. Liao, Z.-F. Ma, *Electrochem. Commun.* **2017**, *83*, 20–23.

[275] Q. Zou, Z. Liang, G.-Y. Du, C.-Y. Liu, E. Y. Li, Y.-C. Lu, *J. Am. Chem. Soc.* **2018**, *140*, 10740−10748.

**Table 1.** Fundamental materials challenges and the corresponding critical issues in Na-S batteries.

| | Fundamental Materials Challenges | Critical Issues | Strategies for Mitigation (Section Numbers) |
|---|---|---|---|
| **S cathode** | **1.** Complicated phase transitions of intermediate discharge/charge products (Na-polysulfides) | Poorly understood electrochemical reaction mechanisms | • *In situ* and *in operando* characterization of sulfur hosts (3.1)<br>• First principle calculations coupled with *in operando* testing as an iterative process (4.2) |
| | **2.** Dissolution of long-chain polysulfides into electrolyte leading to shuttle effect | Loss of active materials;<br>Rapid capacity decay;<br>Low Coulombic efficiency (CE) | • Polysulfide adsorbents and electrocatalysts (3.1.1)<br>• Hermetic encapsulation of active species (3.1.2)<br>• Solid-solid conversion reactions employing insoluble sulfur species (3.2) |
| | **3.** Large volume expansion (~160% change) upon full discharge from S to $Na_2S$ | Cathode degradation;<br>Electrode pulverization | • Encapsulation of $Na_2S$ (3.1.2)<br>• Polar binders to improve structural integrity (3.2.1, 4.3.2, 4.4.1)<br>• Pre-sodiated cathodes (4.2.3) |
| | **4.** Low ionic/electronic conductivity of both S and discharge product $Na_2S$ | Slow kinetics of Na-S reaction;<br>Poor rate capability | • Electrocatalytic host structures (3.1.1)<br>• Conductive composites and sulfur hosts (3.2, 4.2.2)<br>• Se, Te-doping (3.2.1) |
| **Na anode** | **5.** Unstable solid electrolyte interphase (SEI) formation on Na anode surface | Low CE;<br>Anode degradation | • Choice of electrolyte salts, and highly concentrated systems (2.1.1, 2.1.2)<br>• Intrinsic interphase formation (2.2.2)<br>• Extrinsic interphase engineering (2.2.3) |
| | **6.** Diffusion of dissolved polysulfides to Na anode causing side reactions | | • Gel polymer and solid-state electrolytes as physical barriers to polysulfide shuttling (2.1.3, 3.1.3, 3.1.5)<br>• Ion-selective membranes (3.1.4) |
| | **7.** Non-uniform deposition of Na resulting in dendrite formation | Short-circuit;<br>Low CE | • Alloying electrolyte additives or artificial anode interphases (2.2.2, 2.2.3)<br>• Eutectic liquid anodes (4.4.2)<br>• Self-healing $Rb^+$, $Cs^+$ electrolyte additives (4.4.3) |

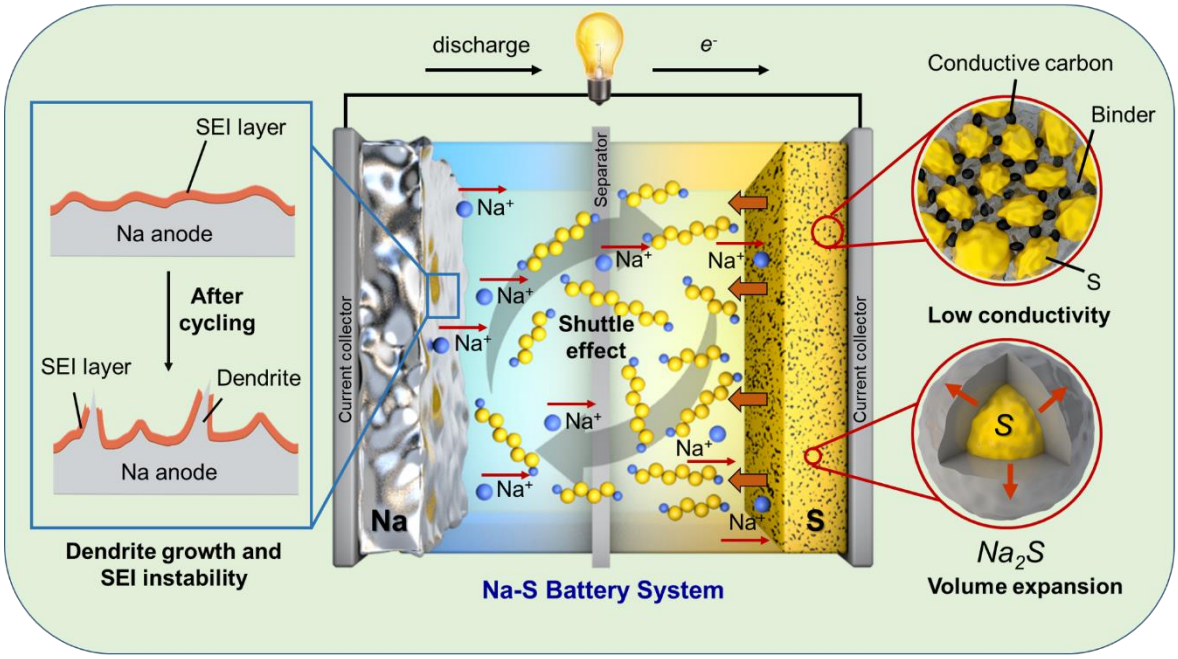


**Figure 1.** Schematic representation of a room-temperature sodium-sulfur cell, illustrating practical challenges such as polysulfide crossover and shuttling in the electrolyte. Enlarged diagrams display issues at the microscopic level, such as dendritic growth and unstable solid electrolyte interphases at the sodium anode, volumetric changes and low conductivity at the sulfur-based cathode.

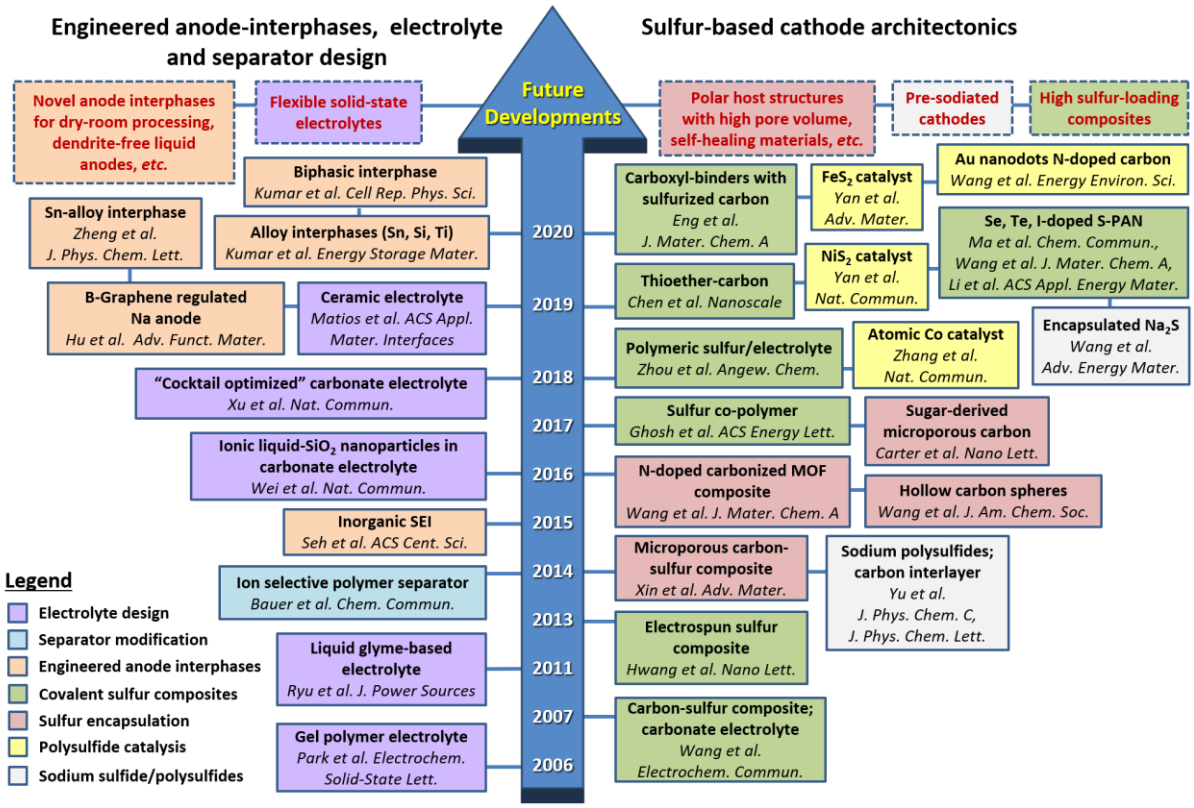


**Figure 2.** Overview of room-temperature sodium-sulfur battery development from 2006 to the present, highlighting seminal advancements in anode interphases, electrolyte design, or sulfur-based composites. Prospective future strategies towards realizing practical high energy density systems are summarized in boxes with dashed outlines.

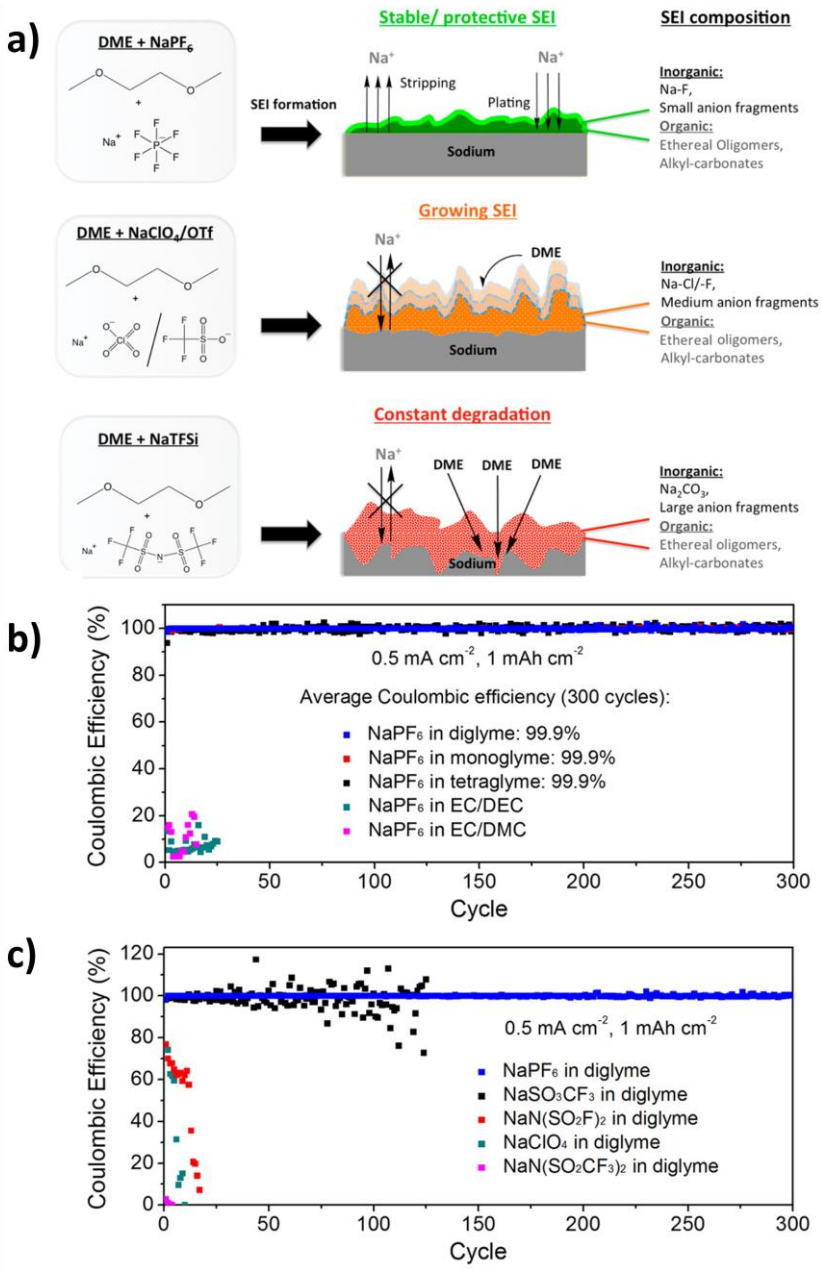


**Figure 3.** (a) Schematic illustration of the deposition behavior in the presence of various anions. Reproduced under the terms of the CC-BY license.[35] Copyright 2017, American Chemical Society. (b,c) Coulombic efficiencies of Na metal deposition/dissolution in 1 M $NaPF_6$ in various electrolyte solvents and, 1 M of various electrolyte salts in diglyme, respectively. Reproduced with permission.[26] Copyright 2015, American Chemical Society.

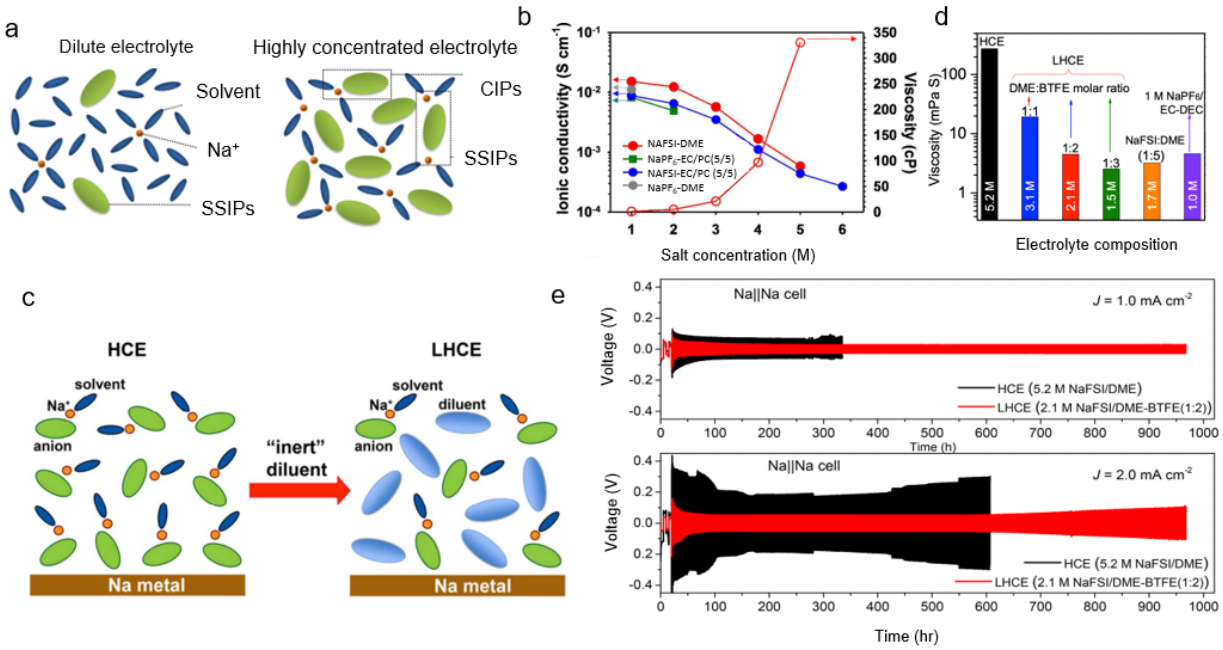


**Figure 4.** (a) Schematic illustration of the microscopic view for a dilute and highly concentrated electrolyte, demonstrating solvent separated ion-pairs (SSIPs) and cation/contact ion-pairs (CIPs). Adapted with permission.[40] Copyright 2014, American Chemical Society. (b) Ionic conductivities of NaFSI-DME, $NaPF_6$-EC/PC (5/5), NaFSI-EC/PC, $NaPF_6$-DME, and viscosity of NaFSI-DME at varying salt concentrations and room temperature. Reproduced with permission.[46] Copyright 2017, American Chemical Society. (c) Schematic diagram illustrating the dilution of a high-concentration electrolyte (HCE) to a localized high-concentration electrolyte (LHCE). (d) Viscosity comparison of dilute electrolyte, HCE, and LHCEs at varying NaFSI salt concentrations. (e) Long-term strip/plating of symmetric Na//Na cells with HCE (5.2 M NaFSI/DME) and LHCE (2.1 M NaFSI/DME-BTFE (1:2)) at 1.0 mA $cm^{-2}$ (upper panel) and (b) 2.0 mA $cm^{-2}$ (lower panel), after two initial cycles at 0.2 mA $cm^{-2}$. Reproduced with permission.[51] Copyright 2018, American Chemical Society.

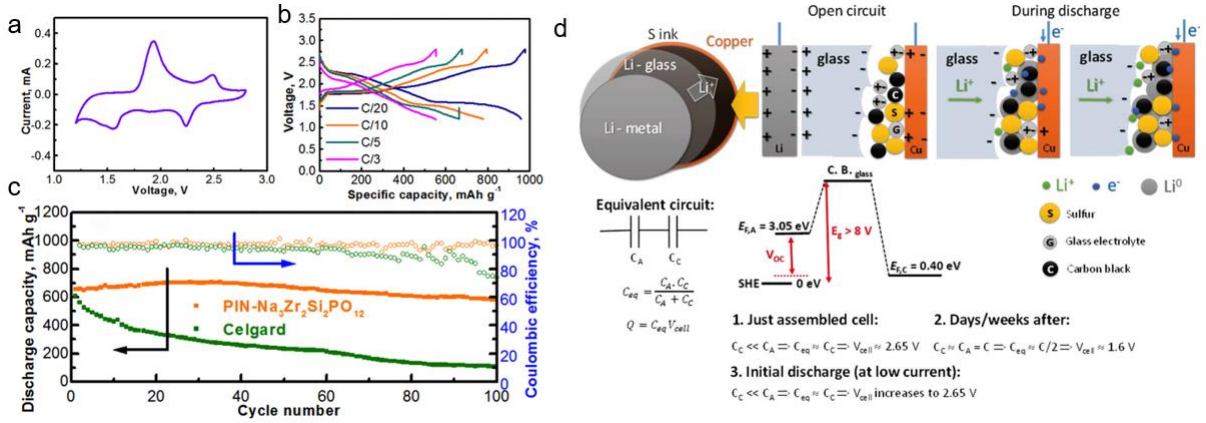


**Figure 5.** (a) Cyclic voltammograms of Na/PIN-$Na_3Zr_2Si_2PO_{12}$/CNF/S cell at a scan rate of 0.1 mV $s^{-1}$. (b) Charge/discharge curves of Na/PIN-$Na_3Zr_2Si_2PO_{12}$/CNF/S cells at various C-rates. (c) Capacities and the Coulombic efficiencies a function of cycle at a cycling rate of 0.2 C. Reproduced with permission.[80] Copyright 2019, Elsevier. (d) Schematic illustration of a plating cathode: the plating process on discharge with a redox center, the electrode energies, and the charging capacitances at electrode/electrolyte interfaces. Reproduced with permission.[82] Copyright 2017, The Royal Society of Chemistry.

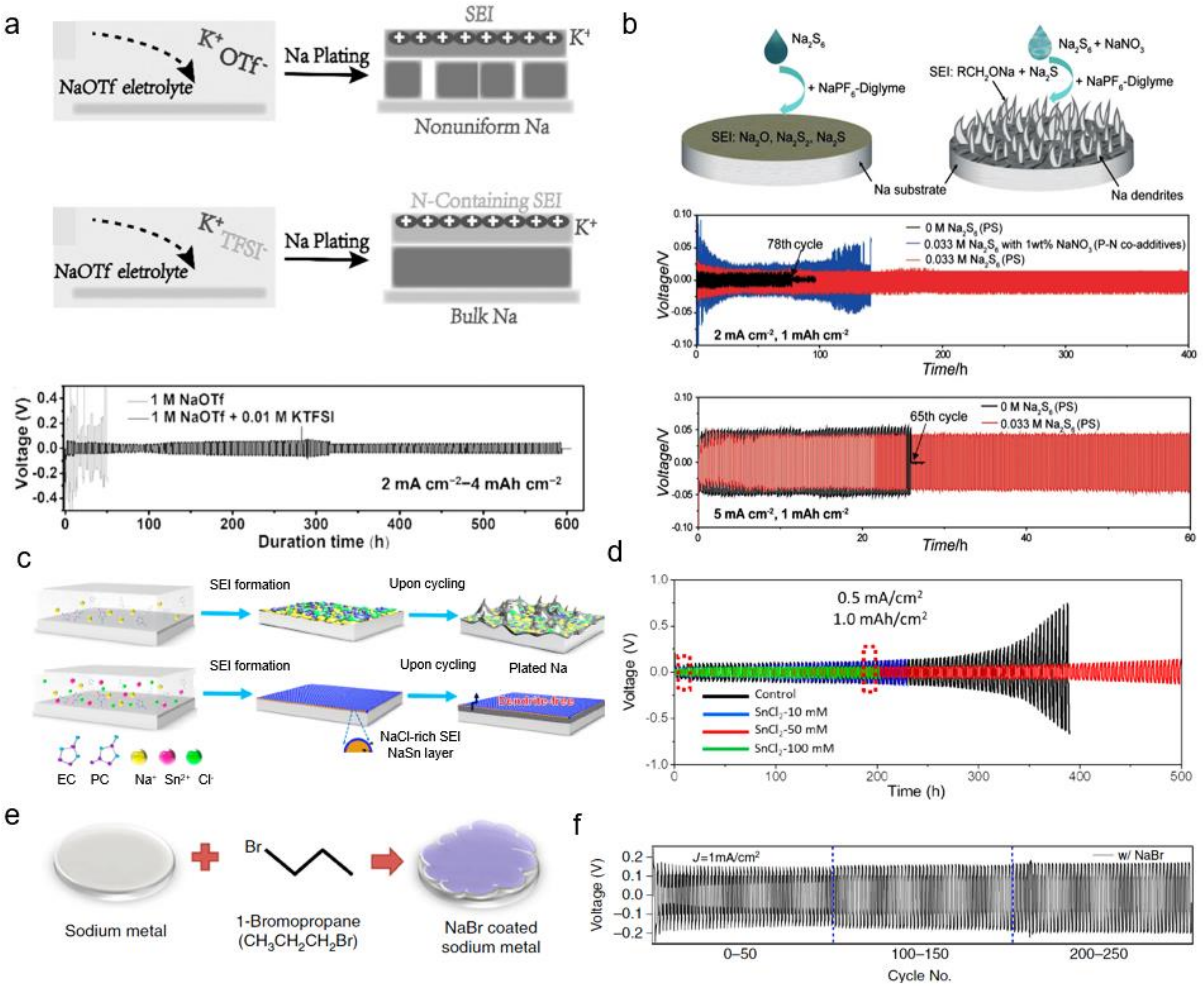


**Figure 6.** (a) Schematic illustration of the electrostatic absorption of $K^+$ ion, and effect of $TFSI^-$ anion on the SEI composition, and stripping/plating stability of Na metal anode in the presence of the $TFSI^-$ anion. Reproduced with permission.[99] Copyright 2018, Wiley-VCH. (b) Depiction of the process steps involved in the development of intrinsic interphase, and stripping/plating stability of Na anode with and without interphase. Reproduced with permission.[101] Copyright 2018, Wiley-VCH. (c) Illustration of the Na metal anode with and without alloy interphase (Na-Sn), (d) stripping/plating stability of Na metal anode with and without alloy interphase. Reproduced with permission.[102] Copyright 2019, American Chemical Society. (e) Illustration of the process steps to develop artificial interphase, and (f) stability of Na metal anode with and without NaBr interphase, at 1 mA $cm^{-2}$ current density. Reproduced under the terms of the CC-BY license.[107] Copyright 2017, Springer Nature.

**Table 2.** Performance comparison of various additives to facilitate the formation of intrinsic interphase.

| Additive | Nature of additive | Cycle life (Na//Na cell) (hours) | Current density | Overpotential (mV) | Ref. |
|---|---|---|---|---|---|
| 3% FEC | reduction | 600 | 50 μA $cm^{-2}$ | 200 | 96 |
| Li salt | absorption | 500 | 2 mA $cm^{-2}$ | 45 | 98 |
| KTFSI | absorption | 600 | 0.5 mA $cm^{-2}$ | 14 | 99 |
| $Na_2S_6$ | reduction | 400 | 2 mA $cm^{-2}$ | 50 | 101 |
| $SnCl_2$ | reduction-alloy | 600 | 0.5 mA $cm^{-2}$ | 200 | 102 |
| $InI_3$ | reduction-alloy | 900 | 0.1 mA $cm^{-2}$ | 250 | 103 |

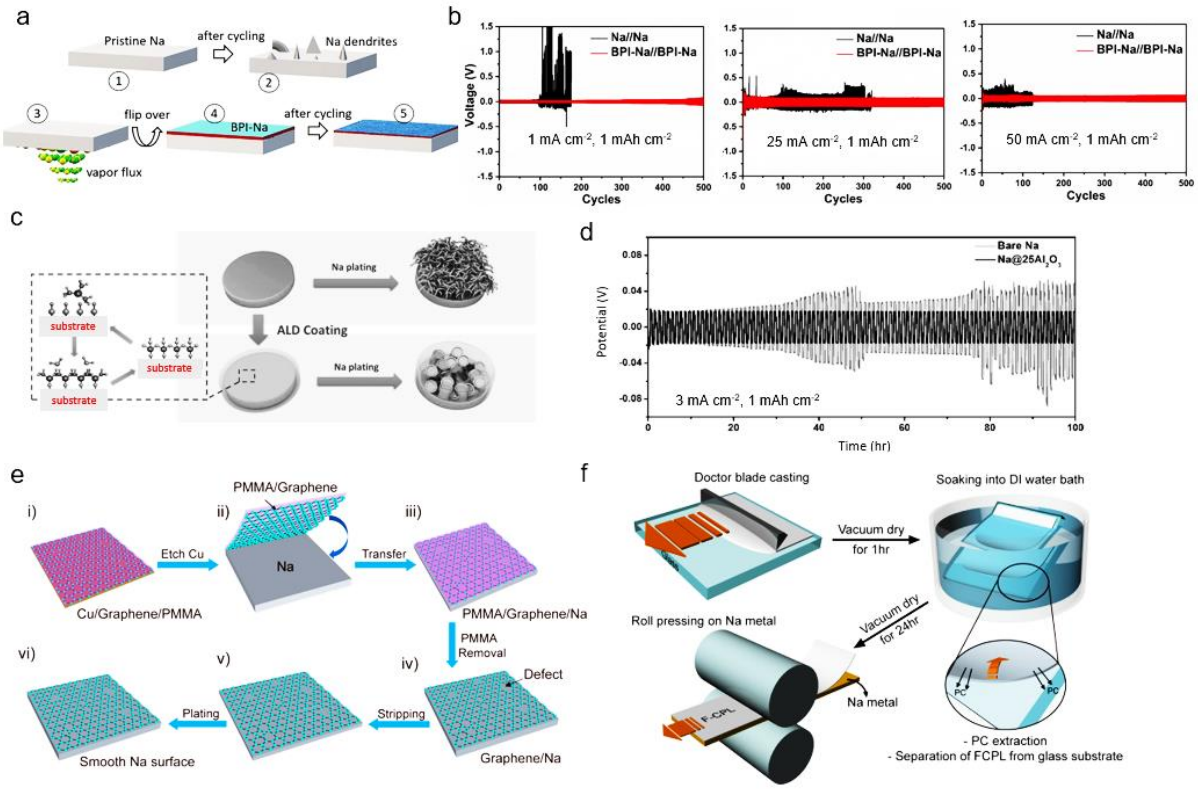


**Figure 7.** (a) Schematic illustration of the process steps involved in the development of the biphasic interphase, (b) stripping/plating stability of Na metal anode with and without biphasic interphase, Reproduced under the terms of the CC-BY-NC-ND license.[89] Copyright 2020, The Authors. (c) Pictorial depiction of atomic layer deposition of $Al_2O_3$ interphase, and its effectiveness in preserving surface integrity, and (d) stability of the Na metal anode with and without $Al_2O_3$ interphase. Reproduced with permission.[110] Copyright 2017, Wiley-VCH. Illustration of the steps involved in solid-solid approach for (e) multi-layer graphene/Na metal and (f) polymer layer/Na metal electrode. Reproduced with permission.[115,117] Copyright 2017, American Chemical Society.

**Table 3.** Performance comparison of various strategies to design artificial or extrinsic interphase.

| **Interphase materials** | **Fabrication route** | **Cycle life (h) (Na//Na cell)** | **Current density** | **Overpotential (mV)** | **Ref.** |
|---|---|---|---|---|---|
| NaBr | drop casting (solid-liquid) | 500 | 1 mA $cm^{-2}$ | 200 | 107 |
| Na-Sn | drop-casting (solid-liquid) | 1000 | 0.5 mA $cm^{-2}$ | 400 | 108 |
| Polymeric (DAIM) | drop casting (solid-liquid) | 50 | 1 mA $cm^{-2}$ | 80 | 109 |
| $Na_2S_6$ | drop casting (solid-liquid) | 400 | 2 mA $cm^{-2}$ | 50 | 101 |
| $NaNH_2$-NaOH | vapor reaction (solid-vapor) | 1000 | 1 mA $cm^{-2}$ | 70 | 89 |
| Na-Sn | vapor reaction (solid-vapor) | 650 | 3 mA $cm^{-2}$ | 100 | 105 |
| $Al_2O_3$ | atomic layer deposition (solid-gas) | 500 | 3 mA $cm^{-2}$ | 400 | 110 |
| $Al_2O_3$ | plasma enhanced atomic layer deposition (solid-gas) | 450 | 0.25 mA $cm^{-2}$ | 200 | 111 |
| Alucone | molecular layer deposition (solid-gas) | 140 | 3 mA $cm^{-2}$ | 800 | 112 |
| multilayer graphene | physical adsorption (solid-solid) | 600 | 0.25 mA $cm^{-2}$ | 500 | 115 |
| $MoS_2$ flakes | physical adsorption (solid-solid) | 150 | 0.2 mA $cm^{-2}$ | 25 | 116 |
| PVDF-HFP-$Al_2O_3$ | physical adsorption (solid-solid) | 550 | 0.5 mA $cm^{-2}$ | 500 | 117 |

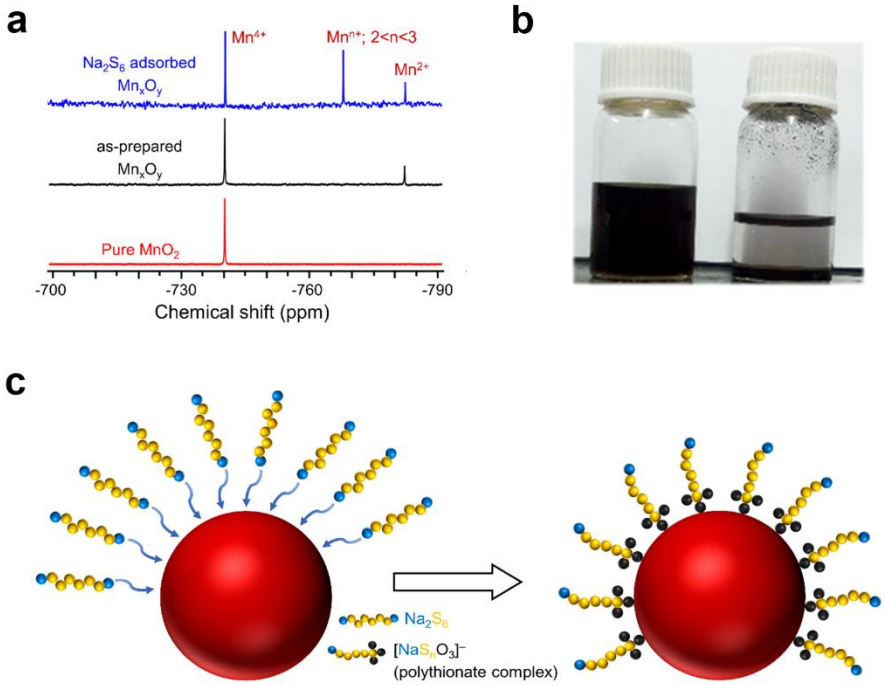


**Figure 8.** Demonstration of polysulfide adsorption ability of $Mn_xO_y$ and its mechanism. (a) Solid-state $^{55}$Mn NMR spectra of $Mn_xO_y$ at different states. (b) Camera images of $Na_2S_6$ solution without $Mn_xO_y$ (left bottle) and with $Mn_xO_y$ (right bottle). (c) Schematic of the $Mn_xO_y$ adsorption and possible redox reaction. $Mn_xO_y$ is reduced after interaction with $Na_2S_6$ and simultaneously $Na_2S_6$ gets oxidized to a polythionate complex. Reproduced with permission.[127] Copyright 2019, American Chemical Society.

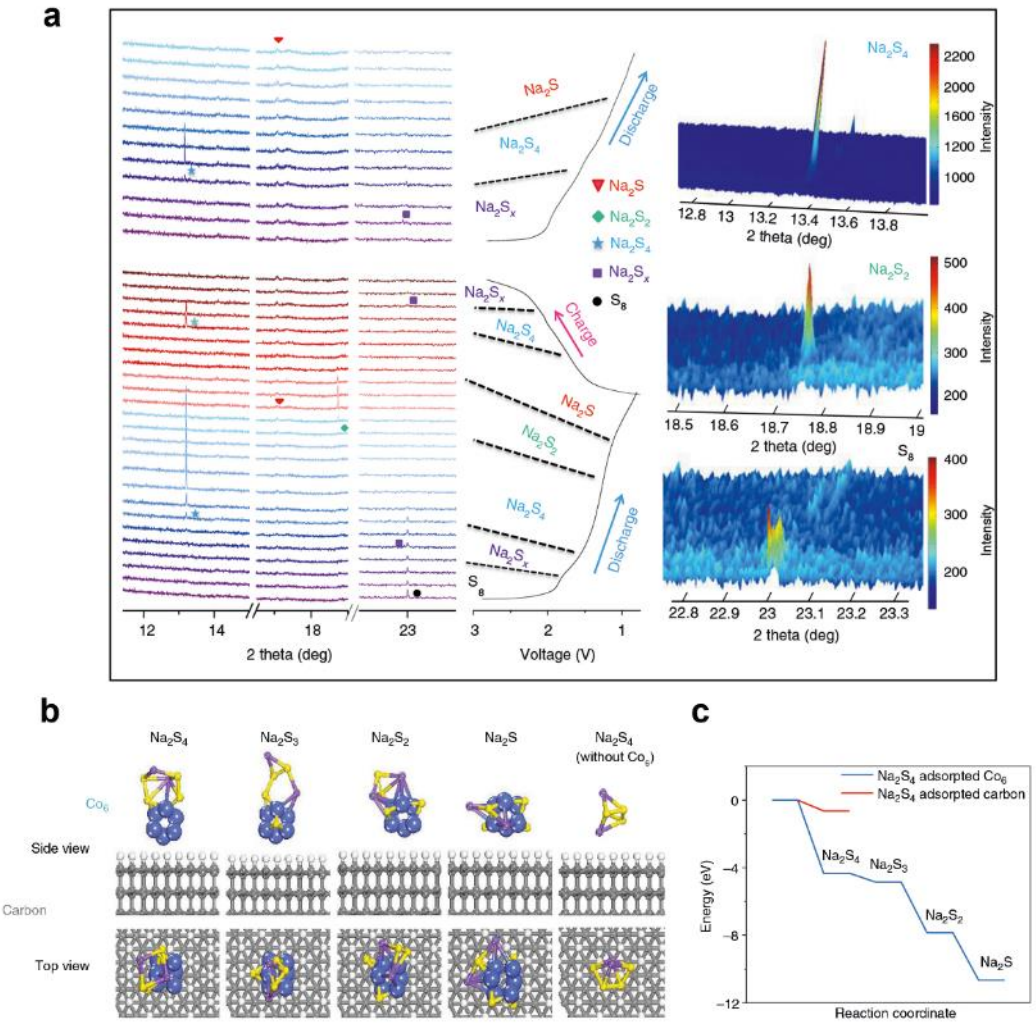


**Figure 9.** Characterization and mechanism of the electrocatalytic process. (a) In situ SXRD patterns of the RT-Na/S@$Co_n$-HC cells (left) with the initial galvanostatic charge/discharge curves (middle) at 500 mA $g^{-1}$, and contour plot of XRD patterns at selected ranges of degrees two theta (right) at 100 mA $g^{-1}$. (b) Density functional theory results for optimized structures of $Na_2S_4$ cluster on carbon-supported $Co_6$ cluster, and carbon support. (c) Energy profiles of $Na_2S_4$ adsorption on carbon-supported $Co_6$ cluster (in blue) and carbon support (in red). Reproduced under the terms of the CC-BY license.[134] Copyright 2018, Springer Nature.

**Table 4.** Comparison of the binding energy/adsorption energy of metals and metal sulfides.

| Sulfiphilic Site | Cathode Material | Binding/Adsorption Energy (eV) | | | Specific capacity at final cycle (Current density) | Cycle lifetime demonstrated | Ref. |
|---|---|---|---|---|---|---|---|
| | | $S_8$ | $Na_2S_4$ | $Na_2S_2$ | | | |
| $TiO_2$ | CSB@$TiO_2$ | - | - | - | 524.8 mAh $g^{-1}$ (1 A $g^{-1}$) | 1400 | 126 |
| $Mn_xO_y$ | rGO/S/$Mn_xO_y$@SA-PANI | - | - | - | ~320 mAh $g^{-1}$ (0.5 A $g^{-1}$) | 400 | 127 |
| $Ti_3C_2T_x$ | S-$Ti_3C_2T_x$/S composite | - | -2.88 | -1.89 | 577 mAh $g^{-1}$ (2 C) | 500 | 129 |
| Nano Cu | HSMC | - | - | - | 610 mAh $g^{-1}$ (0.03 C) | 110 | 131 |
| Atomic Co | S@Con-HC | - | -4.33 | -7.85 | 508 mAh $g^{-1}$ (100 mA $g^{-1}$) | 600 | 134 |
| Co nanoparticle | S@Co/C/rGO | - | - | - | 286.5 mAh $g^{-1}$ (5 C) | 1000 | 137 |
| Fe nanocluster | S@M-HC | - | -2.46 | -10.02 | 394 mAh $g^{-1}$ (100 mA $g^{-1}$) | 1000 | 138 |
| Cu nanocluster | | - | -1.94 | -7.76 | 263 mAh $g^{-1}$ (100 mA $g^{-1}$) | 1000 | |
| Ni nanocluster | | - | -2.93 | -7.74 | 201 mAh $g^{-1}$ (100 mA $g^{-1}$) | 1000 | |
| $FeS_2$ nanograins | $FeS_2$@NCMS/S | - | -1.46 | -2.78 | 524 mAh $g^{-1}$ (0.1 A $g^{-1}$) | 300 | 135 |
| $NiS_2$ nanocrystal | $NiS_2$@NPCTs/S | - | -0.70 | -1.60 | 401 mAh $g^{-1}$ (1 A $g^{-1}$) | 750 | 139 |
| $CoS_2$ | core-shell ZCS@S | -0.83 | -2.43 | - | 325 mAh $g^{-1}$ (0.2 A $g^{-1}$) | 500 | 140 |
| ZnS | | -0.70 | -2.14 | - | 570 mAh $g^{-1}$ (0.2 A $g^{-1}$) | 1000 | |
| Au nanodots | CN/Au/S | -1.63 | -2.59 | -3.39 | 430 mAh $g^{-1}$ (2 A $g^{-1}$) | 1000 | 141 |
| Ni-MOF-2D | S/Ni-MOF-2D | - | -2.60 | -4.00 | 347 mAh $g^{-1}$ (1 C) | 1000 | 142 |

Abbreviations: $FeS_2$@NCMS: $FeS_2$ nanograins grown in nitrogen-doped hierarchical carbon microspheres. $NiS_2$@NPCTs: $NiS_2$ nanocrystals implanted in nitrogen-doped porous carbon nanotubes. Core-shell ZCS@S: core-shell nanoarchitecture and multi-sulfiphilic cathode.

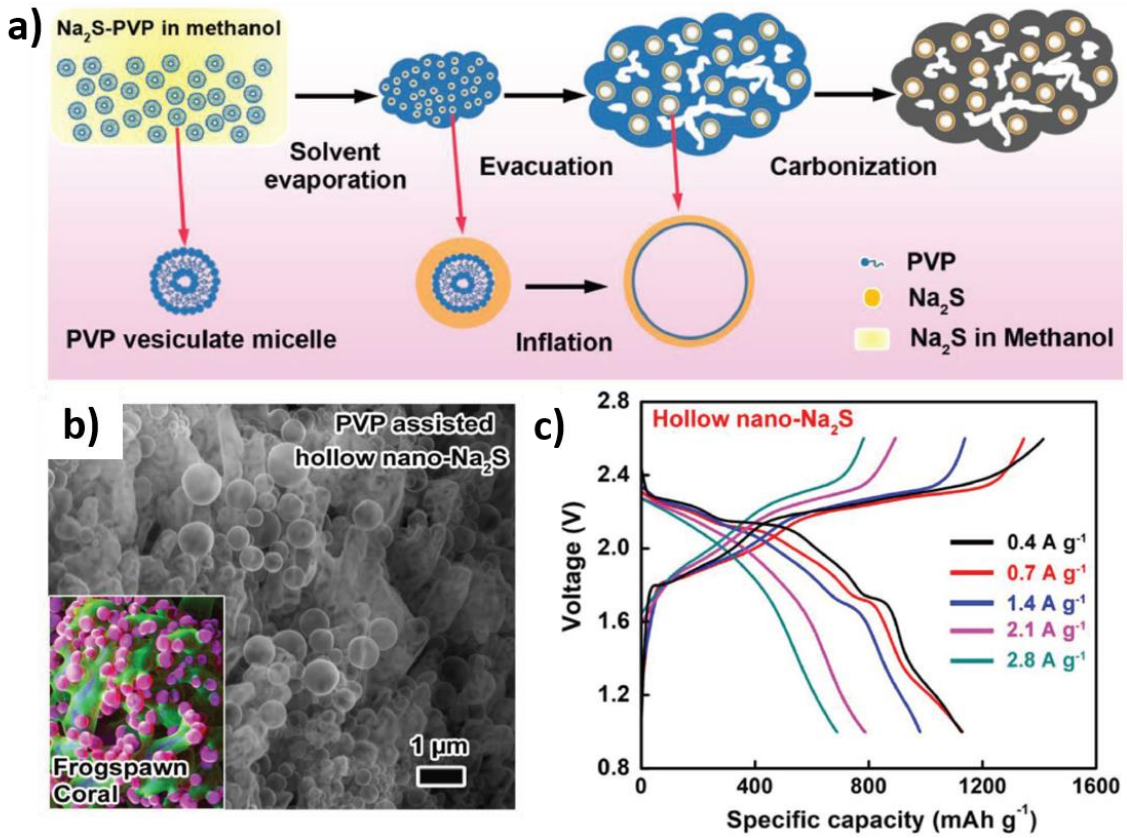


**Figure 10.** Encapsulation of active material in a carbonaceous host structure, allowing for cycling of long-chain polysulfides, without physical contact with the external liquid electrolyte. (a) Reaction schematic for the synthesis of encapsulated $Na_2S$ in hollow carbon spheres. (b) SEM image of hollow $Na_2S$ nanospheres embedded in a spongy carbon matrix. (c) Galvanostatic charge/discharge curves for hollow $Na_2S$ cathodes at varying current densities. Reproduced with permission.[144] Copyright 2019, Wiley-VCH.

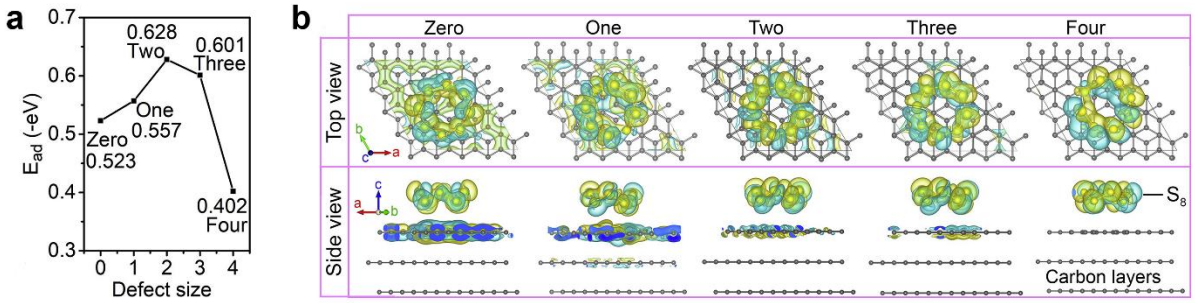


**Figure 11.** Density functional theory calculation of processed nanocarbon. (a) The adsorption energy of $S_8$ molecule adsorbed on different carbon defect site. (b) Deformation charge density at an $S_8$ molecule adsorption site of the carbon surface with different defect sizes. The graphs show top and side views of the deformation charge density. The stable models of $Na_2S$ and $Na_2S_5$ molecule adsorption on the carbon surface with or without different defects are shown. Reproduced with permission.[150] Copyright 2020, Elsevier.

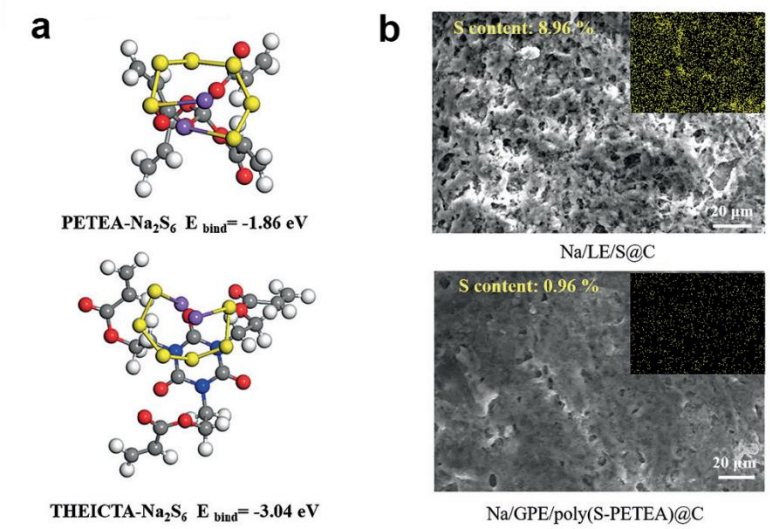


**Figure 12.** (a) Calculated binding energies of $Na_2S_6$ with PETEA and THEICTA monomers. Yellow, purple, gray, white, red and blue balls represent sulfur, sodium, carbon, hydrogen, oxygen and nitrogen atoms, respectively. (b) SEM and EDS (inset) images of Na metal anode after 100 cycles at 0.1C from Na/ LE/S@C and Na/GPE/poly(S-PETEA)@C cells. Reproduced with permission.[151] Copyright 2018, Wiley-VCH.

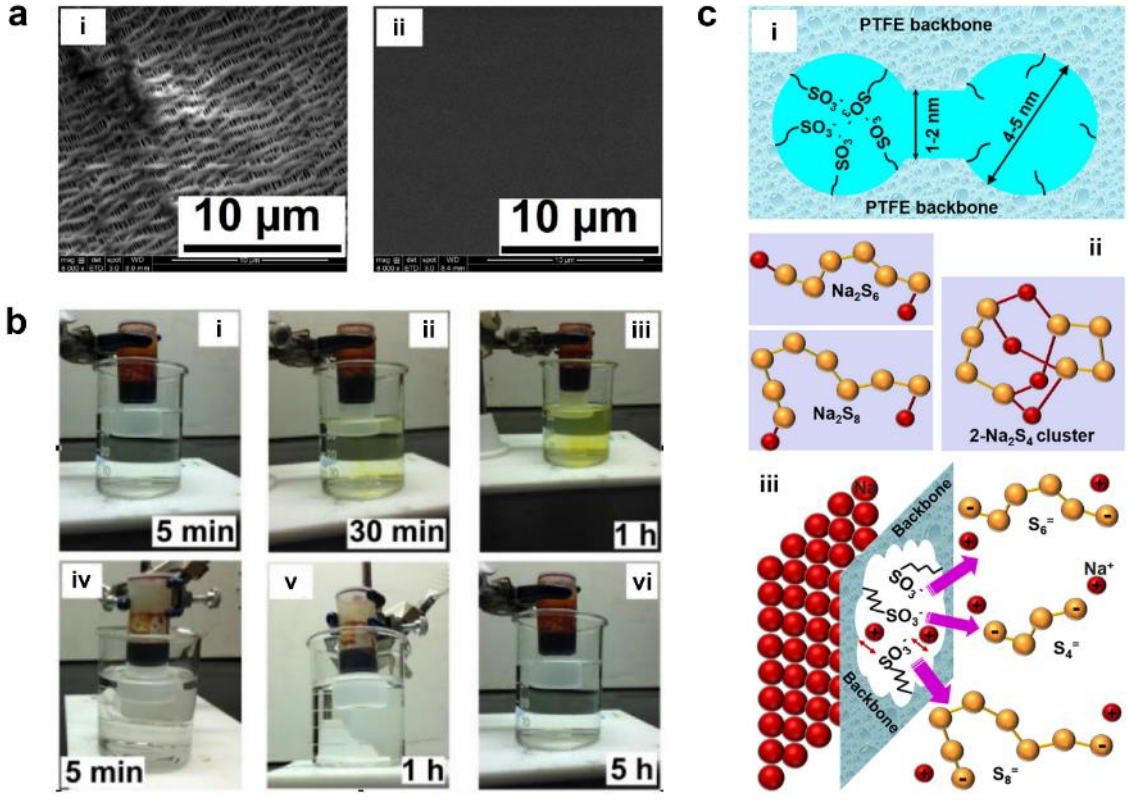


**Figure 13.** Characterization of Na-Nafion membrane. (a) SEM images of i) a porous Celgard separator and ii) a non-porous Nafion membrane. (b) Demonstration of the visual polysulfide diffusion tests. i) to iii) Polysulfide diffusion test of the Celgard separator after various resting times. iv) to vi) Polysulfide diffusion test of the sodiated Nafion membrane after various resting times. Reproduced with permission.[153] Copyright 2015, Wiley-VCH. (c) Schematics of i) Architecture of Nafion membrane. ii) Molecular schematics of monomeric $Na_2S_6$,

$Na_2S_8$, and dimer $Na_2S_4$ units. The sulfur and sodium are, respectively, represented by orange and red spheres. iii) the ionic-selectivity of the Nafion membrane by ionic interactions at the hydrophilic pores of the membrane. Reproduced with permission.[154] Copyright 2016, American Chemical Society.

**Table 5.** Performance comparison of gel polymer electrolytes, ion-selective membranes, and polymer electrolytes.

| **Electrolyte systems** | | **Specific capacity (Initial)** | **Specific capacity at final demonstrated cycle** | **Cycle lifetime demonstrated** | **Ref.** |
|---|---|---|---|---|---|
| PVDF-HFP: Tetraglyme: $NaCF_3SO_3$ | 3: 6: 1 | - | 108 mAh $g^{-1}$ | 10 | 19 |
| PVDF-HFP: Tetraglyme: $NaCF_3SO_3$ | 3: 6: 1 | 392 mAh·$g^{-1}$ | 117 mAh $g^{-1}$ | 10 | 146 |
| 1M NaTf in EC/PC: PVDF-HFP (with $SiO_2$ filler) | 4: 1 | 165 mAh·$g^{-1}$ | 21 mAh $g^{-1}$ | 8 | 147 |
| PVDF-HFP: 1M $NaPF_6$ in diglyme (with $SiO_2$ filler) | 17.2 wt% liquid | 713 mAh·$g^{-1}$ | >700 mAh $g^{-1}$ | 200 | 150 |
| Cross-linked PETEA-THEICTA: 1M NaTFSI in PC/FEC | | - | 736 mAh $g^{-1}$ | 100 | 151 |
| Na-Nafion: 1M $NaClO_4$ in tetraglyme | | - | 350 mAh $g^{-1}$ | 20 | 21 |
| Na-Nafion: 1M $NaClO_4$, 0.2M $NaNO_3$ in tetraglyme | | 750 mAh·$g^{-1}$ | 550 mAh $g^{-1}$ | 100 | 153 |
| Na-Nafion-coated activated carbon nanofiber: 1.5M $NaClO_4$, 0.2M $NaNO_3$ in tetraglyme | | 680 mAh·$g^{-1}$ | - | 100 | 154 |
| PBI: 1M NaTFSI and 0.2M $NaNO_3$ | | 837 mAh·$g^{-1}$ | - | - | 155 |
| PIN-coated $Na_3Zr_2Si_2PO_{12}$: 1M $NaClO_4$ tetraglyme | | - | 550 mAh $g^{-1}$ | 100 | 80 |
| β"-$Al_2O_3$: 1M $NaCF_3SO_3$ DOL/DME | | 475 mAh·$g^{-1}$ | 200 mAh $g^{-1}$ | 40 | 161 |
| β"-$Al_2O_3$: 1M $NaCF_3SO_3$ tetraglyme | 1.5 ul liquid | 855 mAh·$g^{-1}$ | 521 mAh $g^{-1}$ | 104 | 162 |
| PEO: $NaCF_3SO_3$ | 9: 1 | 505 mAh·$g^{-1}$ | 166 mAh $g^{-1}$ | 10 | 22 |

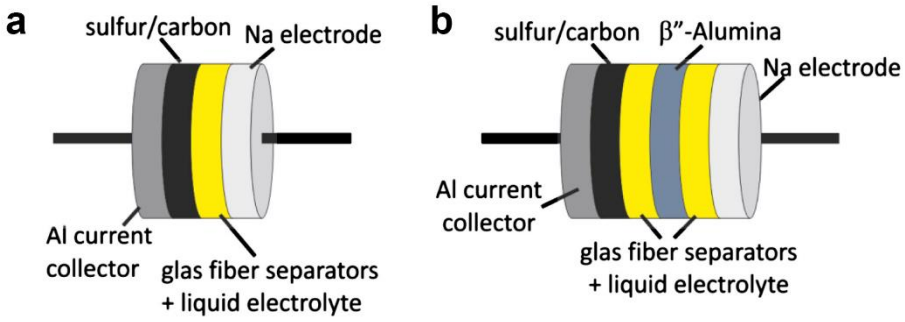


**Figure 14.** Schematics of the cell structure of NSBs with (a) liquid electrolyte; (b) beta-alumina liquid/solid electrolyte. Reproduced with permission.[161] Copyright 2013, Elsevier.

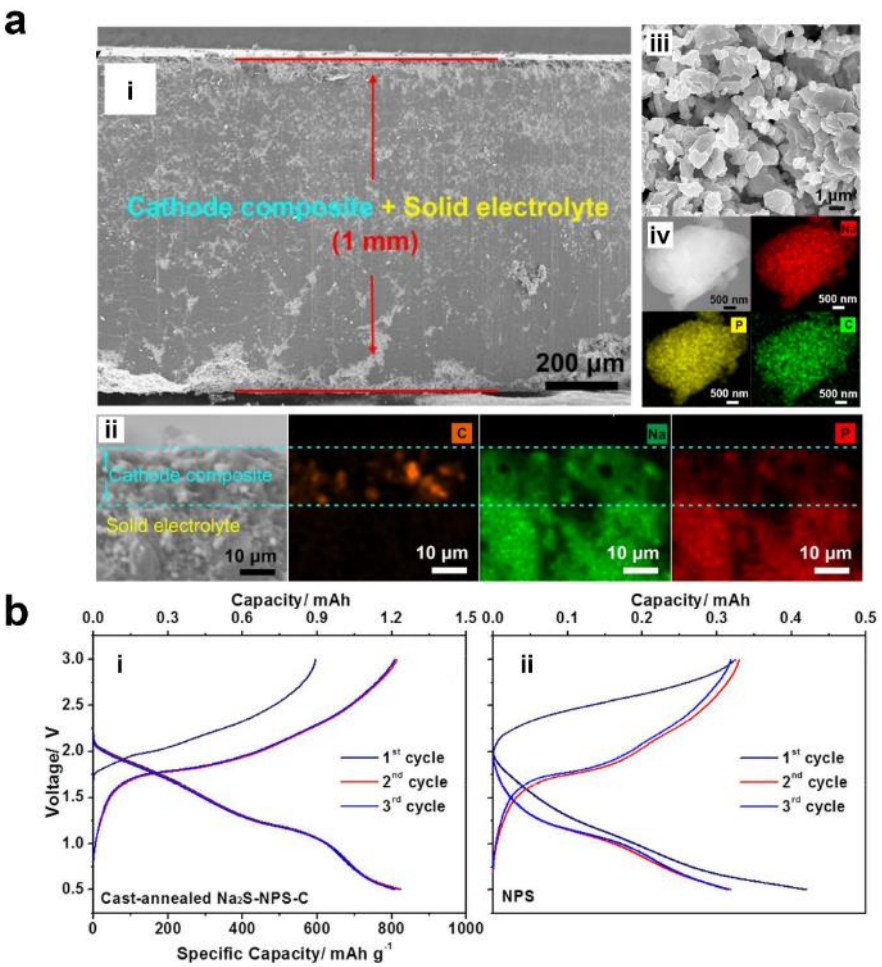


**Figure 15.** (a) (i) Cross-section SEM image of NPS-nano-$Na_2S$-C cathode composite and $Na_3PS_4$ solid electrolyte. (ii) High magnification cross-section SEM image around the cathode/electrolyte interface and the corresponding elemental mappings of C, Na, and P. (iii) SEM image of NPS. (iv) SEM image and elemental mappings of sodium, phosphorus, and carbon. Reproduced with permission.[23] Copyright 2017, American Chemical Society. (b) Electrochemical performances of (i) the cast-annealed $Na_2S$-NPS-C nanocomposite and (ii) NPS-C composite at 60 °C between 0.5 and 3 V. The upper axis shows the total capacity of the electrode, the lower on showing the specific capacity calculated based on the weight of $Na_2S$ in the electrode. Reproduced with permission.[171] Copyright 2018, American Chemical Society.

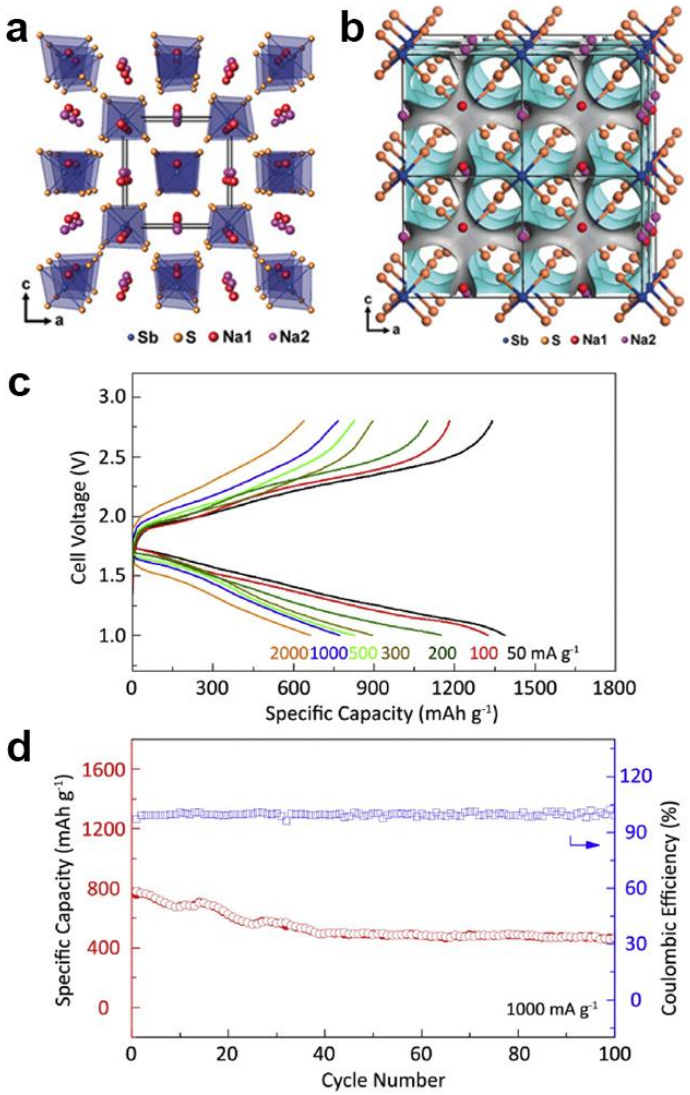


**Figure 16.** (a) Crystal structure of $Na_3SbS_4$ with the unit cell outlined. (b) 3D bond valence map isosurfaces for $Na_3SbS_4$ with an isovalue of ±0.3 v.u. Reproduced with permission.[176] Copyright 2016, Wiley-VCH. (c) Galvanostatic discharge/charge profiles under different current densities at room temperature. (d) Room temperature cycling performance at current density of 1000 mA $g^{-1}$. Reproduced with permission.[178] Copyright 2020, Elsevier.

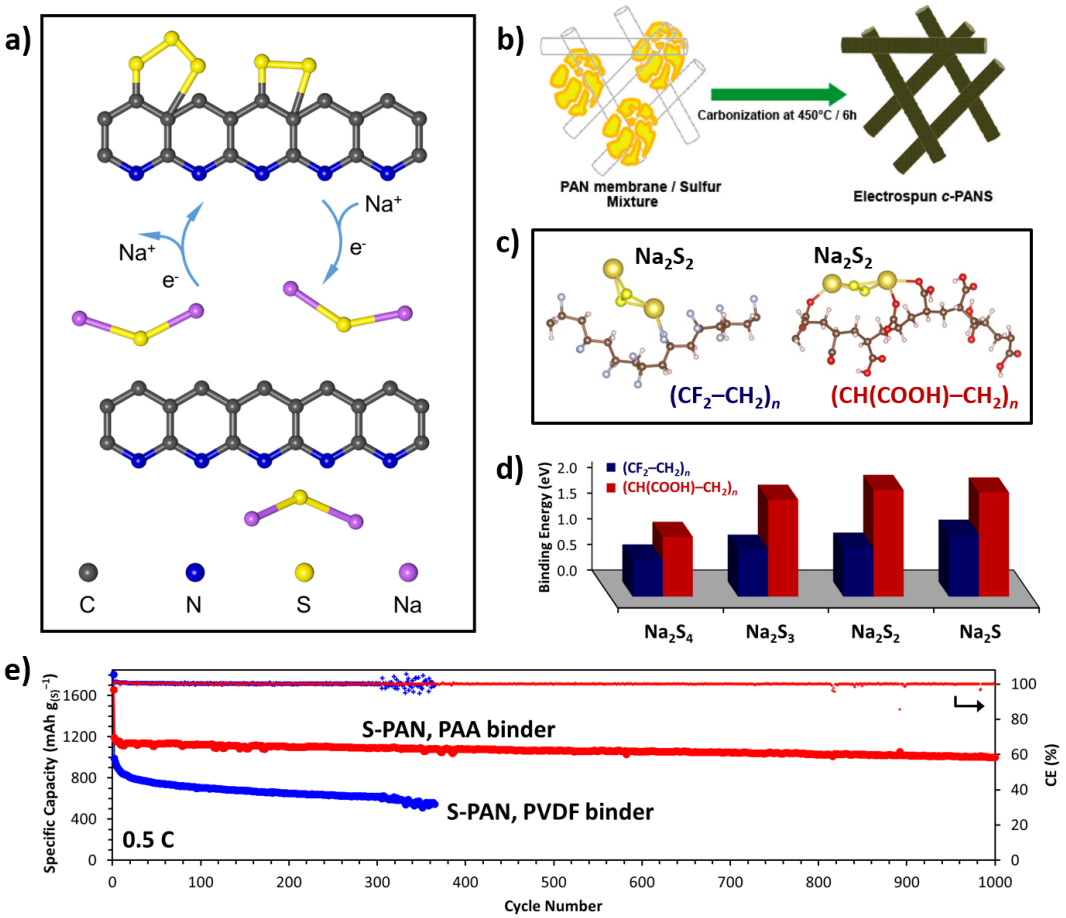


**Figure 17.** Sulfurized polyacrylonitrile (S-PAN) composites, and strategies for improving cycle life and rate performance. (a) Generalized sodiation/desodiation mechanism. Adapted with permission.[158] Copyright 2019, American Chemical Society. (b) Carbonization of electrospun PAN fibers in the presence of sulfur. Reproduced with permission.[181] Copyright 2013, American Chemical Society. (c) Optimized binding configurations of $Na_2S_2$, and (d) binding energies of short-chain polysulfides and $Na_2S$ with polyvinylidene difluoride $(CF_2–CH_2)_n$ or polyacrylic acid $(CH(COOH)–CH_2)_n$ binders, based on density functional theory calculations. (e) comparison of cycling performance for cathodes with PAA and PVDF binders. Adapted with permission.[184] Copyright 2020, The Royal Society of Chemistry.

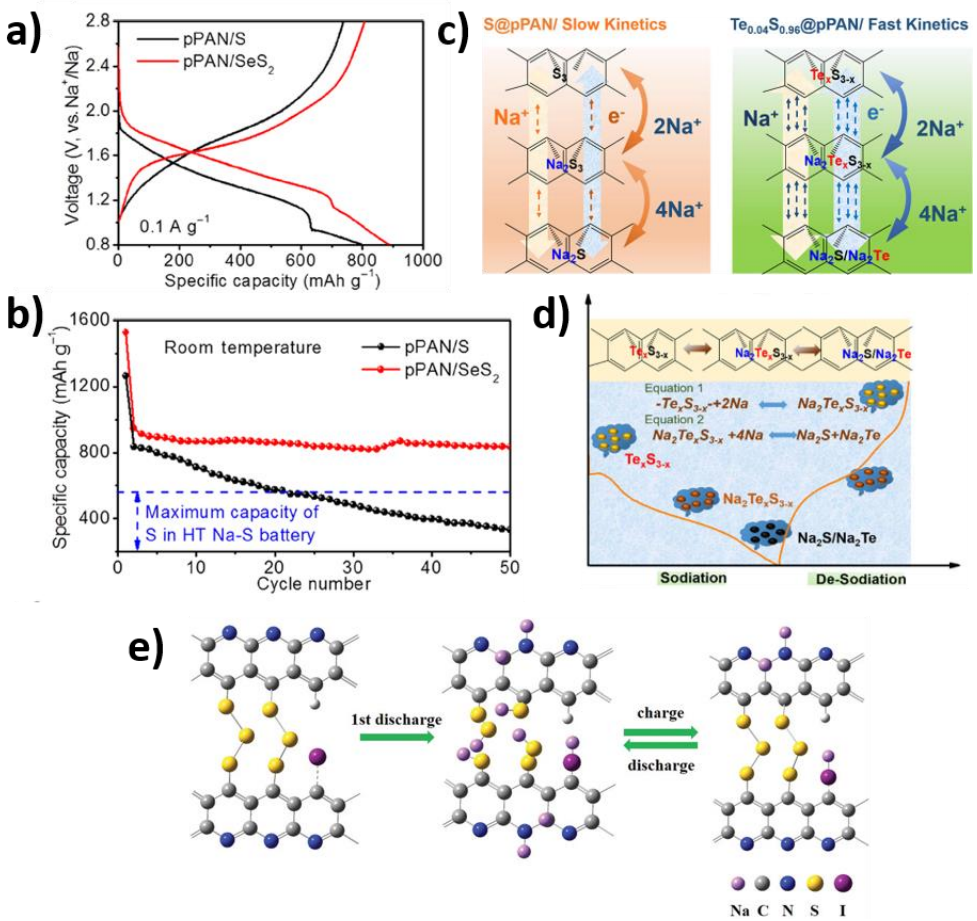


**Figure 18.** Elemental-doping of S-PAN for kinetic enhancements. (a) Comparison of galvanostatic charging curves, and (b) cycling performances for S-PAN and $SeS_2$-doped S-PAN. Reproduced under the terms of the CC-BY-NC license.[186] Copyright 2018, The American Association for the Advancement of Science. (c,d) Illustration of sodiation mechanisms for undoped and Te-doped S-PAN. Reproduced with permission.[190] Copyright 2019, American Chemical Society. (e) Proposed mechanism for iodine-participation in the sodiation of I-doped S-PAN. Reproduced with permission.[191] Copyright 2019, The Royal Society of Chemistry.

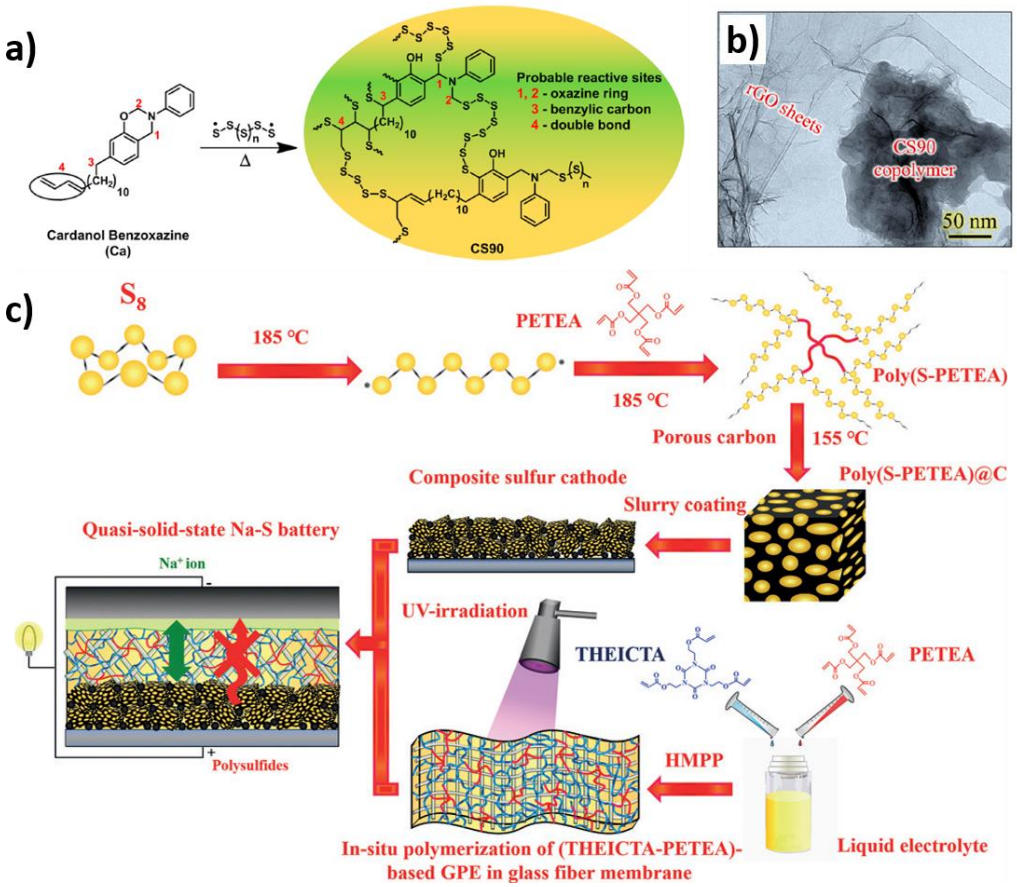


**Figure 19.** Sulfur-copolymers derived from ring opening polymerization with elemental $S_8$. (a) co-polymerization of naturally-derived benzoxazine with $S_8$ to form CS90, and (b) the CS90 co-polymer containing conductive reduced graphene oxide filler. Reproduced with permission.[197] Copyright 2017, American Chemical Society. (c) Schematic for the inverse vulcanization of elemental sulfur with poly(S-pentaerythritol tetraacrylate(PETEA)) copolymer as cathode, and its combination with an polymerized tris[2-(acryloyloxy)ethyl] isocyanurate (THEICTA) *quasi* solid-state electrolyte, initiated by *in-situ* UV-light irradiation of 2-hydroxy-2-methyl-1-phenyl-1-propanone (HMPP). Reproduced with permission.[151] Copyright 2018, Wiley-VCH.

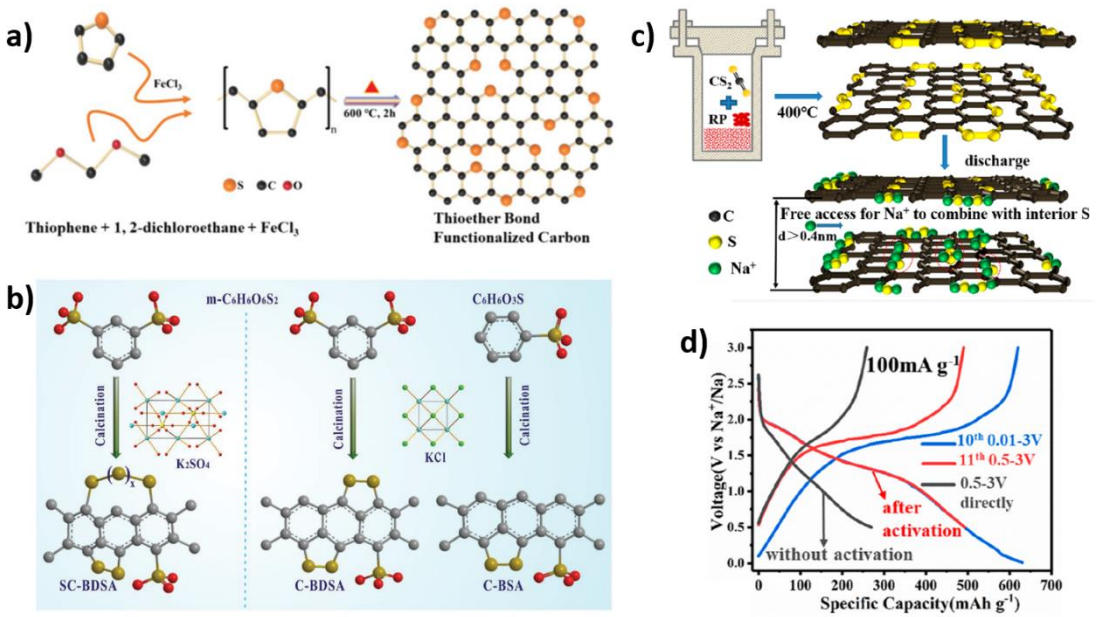


**Figure 20.** Sulfur composites from alternative organosulfur sources. (a) Friedel-Crafts polymerization of a crosslinked polymer using thiophene and dimethoxymethane, with subsequent carbonization to form thioether-functionalized carbons. Reproduced with permission.[198] Copyright 2019, The Royal Society of Chemistry. (b) Comparison of covalent-sulfur species composites formed from the calcination of benzenedisulfonic acid (BDSA), benzenesulfonic acid (BSA), and/or potassium sulfate as precursors. Reproduced with permission.[199] Copyright 2019, Wiley-VCH. (c) Solvothermal synthesis of a covalent sulfur−carbon composite from carbon disulfide precursor in the presence of red phosphorus, and (d) galvanostatic charge/discharge curves demonstrating the effect of prior electrochemical activation at low voltages of 0.01 V to 3 V. Reproduced with permission.[200] Copyright 2020, American Chemical Society.

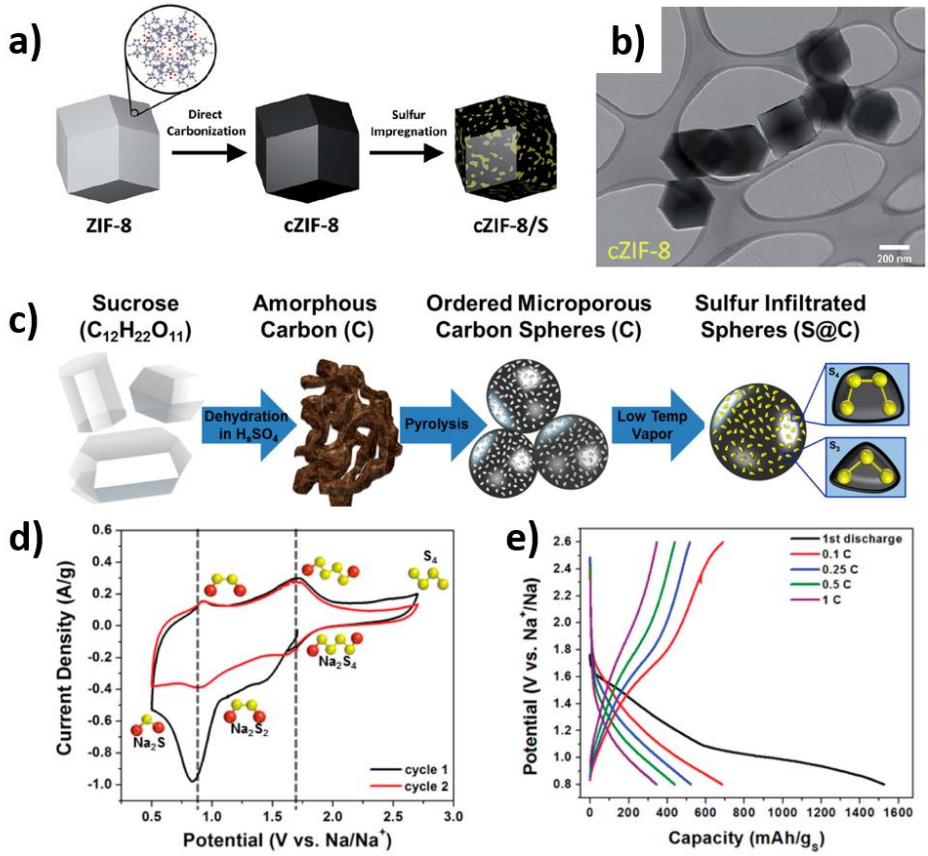


**Figure 21.** Microporous-carbon hosts for short-chain sulfur confinement. (a) Schematic for the carbonization of a zeolitic imidazolate framework (ZIF-8) particle followed by sulfur melt-diffusion. (b) TEM image of carbonized ZIF-8 dodecahedral nanoparticles. Reproduced with permission.[204] Copyright 2016, The Royal Society of Chemistry. (c) Synthesis of microporous carbon spheres from the dehydration and pyrolysis of sugar, with subsequent sulfur vapor-phase impregnation. (d) Cyclic voltammetry of microporous carbon-sulfur cathodes, demonstrating sodiation of short-chain sulfur ($S_4$) species, at 50 μV $s^{-1}$. (e) Representative galvanostatic charge and discharge profiles at increasing C-rates, illustrating single sloping curves. Reproduced with permission.[206] Copyright 2017, American Chemical Society.

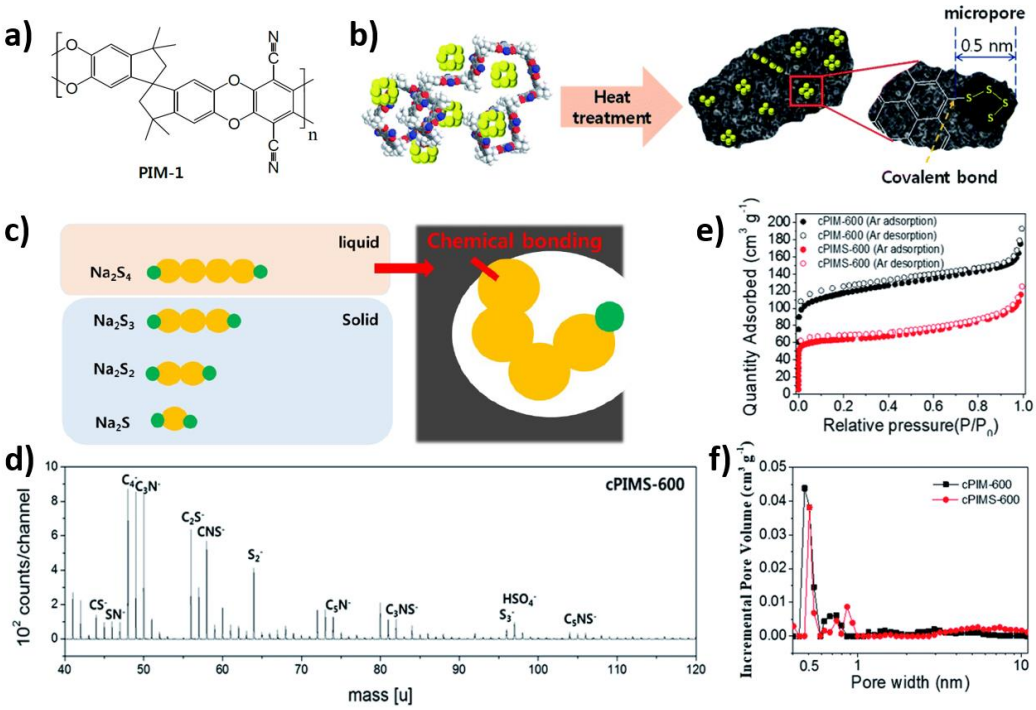


**Figure 22.** Short-chain sulfur species covalently bound within a microporous carbon structure. (a) Scheme illustrating the heating of a ground mixture of microporous PIM-1 powder and elemental sulfur, first at 155 °C for sulfur infiltration, then followed by carbonization and covalent bond formation at 600 °C. (b) Chemical structure of the as-synthesized PIM-1 repeating unit. (c) Short-chain sodium polysulfide discharge products formed within the carbon micropores. (d) TOF-SIMS spectra of the microporous PIM-based sulfur composite. (e) Argon adsorption/desorption isotherms at 87 K. (f) Pore size distribution based on the Horvath-Kawazoe method for micropore analysis. Reproduced with permission.[211] Copyright 2020, The Royal Society of Chemistry.

**Table 6.** Na-S battery systems based on covalently-bonded sulfur and short-chain sulfur composites.

| Short-chain sulfur/ composite cathodes | Initial specific capacity (C-rate/ current density) | Specific capacity at final demonstrated cycle | Cycle lifetime demonstrated | S-content | Ref. |
|---|---|---|---|---|---|
| **Sulfurized carbons and sulfurized polyacrylonitrile (PAN)** | | | | | |
| S-PAN particles on porous Ni-foam | 655 mAh $g^{-1}$ (0.1 mA $cm^{-2}$) | 500 mAh $g^{-1}$ (0.1 mA $cm^{-2}$) | 18 | 42% | 182 |
| S-PAN particles (PAA-binder enhanced) | 1195 mAh $g^{-1}$ (0.5 C) | 1000 mAh $g^{-1}$ (0.5 C) | 1000 | 41% | 184 |
| Electrospun S-PAN fibers | 219 mAh $g_{(composite)}^{-1}$ (1 C) | 153 mAh $g_{(composite)}^{-1}$ (1 C) | 500 | 31% | 181 |
| Electrospun S-PAN nanowebs | 342 mAh $g_{(composite)}^{-1}$ (0.1 C) | 266 mAh $g_{(composite)}^{-1}$ (0.1 C) | 200 | 41% | 183 |

| | | | | | |
|---|---|---|---|---|---|
| Electrospun Se-doped S-PAN ($Se_{0.04}S_{0.96}$) | ~700 mAh $g^{-1}$ (0.5 A $g^{-1}$) | 456 mAh $g^{-1}$ (0.5 A $g^{-1}$) | 200 | 49–54% | 185 |
| Electrospun $SeS_2$-PAN fibers | 1043 mAh·$g^{-1}$ (1 A $g^{-1}$) | 800 mAh·$g^{-1}$ (1 A $g^{-1}$) | 400 | ~52% | 186 |
| SeS-PAN particles | 721 mAh $g^{-1}$ (0.2 A $g^{-1}$) | ~550 mAh $g^{-1}$ (0.5 A $g^{-1}$) | 150 | 63% (17% S, 46% Se) | 188 |
| Se-doped S-PAN ($Se_{0.08}S_{0.92}$) | 1185 mAh $g^{-1}$ (0.4 A $g^{-1}$) | 770 mAh $g^{-1}$ (0.4 A $g^{-1}$) | 500 | 44% | 187 |
| Te-doped S-PAN ($Te_{0.04}S_{0.96}$) | 1067 mAh $g^{-1}$ (0.5 A $g^{-1}$) | 970 mAh $g^{-1}$ (0.5 A $g^{-1}$) | 600 | 41% | 190 |
| I-doped S-PAN | 994 mAh $g^{-1}$ (0.5 C) | 768 mAh $g^{-1}$ (0.5 C) | 500 | 42% | 191 |
| **Sulfur co-polymers** | | | | | |
| Benzoxazine-derived sulfur-copolymer on graphene | ~500 mAh $g^{-1}$ (1 A $g^{-1}$) | 285 mAh $g^{-1}$ (1 A $g^{-1}$) | 100 | < 89% | 197 |
| Thioether-functionalised carbon | ~600 mAh $g^{-1}$ (0.1 A $g^{-1}$) | 330 mAh $g^{-1}$ (1 A $g^{-1}$) | 800 | 21% | 198 |
| Benzenedisulfonic acid/sulfate-based sulfurized carbon | 696 mAh $g^{-1}$ (2.5 A $g^{-1}$) | 452 mAh $g^{-1}$ (2.5 A $g^{-1}$) | 1000 | 40% | 199 |
| Carbon disulfide-derived composite (red phosphorus reactant) | 1064 mAh $g^{-1}$ (1.6 C) | 811 mAh $g^{-1}$ (1.6 C) | 950 | 38% | 200 |
| MOF-derived S, N-doped porous carbon-sulfur composite | 1246 mAh $g^{-1}$ (0.1 A $g^{-1}$) | 730 mAh $g^{-1}$ (1 A $g^{-1}$) | 1000 | 37% | 201 |
| **Microporous carbon-sulfur composites** | | | | | |
| ZIF-8-derived microporous carbon-sulfur composite | 866 mAh $g^{-1}$ (0.1 C) | 600 mAh $g^{-1}$ (0.1 C) | 100 | 47% | 11 |
| Carbonized ZIF-8 microporous carbon-sulfur composite | 873 mAh $g^{-1}$ (0.2 C) | ~500 mAh $g^{-1}$ (0.2 C) | 250 | ~50% | 204 |
| Sugar-derived sulfur-infiltrated spheres | ~900 mAh $g^{-1}$ (0.1 C) | 306 mAh $g^{-1}$ (1 C) | 1500 | 35% | 206 |
| PVDF-derived microporous carbon-sulfur composite | 918 mAh $g^{-1}$ (0.1 C) | 392 mAh $g^{-1}$ (1 C) | 200 | 40% | 205 |
| Polymer of intrinsic microporosity, PIM-1-based carbon–sulfur composite | ~500 mAh $g^{-1}$ (0.1 C) | ~550 mAh $g^{-1}$ (0.1 C) | 250 | ~30% | 211 |

Note: unless otherwise stated, all specific capacities are based on the weight of sulfur, or the combined chalcogen weight in the case of chalcogen-doped S-PAN.

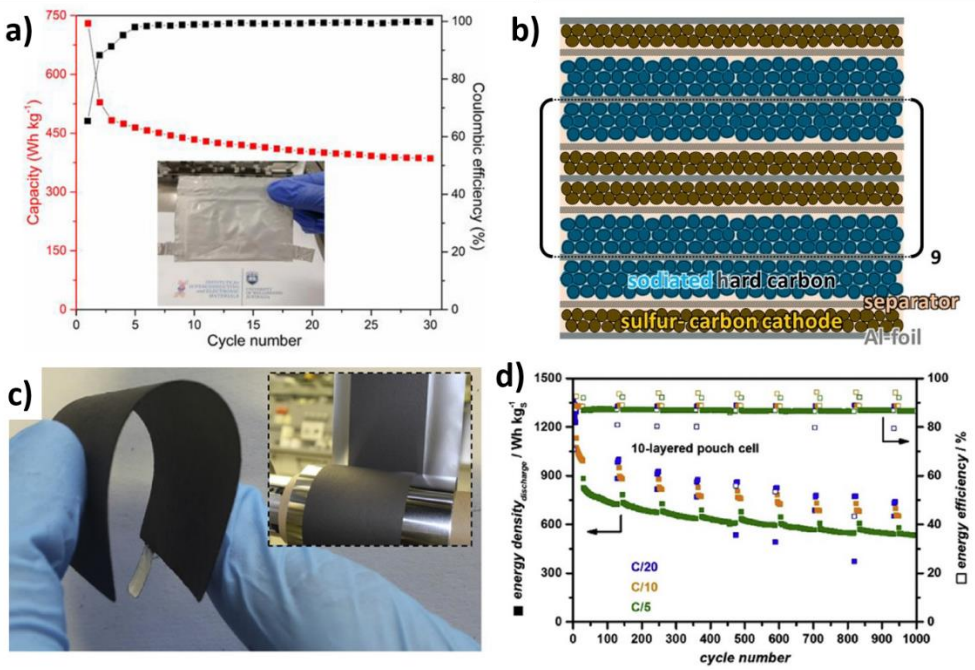


**Figure 23.** Sodium-sulfur batteries with pouch cell configurations. (a) Energy density of sulfur-based cathode based on core-shell ZnS catalysts, tested in a full-cell battery pouch assembly, at current density of 0.1 A $g^{-1}$. Inset figure demonstrates dimensions of pouch cell. Energy density values based on the mass of cathode material. Reproduced with permission.[140] Copyright 2020, American Chemical Society. (b) Schematic of a 10-layered pouch cell, consisting of a sodiated-carbon anode and sulfur-carbon composite cathode. (c) Image of double-sided coating of hard carbon for sodiated-carbon anodes. Inset picture displays roll-to-roll production of electrodes on aluminium foil. (d) Energy density and efficiency of 10-layered sodium-sulfur pouch cell, based on the sulfur mass. Reproduced with permission.[238] Copyright 2019, Elsevier.

**Table 7.** Battery chemistries of sulfur-based cathodes coupled with alkali metal anodes (M = Li, Na, K).

| | **Sulfur Battery Chemistries (M-S)** | | |
|---|---|---|---|
| | **Li-S** | **Na-S** | **K-S** |
| Relative atomic mass | 6.94 | 22.99 | 39.10 |
| Crustal abundance of metal anode | 0.0018% | 2.27% | 1.84% |
| Ionic radius (Å) | 0.76 | 1.02 | 1.38 |
| Melting point of pure metal anode (°C) | 180 | 98 | 64 |
| Eutectic liquid and alloying metal anodes | Yes | Yes | Yes |
| Specific capacity of metal anode (mAh $g^{-1}$) | 3860 | 1165 | 685 |
| Volumetric capacity of metal anode (mAh $cm^{-3}$) | 2062 | 1128 | 591 |
| Standard reduction potential of metallic anode $E°$ (V *vs.* SHE) | −3.04 | −2.71 | −2.93 |
| Theoretical gravimetric energy density of M-S battery (Wh $kg^{-1}$) | 2567 | 1274 | 1023 |
| Theoretical volumetric expansion of sulfur upon full discharge (*i.e.* $S_8 \rightarrow M_2S$) | ~80% | ~170% | ~300% |

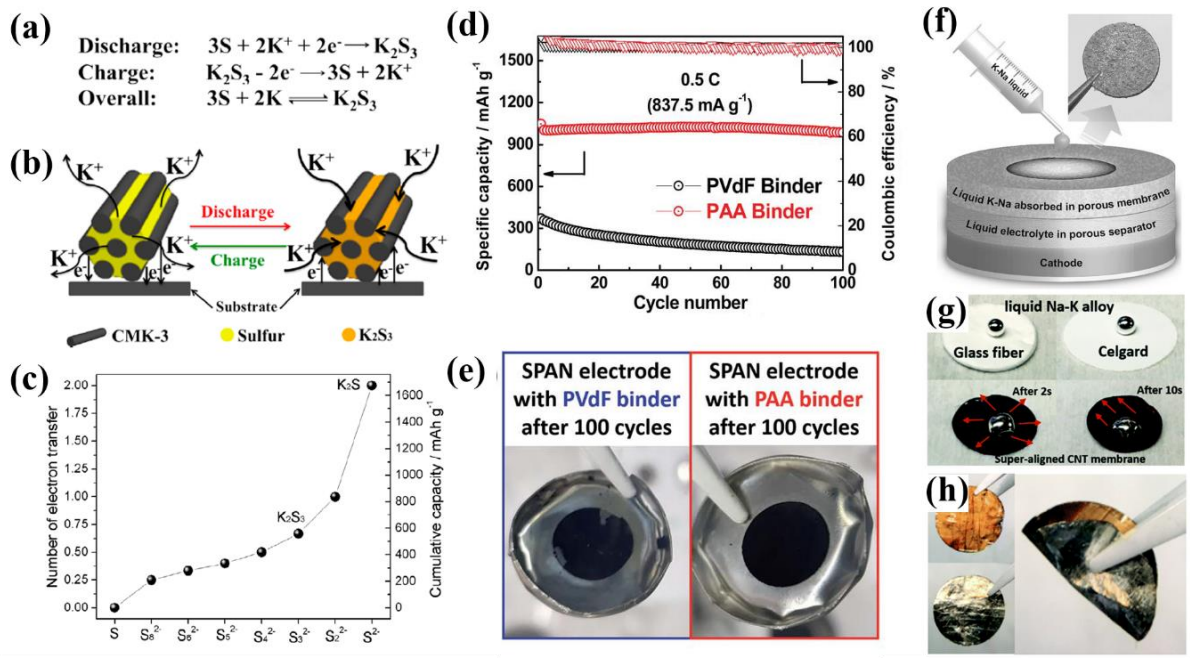


**Figure 24.** Recent advancements of potassium-sulfur systems. *Left panel*: (a,b) Potassiation mechanism of sulfur in a mesoporous CMK-3 carbon host, to $K_2S_3$ as the final discharge product. Reproduced with permission.[252] Copyright 2014, American Chemical Society. (c) Theoretical specific capacity with potassiation extent. Reproduced with permission.[251] Copyright 2020, Wiley-VCH. *Middle panel*: K-S battery cathodes assembled with different cathode binder systems. (d) Cycle performance and Coulombic efficiency of K-S batteries with PVDF versus PAA binders. (e) Condition of cathodes after cycling for 100 cycles. Reproduced with permission.[258] Copyright 2018, The Royal Society of Chemistry. *Right panel*: Potassium-sodium eutectic liquid alloying anodes. (f) Schematic cell assembly for a liquid K-Na liquid anode at room temperature. Reproduced with permission.[270] Copyright 2016, Wiley-VCH. (g) optical images of a K-Na droplet on common glass fiber and polypropylene Celgard separators, and absorption process of the liquid alloy into a carbon nanotube membrane used as anode current collector. (h) optical images of the K-Na liquid-infused CNT membrane; the matte black membrane surface turns a shiny silver after infusion (bottom-left), while the reverse side turns copper-gold (top-left). Reproduced with permission.[271] Copyright 2018, Royal Society of Chemistry.